AUTONOMOUS ENERGY HARVESTING AND POWER MANAGEMENT UNIT FOR WIRELESS IOT APPLICATIONS

A Dissertation

by

ZIZHEN ZENG

Submitted to the Office of Graduate and Professional Studies of
Texas A&M University
in partial fulfillment of the requirements for the degree of

DOCTOR OF PHILOSOPHY

Chair of Committee,	Edgar Sánchez-Sinencio
Committee Members,	José Silva-Martinez
	Pao-Tai Lin
	Hongmin Qin
Head of Department,	Miroslav M. Begovic

December 2020

Major Subject: Electrical Engineering

ABSTRACT

Internet-of-Things has aroused wide focus to make our society more intelligent and more efficient by employing tremendous connected devices. To ensure its efficiency, battery replacement and maintenance become major challenges. Therefore, energy harvesting (EH) with smart power management is one of the key enabling technologies. With EH technologies, the sensors can autonomously capture the available ambient energy and thus a battery-less solution is even feasible because of the ultra-low-power design techniques.

This dissertation focuses on the EH technologies with smart power management unit (PMU) and integrated circuits (IC) for Internet-of-Things (IoT) applications. In the first part, three different RF-EH systems for wide input-power range operations are presented with different working scenarios: the first one works with a cascading DC-DC converter for maximum power point tracking (MPPT) and a novel fractional open-circuit voltage approximation (FOCVA) is proposed to help with MPPT; the second one delivers the energy directly to a system-on-chip (SoC) loading with a fully integrated hill-climbing MPPT; the third one employs dual-band operations and a nano-watt hysteresis-controlled switched-capacitor (SC) converter to boost up the output voltage and reduce the reverse leakage current for modulated signal harvesting.

In the second part, an EH system based on autonomous IC interface is proposed to extract the energy from a centimeter-scale electromagnetic (EM) wind turbine. To improve the efficiency of such an EH system, a self-start-up and self-biased active rectifier is employed. A hysteresis-controlled boost converter is designed with self-zero-current-switching calibrations, which achieves a peak DC-DC efficiency of 93.3% with a maximum efficiency improvement of 12.7%. Also, a novel frequency-to-amplitude conversion (FAC) maximum power point tracking (MPPT) method is proposed for cycle-to-cycle MPPT. In wind-field testing, the EH system starts to track the MPP one cycle after start-up. In the steady-state, the EH system maintains its cycle-to-cycle MPP in different wind speed conditions from 1.0 to 5.0 m/s, achieving a 630% energy extraction gain at a low wind speed of 1.2 m/s.

DEDICATION

To my mother, my father, my family,

my friends,

and my beloved.

ACKNOWLEDGMENTS

I would like to thank my advisor Professor Edgar Sánchez-Sinencio who always provided insightful suggestions and always encouraged me to explore many possibilities. Most of the ideas in my publications are initiated from casual discussions with him. And his long-term devotion to research has set a model since the day when I joined the AMSC group at Texas A&M University. And I would like to thank Professor Amine Bermak, Professor Chi-Ying Tsui, Professor Ross Murch, and Professor Wing-Hung Ki in Hong Kong University of Science and Technology. I was trained to be a qualified researcher by their outstanding research leadership. And I would like to thank Professor Gabriel A. Rincón-Mora from Georgia Institute of Technology, John Khoury and Mike Mulligan from Silicon Labs. They gave a lot of useful suggestions during visits and reshaped my thinking with inspiring perspectives. I would like to thank Yu Su and Mustafa Koroglu from Silicon Labs. They provided me an internship opportunity to work in an exciting research project. This industry experience has urged me to re-examine my innovations with a critical standard.

I would like to thank the lab members from the AMSC group, Xiaosen Liu, Congyin Shi, Mohamed A. Abouzied, Judy Amanor-Boadu, Johan Estrada-Lopez, Sungjun Yoon, Sanghoon Lee, Joseph Riad, Guillermo Garayar-Leyva, Adriana Sanabria, Sergio Soto-Aguilar, and many others. They supported my research and study during my Ph.D. study; and also my co-authors, Shanpu Shen, Xiaopeng Zhong, Xing Li, and Bo Wang from Hong Kong University of Science and Technology. They provided a lot of useful suggestions and helps with my research projects and publications. I also would like to thank my family. Without their support and encouragement, I cannot overcome all these challenges alone. They always encourage me to stand up to the unknown. Since I never expressed my gratitude directly to their faces before, I would like to take this chance to say thank you for their selfless love and care. It is my fortune to be born in a family with so much love, kindness, and wisdom. The Ph.D. study is just a part of the journey in life with a mixture of joy, pain, confusion, and thrilling. But once you remind the initial motivation to create something different, you would regain the endeavor to find the right path.

CONTRIBUTORS AND FUNDING SOURCES

Contributors

This work was supported by a dissertation committee consisting of Professors Edgar SánchezSinencio, José Silva-Martinez, and Pao-Tai Lin of the Department of Electrical and Computer Engineering and Professor Hongmin Qin of the Department of Biology. All other work conducted for the dissertation was completed by the student independently.

Funding Sources

Graduate study was supported by the TI Excellence fellowship and Qualcomm fellowship. Research projects were funded in part by Qualcomm, in part by Silicon Labs, and in part by Texas Instruments.

NOMENCLATURE

TAMU	Texas A&M University
AMSC	Analog and Mixed Signal Center
IC	Integrated Circuit
PMU	Power Mangement Unit
MOSFET	Metal Oxide Silicon Field Effect Transistor
EH	Energy Harvesting
MPPT	Maximum Power Point Tracking
MPP	Maximum Power Point
OC	Open-Circuit
LDO	Low-Dropout Regulator
SoC	System-on-Chip
SiP	System-in-Package
SC	Switched-Capacitor
RF	Radio Frequency
IoT	Internet-of-Thing
WSN	Wireless Sensor Network
VCE	Voltage Conversion Efficiency
PCE	Power Conversion Efficiency
EM	Electromagnetic
PMSG	Permanent Magnet Synchronous Generator

TABLE OF CONTENTS

Page

LIST OF FIGURES

FIGURE Page

LIST OF TABLES

TABLE Page

1. INTRODUCTION

Internet-of-Things (IoT) has aroused wide focus to make our society more intelligent and more efficient by employing tremendous connected devices. The IoT technology has reshaped the entertainment, industry, transportation, and many other areas, and its impacts are still increasing with the help of artificial intelligence and cloud computing technologies. To achieve IoT, wireless sensor network (WSN) is vitally important since it provides the communication ability among the sensors in the edge. Estimated by Fig. 1.1, The total connected number of IoT devices would reach to five billion with an increased rate of 10% to 20% annually.

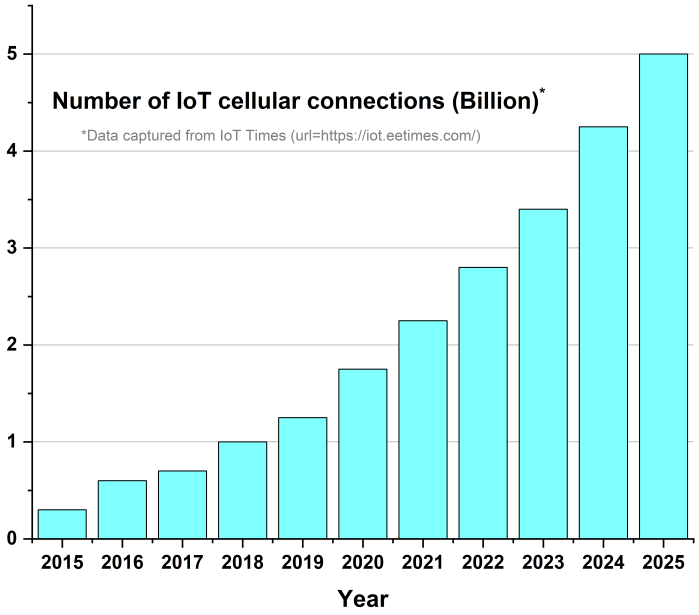

Figure 1.1: IoT connected device number prediction.

1.1 IoT Edge-Sensing Applications

Most of the IoT devices are connected with modern wireless communication protocol, which is listed and compared in Fig. 1.2. The WSN with SoC integrates multiple functions in a single chip,

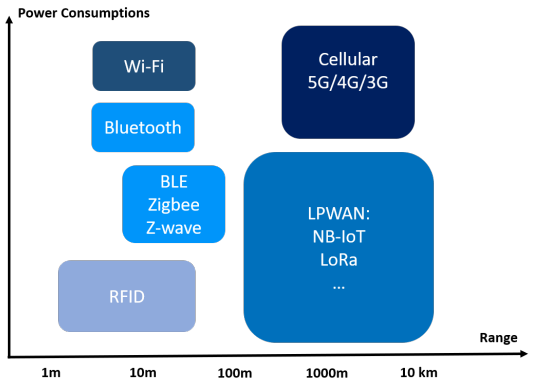

Figure 1.2: IoT wireless communication protocol.

such as sensing abilities, local computations, data compression, and communications. Meanwhile, ultra-low-power techniques have been employed to extend the battery life-time for long-term usage. However, power management on a tremendous number of devices is still a challenge in many IoT applications, especially for the scenarios where the battery replacement is extremely difficult. Some hazard areas even prohibit the battery to prevent secondary damage, where sensors replacement and maintenance become major challenges.

Product Series[1]	Wireless Protocol	MCU/ Processor	System Integration	Integrated PMU	Consumed Power
LR1110	LoRa	NA.	SoC	DC/DC LDO	1.6μA@ sleep mode 1.1mA@ active mode
BlueNRG-2	BLE	Cortex-M0	SoC	DC/DC LDO	500nA@ stand-by 0.9μA@ sleep-mode 1.9mA@ active mode[2]
ZGM130S	Z-Wave	Cortex-M4	SiP	DC/DC LDO	0.8μA@ sleep-mode 9.8mA@ Rx 100 kbps
nRF9160	NB-IoT	Cortex-M33	SiP	PMIC (SiP)	3μA@ PSM stand-by 5.5μA@PSM 1KB/12h 150mA@LTE-M full speed

[1] All data is captured from the product datasheet
[2] Average connection current consumption 7.059 μA (connection interval 1000 ms) – 3 years, 10 months, 12 days with 230 mAh battery (CR2032)

Figure 1.3: IoT SoC specification and comparisons.

Fig. 1.3 listed some commercial SoC products for IoT platforms and their main specifications are also listed for comparison. The power management unit (PMU) circuits are integrated into

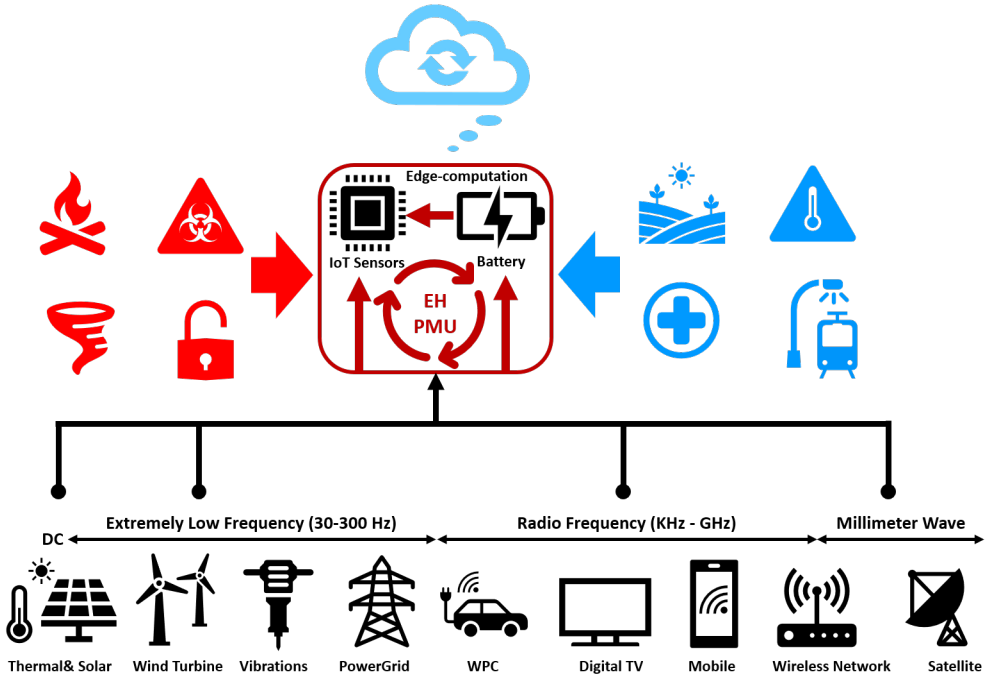

Figure 1.4: IoT edge-sensing systems with EH PMU.

the system to reduce the entire form factor and cost. As mentioned, even with ultra-low-power techniques, the power consumption of the system is still critical for long-term ($5 - 10$ years) applications. Therefore, energy harvesting (EH) with smart power management is one of the key enabling technologies for the development of IoT. With EH technologies, the sensors can capture the ambient energy to prolong the battery's lifetime and thus a battery-less solution is even feasible.

1.2 Energy Harvesting Technologies

Energy harvesting technologies have developed and been employed for many decades in large-scale wind energy and solar power harvesting. The ambient energy can also provide available energy for wireless autonomous devices. Fig. 1.4 illustrates the concept of EH PMU for IoT edge-sensing applications. The energy from the thermal gradient, solar panel, wind flow, vibration, wireless radio waves, and many others can provide sufficient energy for such IoT applications with dedicated EH PMU designs. The EH PMU not only provides the required regulation voltage for the SoC functions but also extracts most of the energy from the EH source, charging to the battery

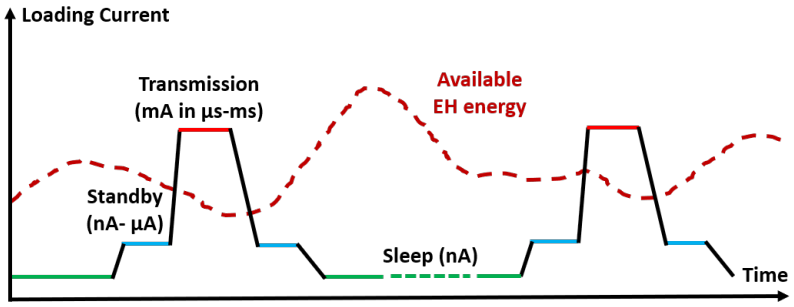

Figure 1.5: A typical operation mode for EH-enabled IoT edge-sensing system.

or directly delivering to the SoC loading. Since the EH source is different across the spectrum (from DC to RF) with different input power and profile, a specialized PMU is required for specific EH sources to ensure optimal performance.

Fig. 1.5 shows a typical operation mode of the IoT edge-sensing system. To reduce overall power consumption, the system remains in standby mode or sleep mode. It only operates in active mode within milliseconds to transfer the critical data. Therefore, the EH energy can sustain the full system operations even its affordable power is not comparable with the peak power consumption of the SoC systems. The captured energy from EH can be stored in a capacitor buffer or a battery and then released for system operations.

Fig. 1.6 shows five different types of available ambient energy for harvesting. Their power density is also listed for comparison [1]. The solar and wind energy power density is the largest, especially in outdoor areas. The thermal and vibration power density is in the middle range, and it can be very useful in some particular applications. The typical power density of RF energy is less than 1 μW/cm^2, which is the smallest compared to other EH sources. However, RF energy is immune to weather conditions [2]. And RF EH technology does not need additional energy harvester components like the other EH applications, which is beneficial to further reduce the system cost and minimize the system size.

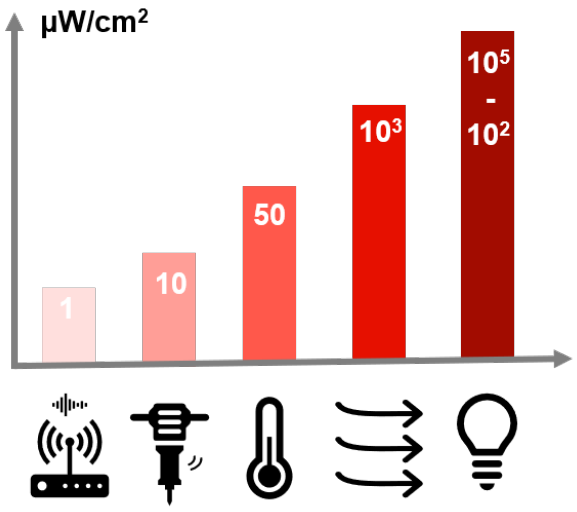

Figure 1.6: Available EH source overview.

1.3 RF Energy Harvesting Technologies

1.3.1 RF Energy Overview

RF EH technologies have been widely used in far-field radio frequency identification devices (RFID) applications. For the ambient RF EH, the available energy in the environment is first examined. In Fig. 1.7a, a recorded RF spectrum data in Seattle is shown. And in Fig. 1.7b, the occupancy conditions of each RF band are listed. The RF energy is abundant in urban and indoor applications, which provides a lot of design flexibility. The ISM bands (900MHz and 2.4GHz) are the most common target frequency band for RF EH in recent works. From Fig. 1.7a, the power density in these two bands are also the largest compared to other bands.

1.3.2 RF EH for Wireless Sensor Systems

For IoT WSN applications shown in Fig. 1.8, because the main off-shell component (Antenna) already exists for wireless communication, the cost of adding RF EH abilities is relatively low compared to other EH sources. What's more, the sufficient wireless communications among the WSN provide large potentials for RF EH. Based on the observation in recent works [2, 3, 4, 5, 6], the RF EH scenarios are divided into three conditions: intentional EH, re-used EH, and captured

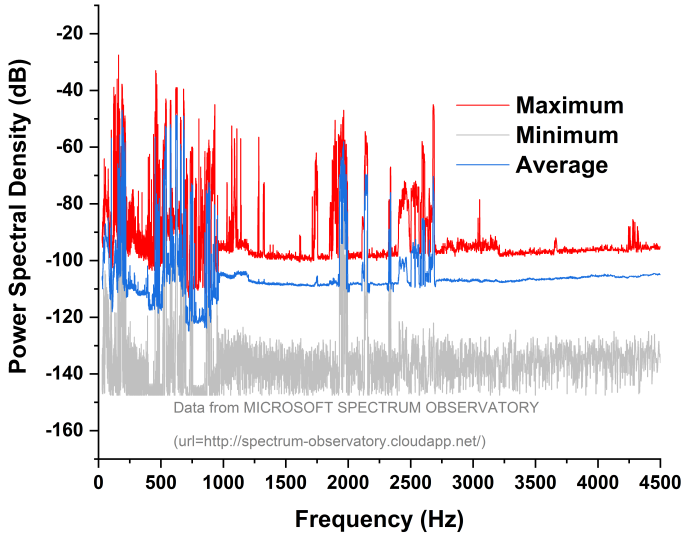

(a)

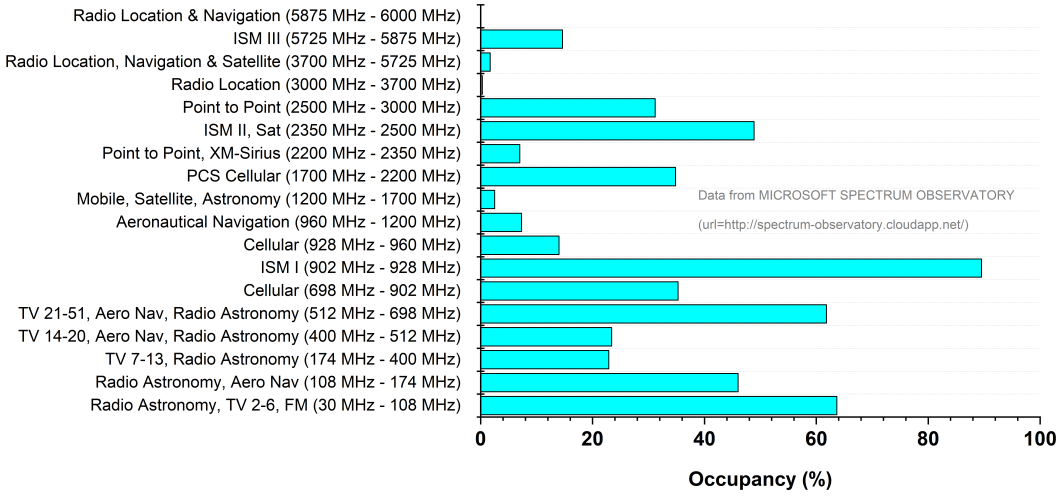

(b)

Figure 1.7: (a) Available RF power density and (b) spectrum occupancy in Seattle, WA.

EH. Intentional EH is achieved with a specific power transmitter to power up the WSN. Similar to conventional RFID applications, it powers up the whole system with sufficient energy, which can be used in some critical applications, for example, to start up the drained down system, to arouse the system for critical data detection. RF EH is reused when the signal transmission is started, capturing redundant energy and make full use of this energy. The EH energy can be the same

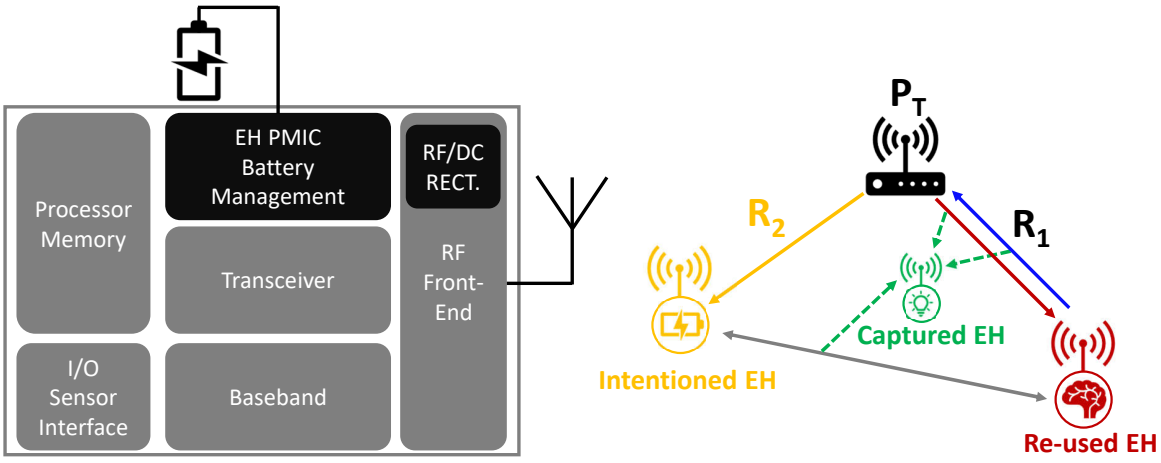

Figure 1.8: RF EH in IoT wireless systems.

band or from the adjacent/blocker bands. And the last one is the captured EH, which captures the accidental RF energy from nearby sensors or other potential sources. Overall, the RF EH technologies can provide crucial and alternative energy when the battery is down or the other EH source is not available. The RF EH system is supposed to have self-start-up and self-sustained functions, while it can also accommodate other EH sources to provide more robust EH abilities.

1.3.3 RF EH Principles and Challenges

To convert the available RF energy to DC energy, the RF-DC rectifier is commonly used, which can be classified as single-end types and differential types. Differential rectifiers require balun transformer or differential antenna designs, which limits the application ranges. Single-end rectifiers do not have these requirements in differential type. However, the forward voltage drop in diodes or the threshold voltage in MOSFET decrease the performance, especially in low power and low voltage domains. For analysis purposes, the working principle and major design challenges in single-ended rectifiers are discussed, which is also applicable in differential rectifiers.

Fig. 1.9 shows the conventional single-end Dickson rectifier topology. To generate a high DC output voltage, the rectifier cells are usually put in cascade [7]. And its operation principle is also illustrated based on two different states: in the negative cycle ϕ_1, the current flows from GND to the bottom plate of flying capacitor C_{1a}, charging the DC voltage of V_{1a} to V_{RF}. And because of

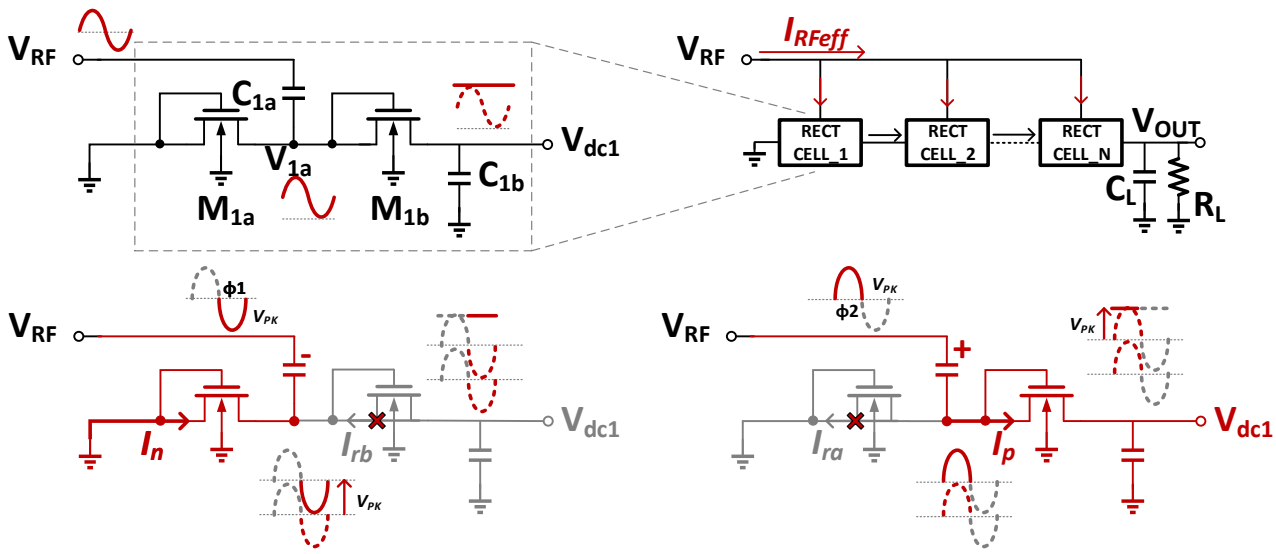

Figure 1.9: RF-DC rectifier operation principles.

the flying capacitor, the AC amplitude are also coupled on the V_{1a} at the same time; in the positive cycle ϕ_2, the current flows from V_{1a} to the DC output voltage V_{dc1}, the final DC voltage is charged up to $2{*}V_{RF}$, and stored in the filtering capacitor C_{1b}. The Dickson rectifier is also named as voltage doubler because the ideal output voltage is two times of the RF signal amplitude. However, in real implementations, the amplitude of V_{RF} can be as low as 100 mV and the threshold voltage V_{TH} of devices is not negligible. To further improve rectifier efficiency in such low voltage operations, low-V_{TH}, zero-V_{TH}, or V_{TH}-compensated devices are widely employed to minimize the effect of V_{TH}. On the other hand, the diodes or diode-connected devices in rectifier are supposed to cut off the reverse current when the anode is negative. However, reducing V_{TH} inevitably decreases this ability, the undesired reverse leakage current is increased. And a design trade-off is required between these two important factors as shown in Fig. 1.11a: a proper device is selected for target working ranges; an optimum device dimension is designed for optimized efficiency. Even so, Because of its high-frequency operation, the fast current transitions are very critical to handle, making the leakage current issue is more severe in RF-EH applications.

Another important parameter is the stage-number of the rectifier. At the minimum input power,

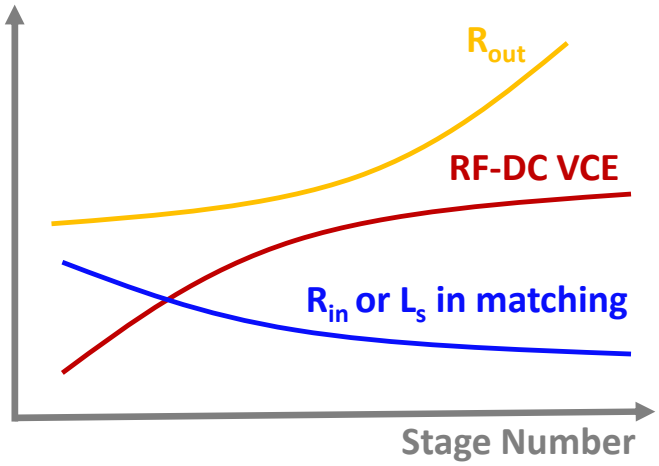

Figure 1.10: RF-DC rectifier stage number effects.

the output of a single-stage rectifier is not high enough to reach the required value. The stage number is increased to achieve a high enough output voltage, which compromises the overall efficiency. However, it is still acceptable for low-cost applications since no extra off-chip components are required. The stage-number also provides another degree of freedom to adjust the effective input impedance R_{in} for RF matching, because all the single-stage rectifiers are connected in parallel in the RF port; the output resistance R_{out} is also changed because the single-stage rectifiers are connected in series in DC ports, which is illustrated in Fig. 1.10.

An alternative solution is to add a cascading boost converter [8]. However, the cost is relative higher and the limited efficiency of the boost converter also degrades the overall performance. No matter which solution is employed, the boosted-up output voltage can exceed the tolerable maximum voltage very easily when the input power increases. Therefore, rectifiers with controllable output voltage and optimized efficiency for wide input-power operations are one of the main challenges in RF-EH applications.

Last but not the least, the reverse leakage current not only affects the rectifier efficiency but also degrades its performance in modulated signal harvesting applications. Recently, the optimized waveform for RF EH is studied. Multi-channels and multi-bands solutions are proposed to increase the output power for the rectifier within similar input powers [3]. However, the rectifier output

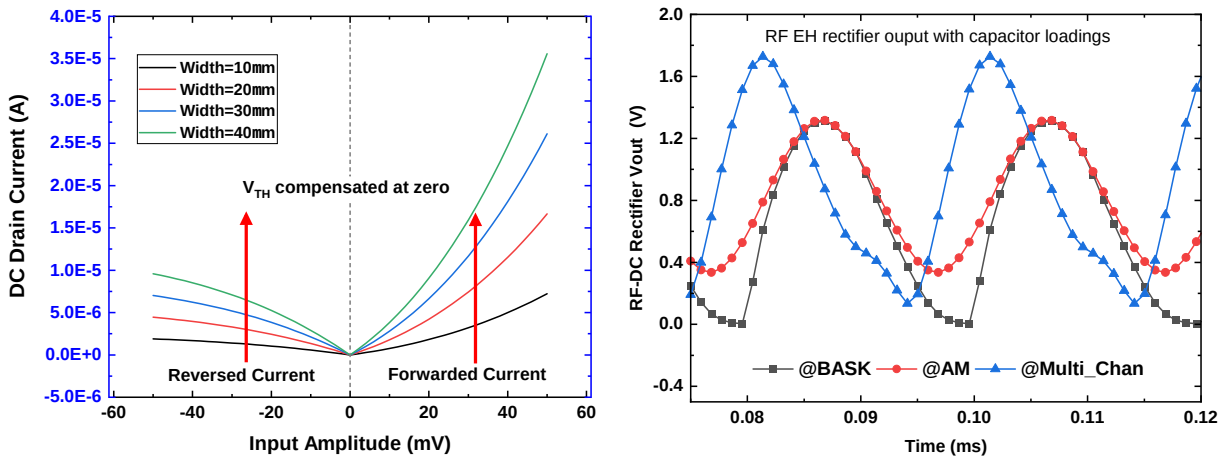

(a) (b)

Figure 1.11: RF-DC rectifier (a) design trade-off (b) output in different modulation schemes.

voltage can only be boosted when the instantaneous power is in its peak value. And in the valley phase, the output voltage remains at a low level because this instantaneous boost-up voltage cannot be reserved even in a pure capacitor loading (Fig. 1.11b). Moreover, in practical implementations, this optimized modulated waveform does not exist in most cases. The actual modulated waveform for signal communication even degrades the performance of the rectifier.

The huge available power density of the up-link signal compared to the down-link signal increases the harvested power capacities [2]. However, the energy profile and modulation scheme are highly dependent on user-behaviors and such high energy can only remain for a very limited period. What's more, the locations of the sensor are different from each other with variant coming power. The input power differences can be as high as 1000 times [2]. Conventional RF EH rectifiers are optimized for a limited working range and the voltage stress in such a wide input power range is very crucial for device reliability. Fig. 1.12 quantifies the variance of main design parameters in different input voltages. Z_{IN} is the effective input impedance of rectifier and it determines the matching network design; R_{OPT} is the optimal loading resistance for maximum power point extraction (MPPT), which can be a circuit loading directly or a DC-DC converter. Although the RF-DC gain is larger in high input power conditions, the nonlinear changes in Z_{IN} and R_{OPT}

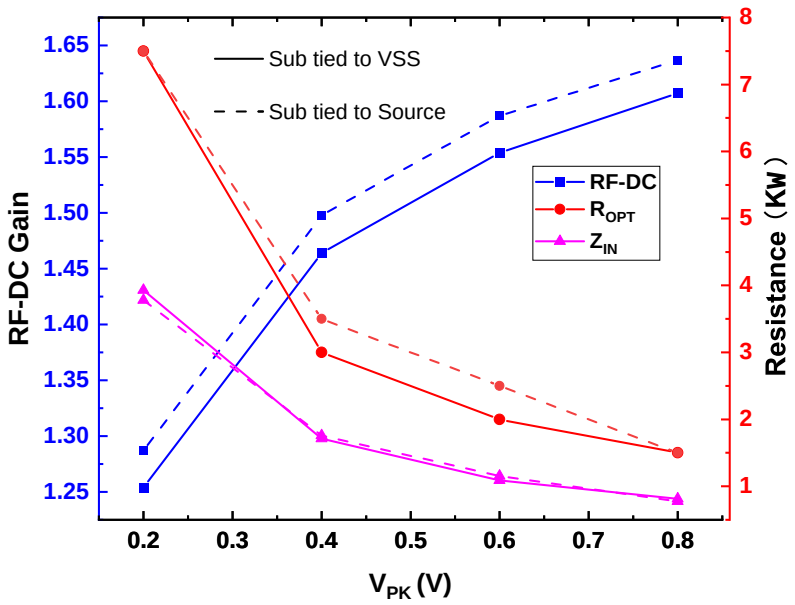

Figure 1.12: Rectifier parameters in different input (one-stage).

degrade the system performance, makes it harder to maintain the optimal MPPT operations for the RF EH system. Fig 1.12 also indicates the nonlinear changes not only come from the body-biased effect in high voltage but also come from the sub-threshold operations of the devices in low voltage domains. Therefore, maintaining high efficiency among such a wide input power range is very critical in the RF EH systems. Overall, the main challenges for RF EH applications are addressed in this dissertation:

- Sensitivity, wide-working range, and efficiency trade-off
- Wide input-power range operations within tolerable voltage stress
- Wide-range and power-efficient MPPT
- EH capabilities to capture modulated RF signals
- High efficiency and self-start-up and self-sustained functions

1.4 Wind Energy Harvesting Technologies

Another important EH source shown in Fig. 1.6 is the wind. Wind is a free, abundant, and promising energy source to enable the Internet-of-Things (IoT) edge-sensing applications at outdoor remote areas [9, 10, 11], or the indoor ventilating systems [12, 13]. As shown in Fig. 1.13, the wind EH technologies are beneficial for various applications, such as gas and temperature detection, vehicles and roadside monitors, battery recharging, agriculture and wildfire sensing and so on. For these IoT applications, the form factor of the harvester is preferred to be minimized while its harvested power, especially at low wind speed, is desired to be maximized. Therefore, the research on micro-scale energy harvesters for low-wind-speed is gaining a lot of attention [14, 15].

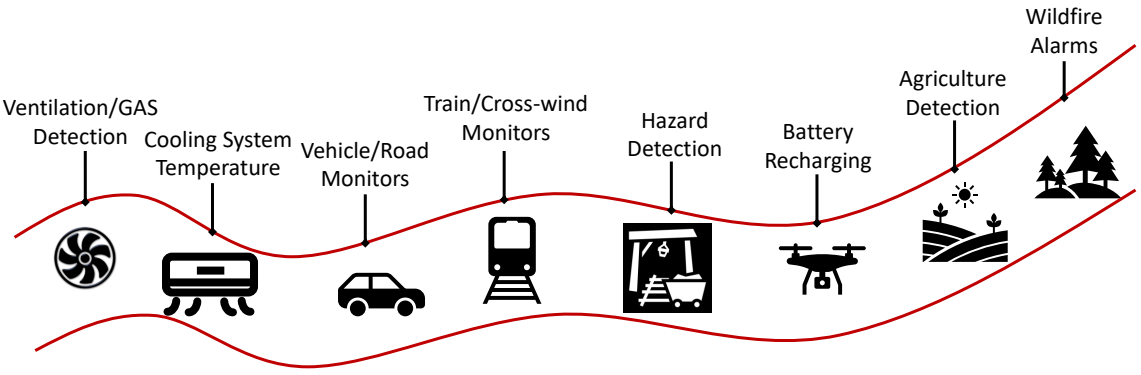

Figure 1.13: Wind EH for IoT edge-sensing applications.

1.4.1 Wind Energy Profiles

The National Centers for Environmental Information (NCEI) provides public access to wind speed and other environmental data. The average wind speed profile in the USA is accessible in [16]. In most of the land areas, the average wind speed is from 1 to 4 m/s measured in height of 10 m. And the wind speed is also highly dependent on the weather and climate conditions. Fig. 1.14 shows wind speed changes in one month of College Station, TX. The average wind speed changes within 3 to 6 m/s. The difference between the maximum and minimum wind speed depicts the

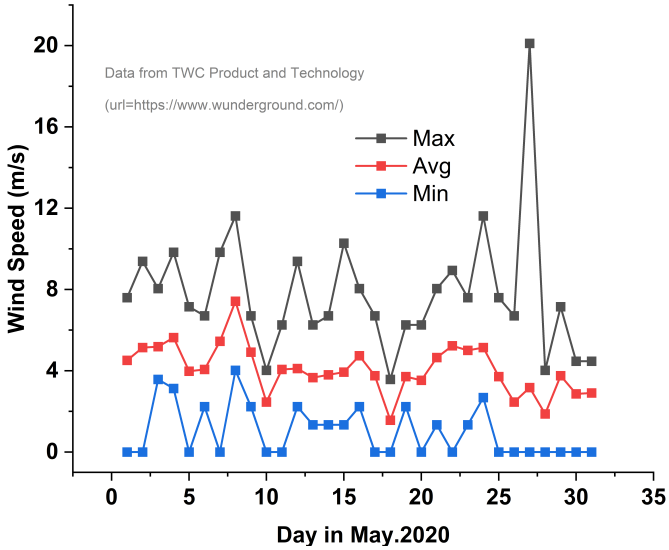

Figure 1.14: Daily wind speed profile in College Station, TX.

wind speed dynamic range.

1.4.2 Micro Wind Turbine Introduction

To minimize the harvester volume and to operate at the minimum wind speed, micro-mechanical structures are proposed in [17] and piezoelectric materials are explored in [18]. Among various types of wind energy harvesters, the rotary electromagnetic (EM) wind turbine generator (WTG) has proved to be a reliable solution, because of its relatively small size, low-cost, compatible voltage levels, and considerable output power at the low wind speed conditions [10, 11]. Therefore, in this dissertation, the rotary EM WTG is employed for Wind EH applications and designs. For a low-cost solution, an AC wind turbine generator (WTG) with a permanent magnet stator is selected. The conceptual model is provided in Fig. 1.15. The rotor is driven by the wind blade and generates the induced voltage for EH. The wind turbine captures the kinetic energy from the upstream wind and generates the available electrical energy. The power conversion coefficient is represented as C_{P}. Because of the medium air, the theoretical maximum value of C_{P} is 59.3% based on Betz's law. Even so, the output power of the cm-scale wind turbine is still quite sufficient for many μW-mW IoT applications. The electrical model of the wind turbine is also shown in

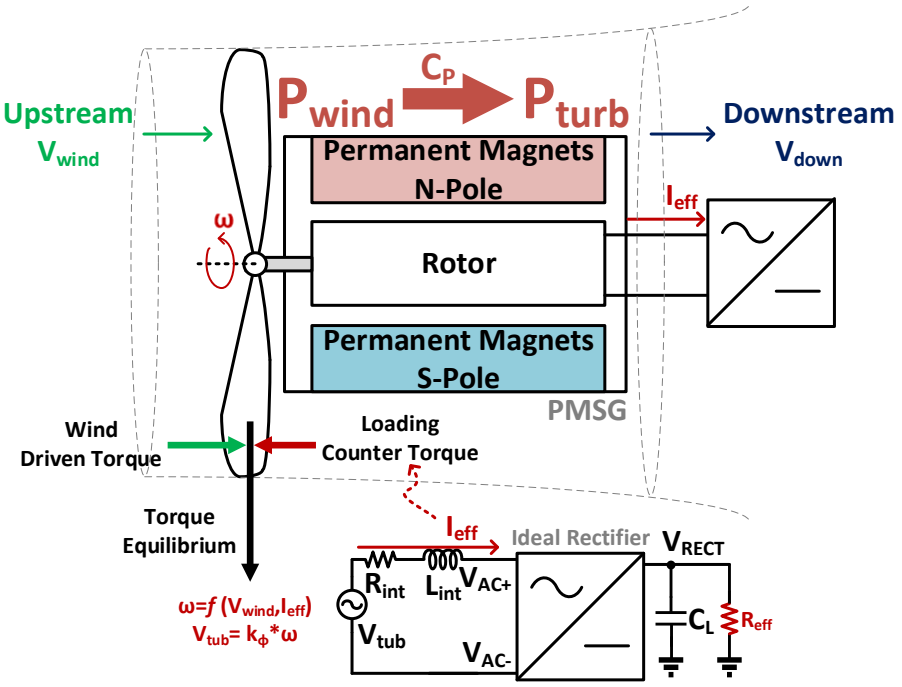

Figure 1.15: Centimeter-scale wind EH turbine for IoT applications.

Fig. 1.15. Another advantage of rotary WTG is that the induced voltage amplitude V_{tub} is linearly proportional to its rotation frequency. This linear relationship is utilized in the proposed MPPT, to achieve fast response and high efficiency. And it can also be employed in many other applications, such as low-cost wind speed detection.

1.4.3 Turbine Electrical Model and Maximum Power Point

Fig. 1.16a is the first-order electrical model of the adopted WTG for maximum power point analysis. The internal resistor R_{int} and inductor L_{int} represent the winding wire and the internal loss, respectively [10]. R_{int} is 60 Ω at DC and L_{int} is 3.5 mH. Since the reactance is less than 1% compared to the resistance, the effective resistive loading R_{eff} only needs to be matched with R_{int} for ideal maximum power extraction. From load-pull measurements, R_{eff} ranges from 100 to 1000 Ω. Fig. 1.16b shows the turbine output amplitude V_{PK} at different rotation frequencies. The corresponding wind speed is covered from 1.0 to 4.0 m/s (corresponding to the WTG rotation fre-

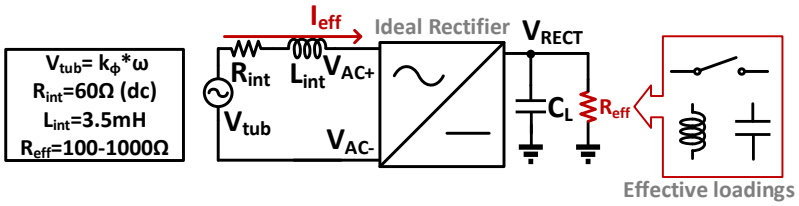

(a)

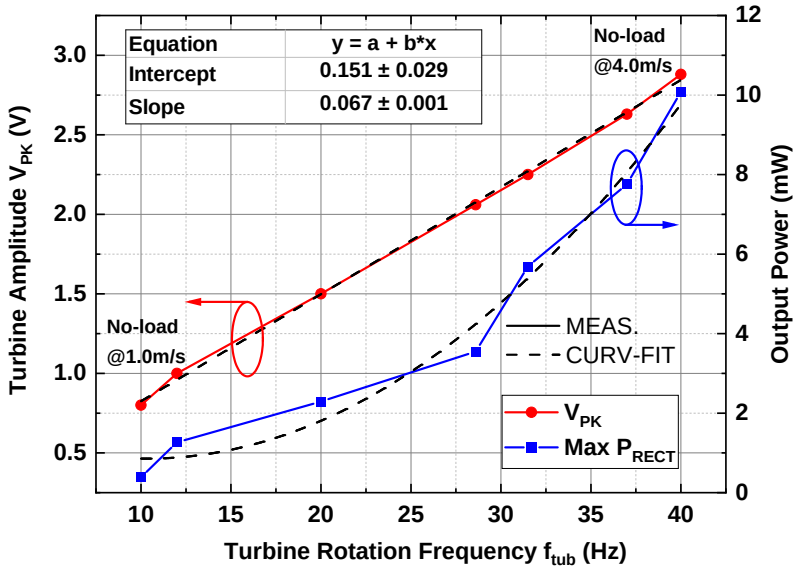

(b)

Figure 1.16: (a) Wind turbine electrical model and (b) amplitude-frequency measurement results.

quency f_{tub} from 10 to 40 Hz). And V_{PK} is recorded under open-circuit conditions. Theoretically, the amplitude of the WTG's output V_{tub} depends on f_{tub}, which is also shown in Fig. 1.16b. The angular rotation speed of the WTG's rotor under open-circuit conditions is determined by [9]:

$$P_{\text{wind}} = 0.5 \times \rho A v^3, P_{\text{tub}} = C_{\text{p}} \times P_{\text{wind}} \tag{1.1}$$

$$\omega_{\text{oc}} = v \times \frac{\lambda}{R}, \omega = \omega_{\text{oc}} - k_\omega \times I_{\text{eff}} \tag{1.2}$$

In (1.1), v is the coming wind speed and and A is the WTG's rotor swept area; P_{wind} is the kinetic energy of the wind, and C_{P} is the coefficient of power of WTG. In (1.2), λ is the coef-

ficient constant between wind speed and rotor frequency [10]; R is the outer blade radius; ρ is the air density constant. Therefore, the angular rotation speed ω_{oc} is linearly proportional to the wind speed based on the blade aerodynamics structure. However, when loaded by a current I_{eff}, a counter torque is generated to compensate for the wind-driven torque. As expressed in (1.2), ω_{oc} is decreased by this loading effect [9, 10], and k_ω is the coefficient of the loading effect. The final ω is achieved with torque equilibrium and this effect performs as an additional loss, which is inevitable in the WTG and is expressed as the Betz limit ($C_{\text{P}} = 59.3\%$). In the wind field-testing measurement, the achievable C_{P} of the selected cm-scale wind turbine ranges from 0.2 to 0.4 under the maximum output power conditions. Nevertheless, V_{tub} is still given by:

$$V_{\text{tub}} = k_\phi \times \omega \tag{1.3}$$

In (1.3), k_ϕ is the magnetic field constant provided by permanent magnets [11]. Therefore, the induced voltage V_{tub} amplitude is proportional to ω. Following Kirchhoffs voltage law, the final WTG's output voltage is:

$$V_{\text{AC}} = V_{\text{tub}} - R_{\text{int}} \times I_{\text{eff}} - L_{\text{int}} \times \frac{dI_{\text{eff}}}{dt} \tag{1.4}$$

The operation frequency of the rectifier is as low as sub-100Hz and the reactance is negligible (0.2%). Therefore, the effect of L_{int} is less than 1% in (1.4). The following analysis assumes (A) V_{tub} is an ideal sinusoidal wave; (B) the voltage drop across L_{int} is negligible; (C) the rectifier's efficiency is ideal with no loss; (D) the effective loading R_{eff} is resistive with an infinite capacitor buffer; (E) no loading effect is introduced. The RMS value of V_{tub} is:

$$V_{\text{tub}_{\text{RMS}}} = \frac{V_{\text{tub}}}{\sqrt{2}} \tag{1.5}$$

The rectifier output power P_{RECT} can be calculated as:

$$P_{\text{RECT}} = (\frac{V_{\text{tub}_{\text{RMS}}}}{R_{\text{int}} + R_{\text{eff}}})^2 \times R_{\text{eff}} \tag{1.6}$$

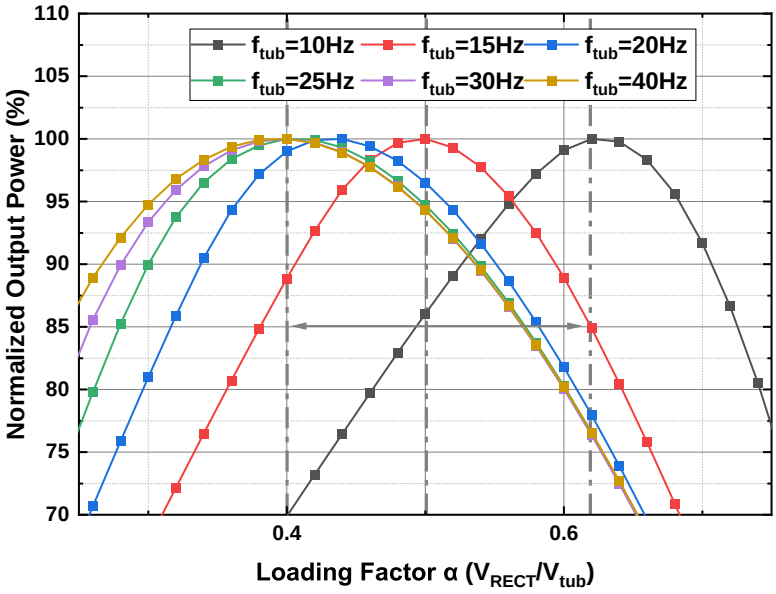

Figure 1.17: Power extraction efficiency under different loading conditions.

When R_{eff} equals R_{int}, the output power P_{RECT} achieves its maximum value as:

$$P_{\mathrm{RECT_{MAX}}} = \frac{{V_{\mathrm{tub}}}^2}{8 \times R_{\mathrm{int}}}, \text{where } V_{\mathrm{RECT}} = \frac{V_{\mathrm{tub}}}{2\sqrt{2}} \approx 0.35 \times V_{\mathrm{tub}} \tag{1.7}$$

In practical implementation, the maximum extracted power cannot reach the theoretical limit described by (1.7) because of the rectifier loss, power overhead of the EH system operation, loading effect, and other non-ideal factors [10]. V_{AC} under open-circuit conditions is used since V_{tub} is not accessible directly. Nevertheless, the fractional value of the AC amplitude has been widely adopted for MPPT because of its simplicity and low cost, which typically ranges from 0.4-0.6 [19, 20].

In Fig. 1.17, the normalized extracted output power in simulations is plotted based on the turbine electrical model with actual rectifier circuits. The loading factor α is the ratio between V_{RECT} and V_{tub}. The optimal α is from 0.6 to 0.4 depending on the operation ranges. In the low f_{tub} range, α is close to 0.6, which is also affected by sub-threshold operations of the rectifier. For higher f_{tub} (larger V_{tub}), the optimal α is close to 0.4 as the previous analysis shows. As a compromise, an α at 0.5 still ensures an 85% to 95% extraction efficiency for the whole range.

1.4.4 The Loading Effect of Wind Turbine

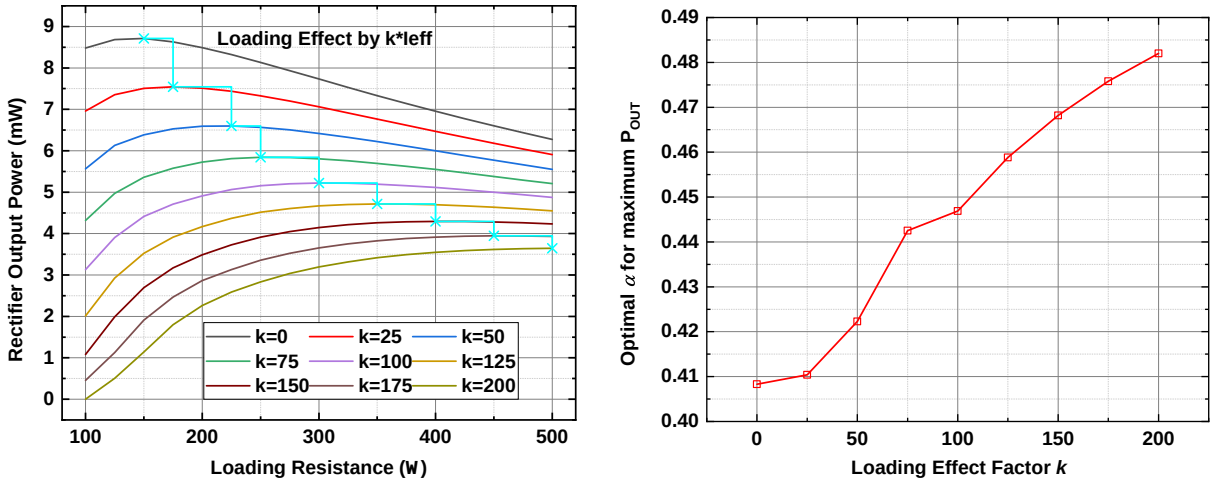

(a) (b)

Figure 1.18: Wind turbine generator's loading effects (a) in output power and (b) in optimal α.

The Loading effect of WTG is another critical factor in wind EH, which degrades the system efficiency and output power [10]. Shown in Fig. 1.15, the rotary speed of WTG is a function of wind speed and loading current. The loading current generates a counter torque to decrease the rotation frequency of WTG, which also decreases the induced voltage amplitude. Therefore, different loading conditions change the operations of WTG itself. In Fig. 1.18, the loading effect is emulated by a reverse AC voltage which is controlled by the effective loading current [V_{tubRMS}/(R_{eff}+R_{int})] with an I-to-V gain of k. In simulations, V_{PK} is 2.8 V to minimize the nonlinear effect in the rectifier. R_{int} is 100 Ω to match with the measurement results. Under the first-order approximation, the variance of the optimal loading resistance and the corresponding α are shown in Fig. 1.18a and 1.18b.

In this subsection, the nonlinear effects in rectifier operations and loading coupling effects have been discussed. And their mechanisms to degrade the system performance in practical implementations were analyzed with simulations. Moreover, to further minimize the potential performance

degradation, α is required to be programmable to determine the optimal value in field-testing.

1.4.5 Design Challenges

The wind power profile can be very sparse under different weather or climate conditions [9], which requires the system to have self-start-up and autonomous operation abilities, especially when the wind is weak or even absent. Meanwhile, the incoming wind is difficult to predict, and its speed can change drastically in a very short period [9]. Therefore, a power-efficient EH system is desired to extract the most available energy under different wind conditions and to extend its operation range close to the minimum cut-in wind speed. The system MPPT functions are supposed to be able to track this fast-changing wind power with little power consumption overhead and power adaptive operations, which accommodates different wind power conditions. Besides the fast-changing wind power profiles, non-ideal factors of the rectifier's sub-threshold operating mode and loading effect of WTG also degrade the performance of conventional MPPT methods.

1.5 MPPT Techniques Introduction

To ensure maximum power extraction, a maximum power point tracking (MPPT) method is required to optimize the overall systems performance under different power conditions [21]. Among different MPPT techniques, the open-circuit voltage V_{OC} detection is widely adopted in IC systems for its simplicity and effectiveness [20]. And it achieves very high MPPT efficiency in EH source that changes slowly or remains constant. For the DC EH source, the fractional ratio is set to be 0.5 and for the AC EH source, the optimal ratio ranges from 0.4 to 0.6.

Particularly for AC EH source like wind, the conventional V_{OC} detection is not adequate for such frequently-changing input power [20]. To provide other feasible low-cost solutions for MPPT, an auxiliary generator is used to replicate the open-circuit voltage [22]. And the internal resistance or inductance values have been examined in [11, 23, 24]. However, those techniques require an accurate model of the target EH source, which is not available for many low-profile generators. And the constant-parameter approximation is not valid for wide-range operations. Additionally, the power consumption is relatively high compared to the deliverable power because they need

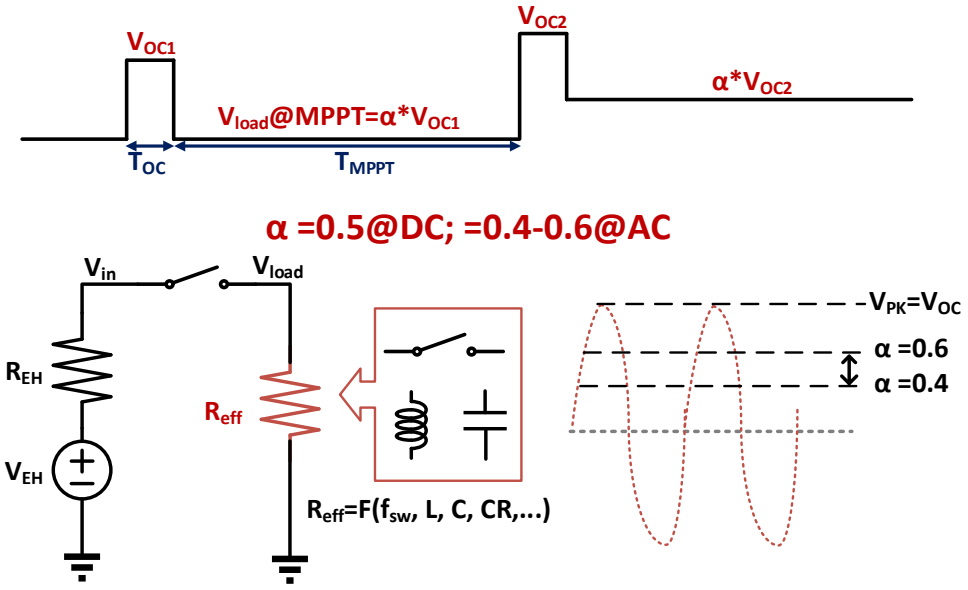

Figure 1.19: V_{OC} detection MPPT operations.

to monitor the current or voltage continuously or rely on high switching-frequency operations [24, 25]. A conduction-angle-based MPPT method is proposed in [26], but its trade-off between the response time and step resolution makes it unsuitable for fast-tracking applications. Therefore, a low-cost, low-power, and fast response method is required to ensure a real-time MPPT. In summary, the main challenges for wind EH applications are addressed in this dissertation:

- Power extraction abilities especially for low wind speed conditions
- Wide-range and high-efficient MPPT for fast-changing wind power
- Autonomous operations and adaptive to different wind conditions
- High efficiency and self-start-up and self-sustained functions

1.5.1 Open-Circuit Voltage Detection

The open-circuit voltage V_{OC} detection method is widely used in commercial EH PMU products. However, its assumption that the EH source power is almost constant is not always valid

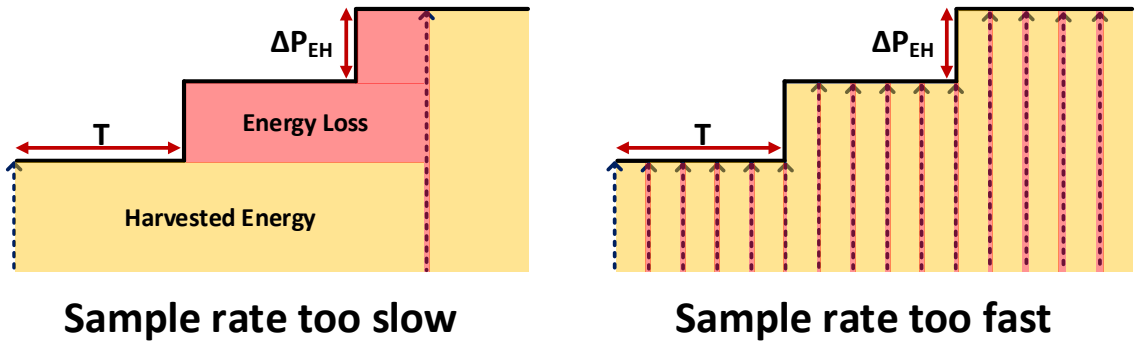

Figure 1.20: V_{OC} detection MPPT in EH source power changing conditions.

for practical applications. Moreover, the high voltage stress during the V_{OC} detection period also limits the working range for many low-voltage processes. Fig. 1.19 shows the basic operations of V_{OC} detection. With a short period of disconnection from the EH source, the V_{OC} is sampled and stored for MPPT. And in the period of T_{MPPT}, the cascading DC-DC converter regulates the loading voltage V_{load} to $\alpha * V_{\text{OC}}$, where α is the ratio between V_{load} and V_{OC}. The cascading DC-DC converter performs as an emulated loading resistance R_{eff} to match the internal EH resistance R_{EH}. Both the switched-inductor (SL) and switched-capacitor (SC) converters can be used for the V_{OC} detection MPPT. When the EH PMU is in the V_{OC} detection phase, the actual energy extraction is stopped. Therefore, to maximize the energy extractions, the typical duty ratio of the detection is minimized as 1%.

When the actual EH source power changes happen, the V_{OC} detection method cannot detect any changes until the next detection phase. As illustrated in Fig. 1.20, the extra energy is lost due to the slow sampling activities. However, if the sampling rate is increased to detect this EH source power variance, the loss due to the sampling activities is also increased to degrade the system performance. To further express this issue, Fig. 1.21 shows the quantity results in three different cases. Both case i, ii, and iii assume the EH source power is changed by 20% in certain transition rates. In case i, the change is set to be descending and it is set to be ascending in case ii. And in case iii, it assumes in every EH power transition, the original MPPT efficiency is degraded by 20% until it is updated. The actual harvested energy is normalized by the total energy, which is

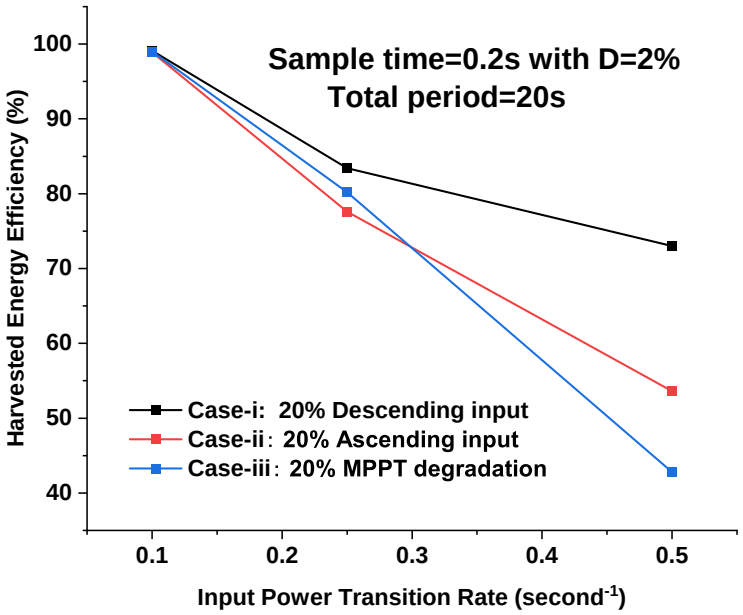

Figure 1.21: MPPT efficiency in EH source power changing conditions.

represented as the energy efficiency. Similar to the illustration in Fig. 1.20, the energy efficiency is dropped significantly when the input power is changed more frequently in all different cases.

Meanwhile, if the V_{OC} sample rate is increased to track the potential EH power changes, the power consumption of the whole EH PMU system is also increased, especially when the EH source power is sparse or even absent. In Fig. 1.22, it shows the effective power consumption of EH PMU system with different duty ratios. In idle mode, the system key circuit block can be shut down or the supply voltage can be scaled down to save power. And in active mode, all the critical circuit blocks need to be turned on. Therefore, the power overhead difference can be high as 1000x. Overall, a sufficient high duty-ratio sampling can maximize the energy efficiency in fast power changing conditions compared to the low duty-ratio sampling. However, the high power consumption introduces more energy loss when the EH power is absent. And if the sampling rate is too fast, the overall energy efficiency is even degraded with extra V_{OC} detection activities. An adaptive sampling rate could solve this problem, but it increases the overall design complexity. And how to ensure this adaptive sampling rate to track the unpredictable EH source power changes is also an important research topic for further explorations. In a brief conclusion, the major drawbacks of

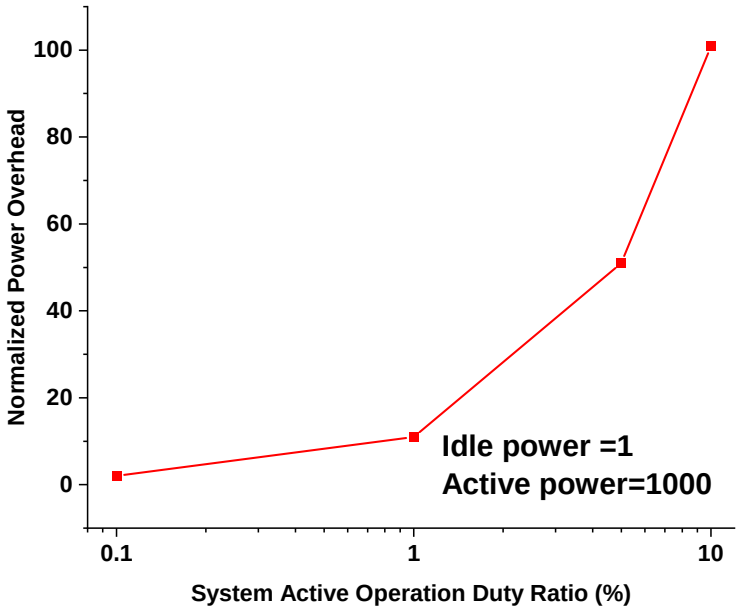

Figure 1.22: Power overhead under different duty ratio operations.

the conventional V_{OC} detection method are:

- Large voltage stress in V_{OC} detection
- Extraction interruption in V_{OC} detection
- Changes in loading conditions of EH source in V_{OC} detection
- Energy loss with outdated V_{OC}
- The fixed sampling rate, no perceptions in EH power profile

1.5.2 Resistor Emulation

As described in the V_{OC} detection method, when R_{eff} is equal to R_{EH}, the maximum power point (MPP) is achieved. In V_{OC} detection MPPT, the MPPT reference is V_{OC} and a predefined α. However, the value of R_{eff} can also be used for MPPT. The voltage and current information are both sensed and processed to get the value of R_{eff} [11]. The advantage of resistor emulation is that it does not need to disconnect the EH source and it can detect the fast-changing input power.

However, the power consumption is relatively high because it needs to process the information of current and voltage simultaneously. And this R_{eff} depends on the internal circuit parameters, like switching frequency, inductor, capacitor, and many other values, which is also sensitive to PVT variances. Moreover, for many applications in low voltage operations, such as RF EH rectifier (Fig.1.12), the optimal loading resistance shifts with the changes of input power. The resistor emulation method is reported with limited working ranges [27], or relatively low MPPT efficiency [11, 23].

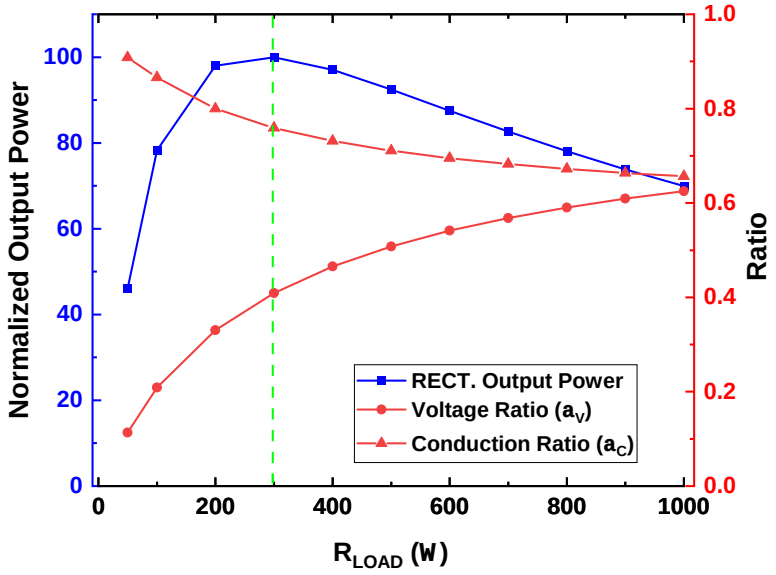

Figure 1.23: AC-DC rectifier output power with different conduction ratios and α.

1.5.3 Conduction Angle and Conduction Duty-Ratio Detection

In AC EH applications, another method to eliminate the V_{OC} detection phase is to monitor the conduction time of the rectifier [7, 26]. The rectifier switches are controlled by a comparator to minimize the conduction loss in diodes. At the same time, the duty ratio of the control signal is also an indication of MPPT conditions. As shown in Fig. 1.23, the optimal conduction ratio for maximum output power is 0.75 in simulation. In practical implementations, the conduction ratio

or conduction angle requires signal process techniques in the time domain. Therefore, it is more suitable for low frequency (around 100 Hz) applications. A nano-current charge pump with a 50-mV step response is used in [26] to determine the final MPPT reference voltage. A peak MPPT efficiency of 90% is achieved. Need to be mentioned, the MPPT operations change the rectifier's conduction ratio directly. Therefore, a small step response is required to prevent any undesired oscillations or latched-up, and it also determines the resolution of the reference voltage. However, the MPPT response is also compromised in this case, which makes it less adequate for fast power changing applications.

1.5.4 Auxiliary EH Source for MPPT Detection

Using an auxiliary EH source to provide MPPT information is also applicable for the fast power changing scenarios [22]. A downscale harvester only dedicated to MPPT can be designed to reduce the overall form factor. Although the real-time EH power variance is reflected, the different loading conditions of the main EH source and the auxiliary source decreases the MPPT efficiency. And it requires a good parameter matching between these two EH sources, which might not be available in many applications.

1.5.5 MPPT Methods Comparison

	V_{OC} Detection	Resistor Emulation	Conduction Angle	Auxiliary EH Source
MPPT Efficiency	↑	→	→	↑
MPPT Range	☺	☹	☺	☺
Power Consumption	☺	☹	☺	☺
MPPT Response	☹	☺	☹	☺
MPPT settling Time	☺	☺	☹	☺
Voltage Stress	☹	☺	☺	☹
Form Factor (Cost)	☺	☹	☺	☹
Programmability	☺	☹	☹	☹

Figure 1.24: MPPT method comparisons.

Fig. 1.24 lists the MPPT methods discussed in this section. And a comprehensive comparison is drawn among these MPPT methods. Overall, a wide-range, low-cost, and low-power MPPT with fast response and high efficiency is desired in EH PMU designs, especially for EH applications with fast-changing power conditions.

1.5.6 Dissertation Organization

Chapter 2 presents an 820-MHz reconfigurable and self-start-up RF EH rectifier with fractional open-circuit voltage approximation (FOCVA) MPPT for wide input-power ranges from -22 dBm to -2 dBm. The proposed FOCVA MPPT relieves the burden of the nonlinear tracking requirement of cascading DC-DC converter. High MPPT accuracy over 87% is achieved. Compared to conventional fixed-stage rectifier, the design achieves $2\times$ ($+19\%$) peak efficiency improvement and the high-efficiency range (η_{Rect} >20%) is improved by 14 dB.

Chapter 3 introduces a 915-MHz reconfigurable 12-stage rectifier with fully-integrated MPPT functions. The rectifier sensitivity is -18.1 dBm for 1-MΩ loading and its peak efficiency is 36% peak efficiency at 1 dBm. The proposed MPPT function can detect and determine the optimal rectifier stage for loading from 10 KΩ to 1 MΩ, with a peak MPPT power efficiency of 99.8%. Measurements also show the system can achieve self-start-up and self-sustained functions with a 10 μF external capacitor buffer.

Chapter 4 proposes a dual-band energy harvesting system operating at GSM-900 (900 MHz) and WLAN (2.4 GHz) bands. To harvest the RF energy from the WLAN band more efficiently, an event-triggered 1:2 parallel-series SC converter is proposed to reduce the reverse leakage current. Meanwhile, this fully-integrated SC converter can provide an output voltage bootstrapping function while maintaining an ultra-low-power consumption down to 28 nW by asynchronous control. Measurement results have shown the PMU can boost up the output voltage by $1.73\times$ with an input voltage as low as 0.2 V. When harvesting the modulated waveform, the RF-EH system output ripple is decreased by $6\times$, and reverse leakage current reduction is over $2500\times$ compared to the direct connection condition.

Chapter 5 presents an EH system to extract the energy from a cm-scale EM wind turbine. To

improve the efficiency of such an EH system, an autonomous and self-biased active rectifier is employed. Also, a novel frequency-to-amplitude conversion (FAC) MPPT method is proposed for cycle-to-cycle MPPT. In wind-field testing for wind speeds from 1.0 to 5.0 m/s, the peak MPPT accuracy is 99.27% with a MPPT efficiency of 99.85%. The extracted power is from 0.1 to 10 mW with a peak end-to-end efficiency of 88.2%. Compared to a full-bridge rectifier, a 630% energy extraction gain is measured at a low wind speed of 1.2 m/s.

Chapter 6 concludes the dissertation by reviewing the main achievements which have been done associated with this dissertation work.

2. RECONFIGURABLE RF EH SYSTEM WITH FOCVA MPPT FOR CASCADING DC-DC CONVERTER [1]

2.1 Introduction

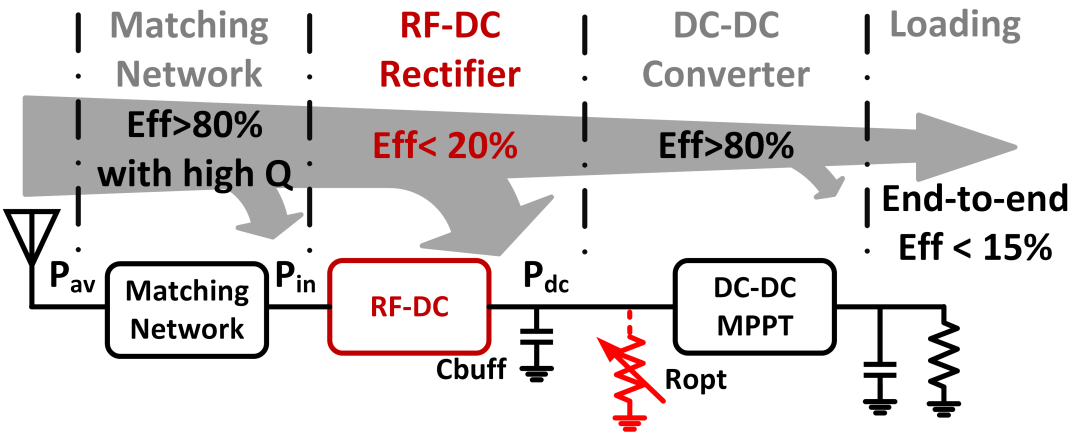

Figure 2.1: RF energy harvesting system with a DC-DC converter.

Fig. 2.1 shows a conventional RF harvester with a DC-DC converter and the bottleneck is still on the rectifier efficiency itself. The typical efficiency of a rectifier is less than 20% in microwatt power conditions. What's worse, the rectifier's output voltage is changing with the input available power, which could be below 0.2 V for low input power and over 3.0 V for high input power. Designing a DC-DC converter with a such large input voltage range would be a challenge especially for the limited power budget. Different up/down and both types of DC-DC converters have been proposed for RF energy harvesting and it increases design complexities [8, 27, 28, 29, 30]. Meanwhile, it is also very difficult to maintain the rectifiers optimal efficiency in such a wide input power range. Therefore, a high-efficiency rectifier with an effective control scheme for a wide

[1] Part of this chapter is reprinted with copyright permission, from Z. Zeng, J. J. Estrada-López, M. A. Abouzied and E. Sánchez-Sinencio, "A Reconfigurable Rectifier With Optimal Loading Point Determination for RF Energy Harvesting From -22 dBm to -2 dBm," in IEEE Transactions on Circuits and Systems II: Express Briefs, vol. 67, no. 1, pp. 87-91, Jan. 2020.

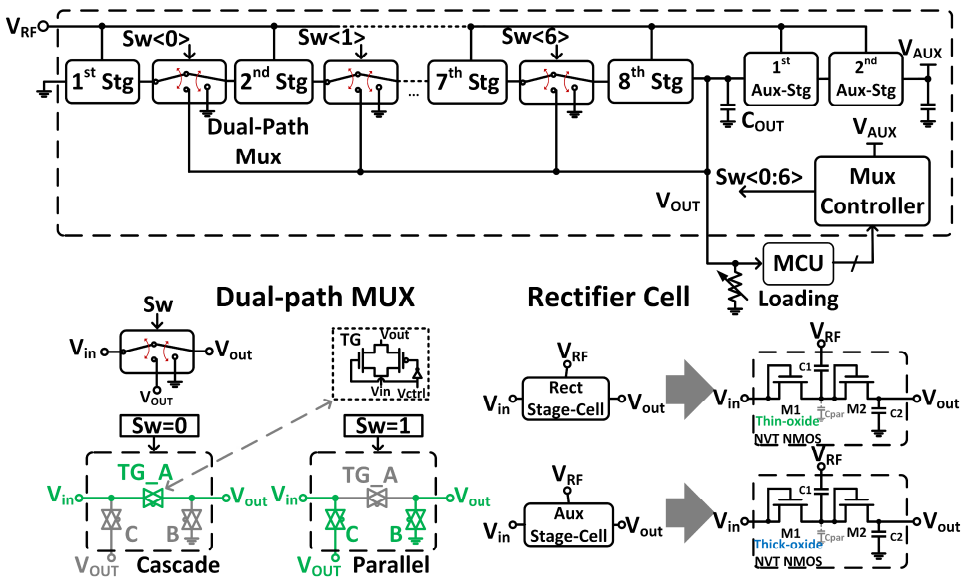

Figure 2.2: Proposed 8-stage reconfigurable rectifier schematic.

input power range is vitally important to improve the overall system end-to-end efficiency.

This work is to design a wide input power range RF-EH system with an accommodated optimal loading point determination method. Section 1.2 will show (A) Circuit design and analysis; (B) Conventional method for optimal loading and (C) Proposed FOCVA method. Measurement results are summarized in Section 1.3 and Section 1.4 concludes this work.

2.2 Proposed Solutions and Implementation

Fig. 2.2 shows the reconfigurable rectifier design. The rectifier topology is based on the Dickson rectifier with thin-oxide native NMOS. 8 stages are chosen to provide 8, 4, 2 and 1-stage configuration by digital control. In low power mode, all the stages are cascading to generate higher voltage by increasing output resistance. In high power mode, all the stages are in parallel to generate a current combination with smaller output resistance. The dual-path multiplexer provides the path to the next stage or bypasses it to final output. To achieve self-start up and self-sustain functions in low voltage, an auxiliary two-stage rectifier is designed to power up the controller internally. To handle large voltage stress, thick-oxide native NMOS is used in auxiliary rectifier.

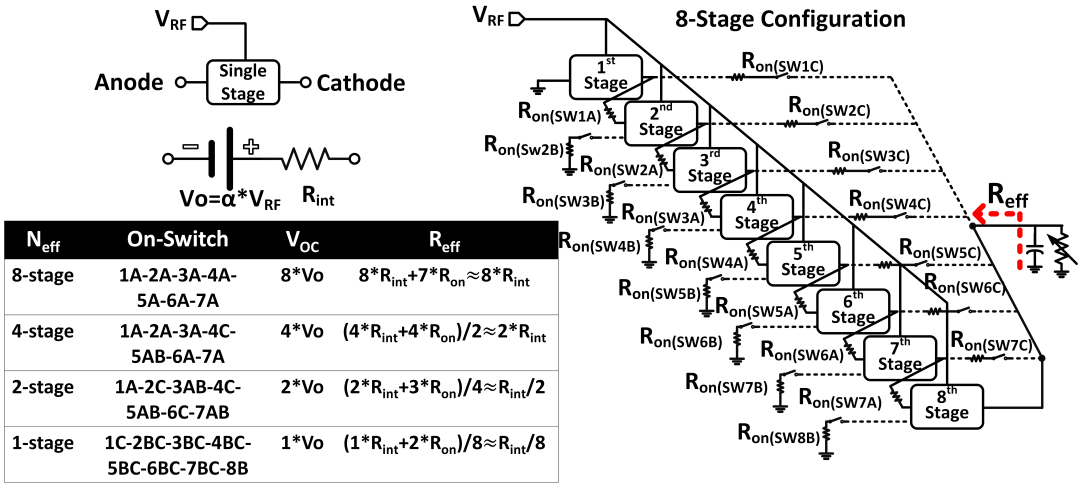

N_{eff}	On-Switch	V_{OC}	R_{eff}
8-stage	1A-2A-3A-4A-5A-6A-7A	8*Vo	$8*R_{int}+7*R_{on}\approx 8*R_{int}$
4-stage	1A-2A-3A-4C-5AB-6A-7A	4*Vo	$(4*R_{int}+4*R_{on})/2\approx 2*R_{int}$
2-stage	1A-2C-3AB-4C-5AB-6C-7AB	2*Vo	$(2*R_{int}+3*R_{on})/4\approx R_{int}/2$
1-stage	1C-2BC-3BC-4BC-5BC-6BC-7BC-8B	1*Vo	$(1*R_{int}+2*R_{on})/8\approx R_{int}/8$

Figure 2.3: Reconfiguration output resistance analysis.

Compared to other similar configuration designs in [31, 32], which both require a certain output voltage at 1 V with large output capacitor and complicate configure method, this work can achieve a much lower start-up voltage as 0.4 V, more simple and wide range method to detect optimal loading point, generating moderate output voltage range suitable for various RF energy harvesting application interfaced with DC-DC converter. An off-chip controller, AT-mega MCU is used to control the rectifier and evaluate the performance of the proposed MPPT method. The MCU power is excluded in this work because the MCU is only used for design validation and the system can be implemented with a fully-integrated solution.

2.2.1 Reconfigurable Rectifier Output Impedance Analysis

All the rectifier configurations are shown in figure 2.3, all the multiplexer switches are simplified as parasitic resistance. R_{eff} represents the effective output resistance of the RF-DC rectifier for optimal power extraction. N_{eff} is the effective rectifier stage number. RF port is input interfaced with matching network and antenna. The output is connected to 20 pF on-chip capacitor and off-chip loading resistance. Although R_{eff} itself highly depends on technologies and design parameters [7, 6], it can be controlled effectively by rectifier stage N_{eff}. Simply, each rectifier single cell could be regarded as a DC voltage source with internal resistance R_{int}. Here we assume R_{int}

is constant to provide straightforward intuition for analysis. The open-circuit output voltage along with effective R_{eff} is changed by parallel/cascade configuration. Normally R_{int} is ranging from 10 to 100 KΩ therefore the parasitic R_{on} is negligible. For different configurations from fixed N_0=8 stage, N_{eff} equals $1, 2, 4,$ and 8. And the R_{eff} will be R_{int}/8, R_{int}/2, R_{int}*2, and R_{int}*8 respectively, which means the output power is higher with smaller N_{eff} with similar output voltage. For example when N_{eff}=4, two 4-stage rectifiers are connected in parallel therefore the effective R_{eff} is R_{int}*2.

Although rectifier operation is nonlinear, it can be approximated as a resistive source for a certain working range [27]. Such approximation is still valid for wide range operation because each rectifier configuration only covers for a limited working range. Ideally, when the loading resistance is close to rectifier output impedance, the optimal loading point appears near half of the open-circuit voltage. Therefore the MPPT is achieved in a wide range operation by adjusting the equivalent loading resistance through the cascading DC-DC converter.

To better explain the effect on efficiency, our assumption is (1) All the transistors and capacitors are identical. (2) Body effect is ignored. (3) Parasitical resistance and capacitor due to reconfiguration multiplexers are ignored. (4) Stage rectifier cell performance is independent of output current and output voltage. (5) Rectifier input impedance from the RF port is similar among different configurations [7, 6, 33]:

$$V_{OUT} = N_{eff} * (\frac{C}{C + C_{par}} * V_{RF} - V_{th} - V_{loss}) \tag{2.1}$$

$$\eta_{Rect} = \frac{\frac{V_{OUT}^2}{R_{load}}}{\frac{V_{OUT}^2}{R_{load}} + P_{loss} * N_{eff}} \tag{2.2}$$

$$Zin_{Rect} = \frac{Zin_{Stage}}{N_0} \tag{2.3}$$

C is the stage capacitor in each stage rectifier and C_{par} is representing the parasitic capacitor. V_{RF} is the voltage swing seen in the rectifiers input. V_{th} is the transistor threshold voltage and V_{loss} is representing voltage drop due to loading current and leakage current. η_{Rect} is RF-DC power conversion efficiency of rectifier and our design focus is only on η_{Rect} because it is the dominant

parameter in total efficiency. Typically, V_{OUT} is maximized in certain stage number N_{eff} and V_{RF} to get maximum efficiency by decreasing C_{par}, V_{th}, and V_{loss}. Although the internal switch implementation will increase P_{loss}, N_{eff} is still the dominant factor for η_{Rect}. This also explains why designers prefer smaller N_{eff} for target output voltage or power to get better efficiency. And when the output voltage is exceeding the required voltage level, decreasing N_{eff} by reconfiguration can maximize the efficiency. Zin_{Rect} in (3) is the input impedance from the RF input port. It is reverse proportional to N_0 because all the stage rectifier is equivalent to a parallel connection to the RF port. As long as each rectifier is connected to the RF port through the coupling capacitor, this N_0 will remain unchanged in equation (3). As pointed out in [5], Zin_{Rect} is also dependent on output voltage V_{OUT}. Therefore, changing N_{eff} to limit V_{OUT} changes can also help to suppress the changes of Zin_{Rect}. Our design starting point is based on equation (1) and (2), with target input power and output voltage requirement, the efficiency is maximized by sizing and selection of stage number. And then the working range is extended thanks to the reconfigurable stage number.

2.2.2 Conventional Optimal Loading Determination

Conventionally, the optimal loading resistance for RF energy harvester is difficult to model or predict because of its non-linear nature. And its value together with the ratio to open-circuit voltage V_{OC} is also changing with input power, which makes it is more difficult for tracking [8]. Although observed in [27], the optimal loading resistance is almost constant, it is only valid in a very limited input power range. Therefore, in various RF energy harvester publications, different loading resistance is used to optimize for different input power levels [34]. However, the methodology to choose such optimal resistance is still missing. The optimal loading point is even more difficult to track for a wide input power range and in [30], a time-based MPPT for buck-booster is used to estimate the input power and overcome the nonlinear effect but it requires a large capacitor array and long integration time to achieve wide-range operation. All the previous MPPT methods are proposed rather for limited operation range or required complicated circuitry and control. We observed each rectifier configuration is working only for a certain limited input power range, therefore a constant loading resistance for each rectifier configuration can be used. Then each limited

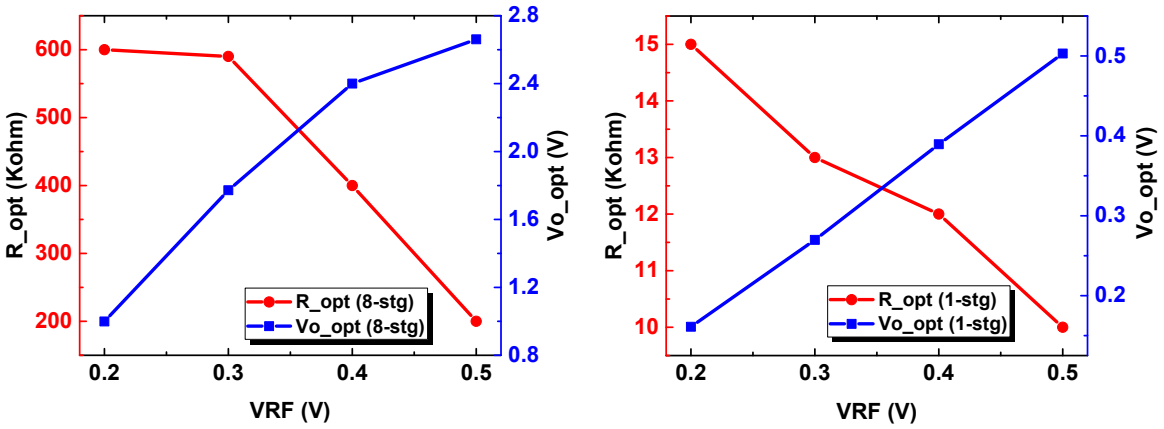

Figure 2.4: Comparison of optimal loading and V_{OUT} in 8-stage and 1-stage.

working range can be combined without overlap to generate a large input power range with the help of reconfiguration.

Fig. 2.4 shows the simulation results of the optimal output voltage and corresponding loading resistance for the 8-stage and 1-stage configurations. By sweeping V_{RF} from 0.2 V to 0.5 V, the equivalent input power is similar, ranging from 5 to 50 μW. The optimal loading resistance is changed up to 67% with fixed stage design, causing the complexity for maximum power point tracking. However, if the V_{RF} range is limited (V_{RF}=0.2 to 0.3 V in 8-stage, 0.4 to 0.5 V in 1-stage), the optimal loading resistance changes will be minimized, therefore the fixed optimal loading can be used.

2.2.3 Fractional Open-Circuit Voltage Approximation (FOCVA)

To determine the optimal loading point without introducing too much complexity, a novel FOCV Approximation method is proposed for wide input power range operation. Although FOCV is not typically used in RF energy harvesting applications, analysis and simulation results indicate its effectiveness with such quasi-resistive approximation.

As shown in Figure 2.5, simulation results show a ratio of 0.5 is a very good approximation to get maximum output efficiency across different input power, overall efficiency accuracy is above 95% compared to the maximum efficiency point. Another observation is that optimal loading

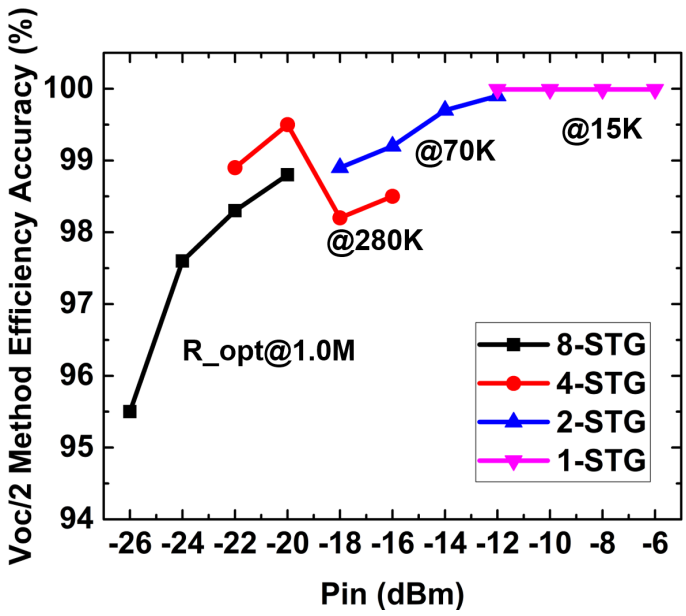

Figure 2.5: FOCVA efficiency accuracy (simulation).

resistance is unchanged with such a method, which also justified our previous statement that in small input power range, the optimal loading resistance is almost constant. Efficiency accuracy here is the ratio between η_{PCE} of fractional V_{OC} method ($V_{\text{O}}/V_{\text{OC}}$=0.5) and captured maximum η_{PCE} through different loadings. Test-bench is also including an L-C matching network and the inductor Q is 30, which shows the proposed FOCVA Method can also work along with the fixed matching network.

2.3 Measurement Results

The chip micrograph with the test bench is shown in Fig. 2.6. The whole system is fabricated in the IBM-130nm process and the reconfigurable rectifier layout area is 450μm*70μm including a two-stage auxiliary rectifier. The digital controller for switch configuration is 80μm*10μm. A reference design of an 8-stage fixed rectifier is also fabricated for comparison. The reference design layout is 180μm*60μm with identical stage rectifier cells. Figure shows the test bench and design layout photograph. To evaluate the real absorbed power, effective input power is calibrated with S_{11} parameters by Vector Network Analyzer. η_{Rect} with external fixed power source is plotted. And then external power source is placed with the internal V_{AUX}, representing the self start-up

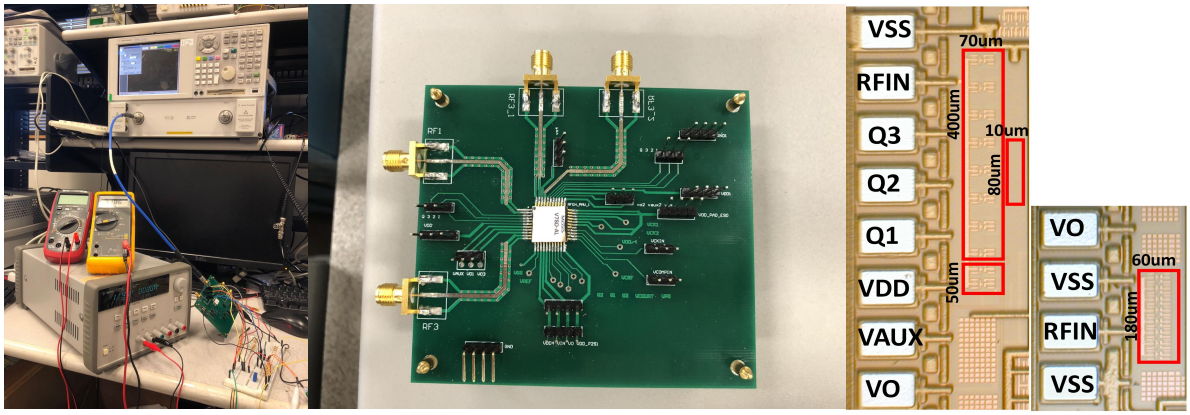

Figure 2.6: Circuit test-bench and design chip micrograph.

performance.

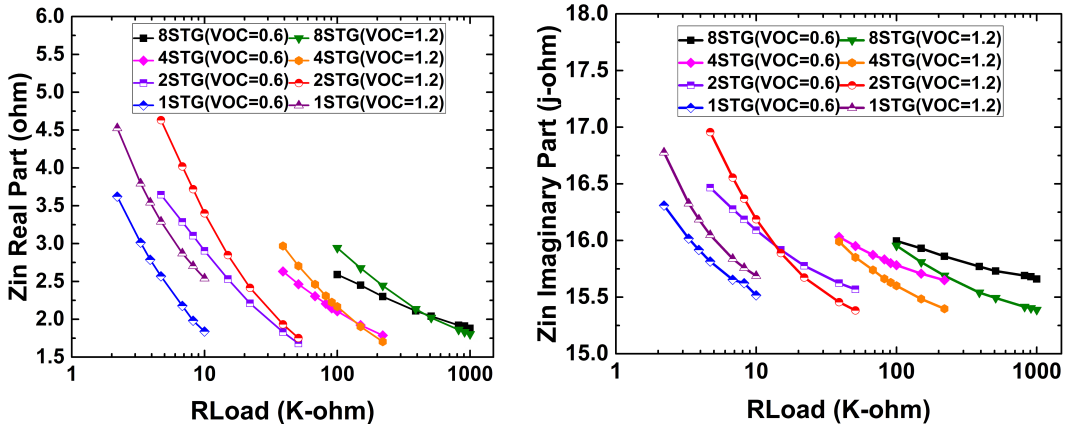

Figure 2.7: Rectifier Z_{in} real and imaginary part measurement.

In Fig. 2.7, the Z_{in} real and imaginary parts are plotted from the S_{11} parameter measurement at 820 MHz with different configurations. The typical value of Z_{in} is $2.3 + 15.9 * j\ \Omega$ because of parasitic inductance from bonding wire, LQFP package, and FR4 PCB trace. Both the real and imaginary parts are changed with the loading. It explains why the rectifier with fixed matching efficiency degrades in higher loading current conditions. And it also shows that the reconfiguration design suppresses this undesired S_{11} shifting in a larger input power range.

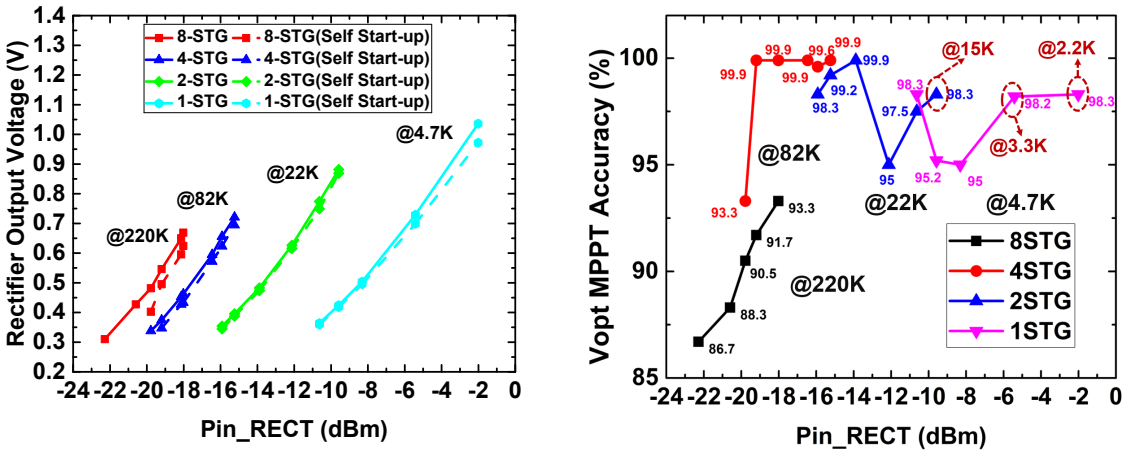

(a) (b)

Figure 2.8: (a)Rectifier V_{OUT} (b) FOCVA MPPT accuracy.

Fig. 2.8a shows the rectifier output voltage V_{OUT} when fixed loading is applied within each configuration. The output voltage is ranging from 0.3 V to 1.0 V. It is exceeding the target output voltage of 0.3 to 0.72 V (ratio of 0.6) because, in the high-power range, the optimal resistance from FOCVA is decreased. However, for a better comparison, rectifier performance with fixed loading is used considering the efficiency absolute difference is $< 3\%$ compared to optimal resistance.

Fig. 2.8b summarizes our proposed FOCVA MPPT accuracy performance in target input power. The maximum error compared to 0.6 is 0.08, thus the overall accuracy is over 86.7%, where MPPT accuracy is defined as the ratio of the real measured fractional value of the optimal point to the predefined ratio 0.6, indicating the effectiveness of our proposed method. Rectifier open-circuit output voltage V_{OC} is kept in 0.5 to 1.2 V by controlling the N_{eff} stage number, then different loading resistance is selected for V_{OUT} to reach the target fractional value. Measurement results show that V_{OUT}= V_{OC}*0.6 is a good estimation value to determine the optimal loading from -22 to -2 dBm, $100\times$ ranging from 6.3 μW to 630 μW. The maximum voltage for the process is 1.2 V and if the maximum voltage requirement is relaxed, this FOCVA method and the rectifier working range could be further increased to a higher power level. The reason fractional ratio changes from 0.5 in the simulation because here the real input power is calibrated by the S_{11} pa-

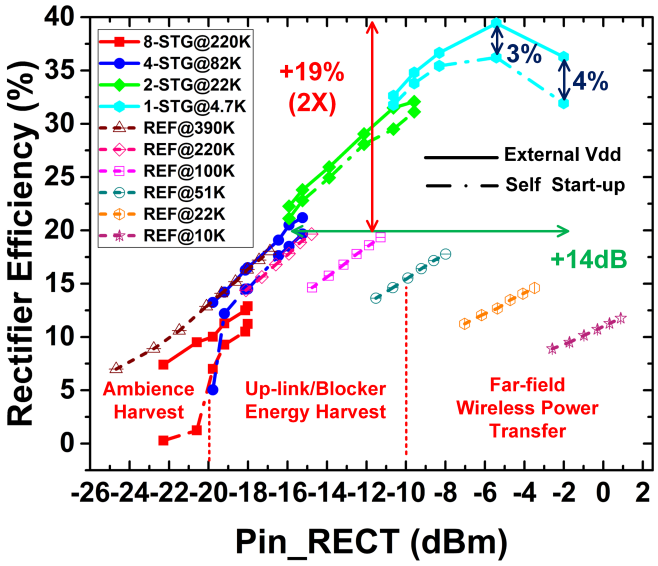

Figure 2.9: Rectifier power conversion efficiency comparison.

rameter to characterize rectifier performance, assuming ideal matching with tracking functions as [5]. The loading resistance is almost constant with every configuration excluding some extreme cases.

Fig. 2.9 shows the measurement results of rectifier power conversion efficiency among the fixed-stage reference and reconfigurable design with or without self start-up. External Vdd performance is used to compare because the V_{AUX} can be replaced with a stable voltage source in steady-stage in DC-DC converter involved applications and the power consumption of the controller is negligible compared to the output power, which is mainly dominant by the leakage current. The fixed stage rectifier is identical to an 8-stage rectifier without any switches for a fair comparison. For reference designs output, the requirement is relaxed to be 0.3 to 1.2 V without detecting V_{OC}.

Measurement results show our proposed reconfigurable rectifier can work with input power from -22 dBm to -2 dBm. The Self-start-up performance difference is less than 2% except for the low-power range (-22 to -20 dBm) and extreme high-power range (-6 to -2 dBm). The first case is because, in low input power, the auxiliary rectifier output V_{AUX} is not high enough to minimize switch conduction resistance. The second case is because the leakage current through the

ESD diode is more severe with higher V_{AUX}. However, from -20 dBm to -2 dBm working range, the whole efficiency difference is less than 4%. Each reconfigurable stage has a very small overlap region with its adjacent states with proposed FOCVA, which avoids state redundancy compared to other similar counterparts without any clear boundaries. To have better performance in the low-power range, more auxiliary stages can be used but efficiency loss is more severe in the high-power range.

Compared with the reference design, the efficiency for fixed stage design is only better in extreme case smaller than -20 dBm. Overall, our proposed reconfigurable design is better from -15 dBm to -2 dBm. The comparison shows that our proposed design can achieve $2\times$ peak efficiency improvement (+19%) with a high-efficiency range extension (+14 dB), sacrificing little sensitivity performance (<3%). It means our purposed reconfigurable design is extending the working range significantly and it can be configured to work with different applications, from microwatt ambient energy harvest, upper link energy harvest, and potential wireless power transfer or short distance RFID applications.

Table 2.1 summarizes the overall performance and comparison in literature. Our work shows the best sensitivity in -22 dBm and a higher peak power efficiency of 39% compared to [31] in static state performance. Overall peak efficiency is improved by 19% and the high efficiency working range is extended by 14 dB compared to reference design. Compared to work [4, 35], our work can achieve both wide input range and peak efficiency improvement simultaneously. For DC-DC regulator assisted energy harvesting applications, our work can provide a moderate output voltage from 0.3 to 1.0 V with fixed loading resistance for each configuration, and 0.3 to 0.72 V with FOCVA ratio = 0.6, improving rectifier efficiency and relieve following booster voltage gain requirements. For example, for a typical 1.2 V supply voltage requirement, it only needs the voltage conversion gains from 1.67 to 4, while other work in comparison will need up and down voltage converter.

Table 2.1: Literature review and comparison of RF EH rectifier with FOCVA.

	[4]	[31]	[35]	This Work
Freq.(MHz)	953	915	900	820
Tech. (nm)	130	180	65	130
Topology	CC-LDCF 3-stage	Vth-Compensated (1-2-4-8)	Dual-Path CC (5-stage)	Dickson (1-2-4-8)
Vout (V)	0.1 - 4.5	0.2 - 2.0	1.0 - 2.8	0.3 - 0.7
PCE_peak	70%@ 6dBm	27%@ -2 dBm[1]	30%@ -17.7 dBm[1]	39%@ -5 dBm
Sensitivity	4% @ -7dBm	7%@ -14.8 dBm[1]	30%@ -17.7 dBm[1]	7.5%@ -22 dBm
PCE_peak Improvement	+9.5%	NA	No	+19 %
PCE Range >20% (dBm)	-3 - 11 14 dB	-7 - 3 10 dB	-16 - -7 11 dB	-16 to -2 14 dB

[1] MN + Rectifier static state performance, captured from figures

2.4 Conclusion

An RF-EH system based on a reconfigurable rectifier is designed for a wide input power range and maintain high efficiency from -22 dBm to -2 dBm. The final output is designed to be 0.3 to 0.7 V with FOCVA and suitable for following boost converter to perform MPPT. Compared to conventional Dickson rectifier, this design peak efficiency equals to 39%, with 19% peak efficiency improvement and the high-efficiency range >20% is from -16 dBm to -2 dBm. With the help of reconfigurable structures, Fractional Open-Circuit Voltage Approximation Method (FOCVA) is proposed for optimal loading determination in a wide input power range. Simulation and measurement results show our proposed method can achieve good MPPT accuracy in the whole range from -22 dBm to -2 dBm, with MPPT accuracy over 86%. Compared to the existing MPPT method in literature, our method can achieve simplicity and accuracy simultaneously. In future work, a DC-DC converter could be designed with MPPT functions based on our proposed FOCVA method to maximize EH power extraction.

3. RECONFIGURABLE RF EH SYSTEM WITH FULLY-INTEGRATED HILL-CLIMBING MPPT ON RESISTIVE LOADINGS[1]

3.1 Introduction

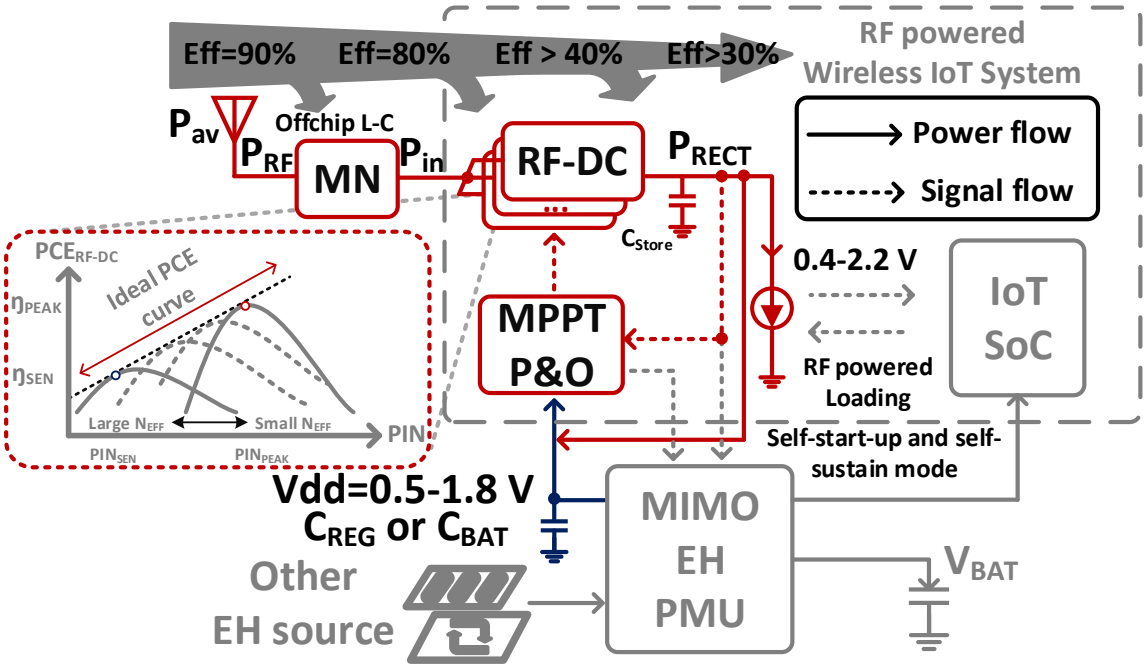

Figure 3.1: Proposed RF-EH system for MIMO-EH enabled Wireless IoT.

Fig. 3.1 shows our purposed RF-EH involved system. The end-to-end RF-EH efficiency in a conventional system is relatively low mainly because of the power conversion loss and the long cascading power-delivery path. Instead of cascading the power converter to the rectifier, our proposed solution provides a direct power-delivery path to the internal SoC block. The power-management-unit (PMU) only needs to provide a scalable voltage source for the controller and assist in load selection. The interface control can be simple and efficient because the major MPPT function is

[1]Part of this chapter is reprinted with copyright permission, from Z. Zeng et al., "Design of Sub-Gigahertz Reconfigurable RF Energy Harvester From -22 to 4 dBm With 99.8% Peak MPPT Power Efficiency," in IEEE Journal of Solid-State Circuits, vol. 54, no. 9, pp. 2601-2613, Sept. 2019.

integrated with the RF-EH system itself to adjust the rectifier stage number optimized for different input-power conditions. And the system can be configured with self-start-up and self-sustained functions to ensure the whole system robustness when the alternative EH power source is absent or the battery is fully depleted.

Additionally, the internal capacitor buffer is charged up to the desired voltage level more quickly. It is beneficial for efficient usage of the incidental RF power because the available RF power is difficult to predict, whose dynamic power density profile highly depends on the user behaviors. The peak power can be high as 1.9 mW (2.8 dBm) with a typical duration time from 0.1 to 2 s in the up-link communication[36, 2]. And if constant power source exists, our system can also work with a big capacitor buffer for energy storage. Another advantage is that our proposed topology can break the contradiction between large-range rectifier output voltage and high battery voltage. Thus the harvested efficiency is increased by minimized voltage conversion loss. The scaled supply voltage can minimize the power overhead. The system operation range is also extended by the lower sensitivity requirement. In this work, a RF-EH system with co-designed antenna and an integrated hill-climbing MPPT controller is proposed to optimize the overall efficiency and provide efficient control. Section 2.2 illustrates the analytical model and circuit implementation. Section 2.3 shows the measurement results for validation and Section 2.4 summarizes the achievements of this work.

3.2 Proposed Solution and Implementation

3.2.1 Reconfigurable Rectifier Design and System Overview

Our proposed system includes a reconfigurable rectifier and a digital MPPT control block. The reconfigurable rectifier is the key circuit block needed to improve efficiency and to extend the working range. This work is an extended version of [32] with more detailed analysis and an optimized system integration. Fig. 3.2a shows the rectifier details. The rectifier stage cell is connected to the next stage cell through the dual-path multiplexer in the cascade phase, otherwise, it will be connected to the final output in the parallel phase. Meanwhile, another ground connection

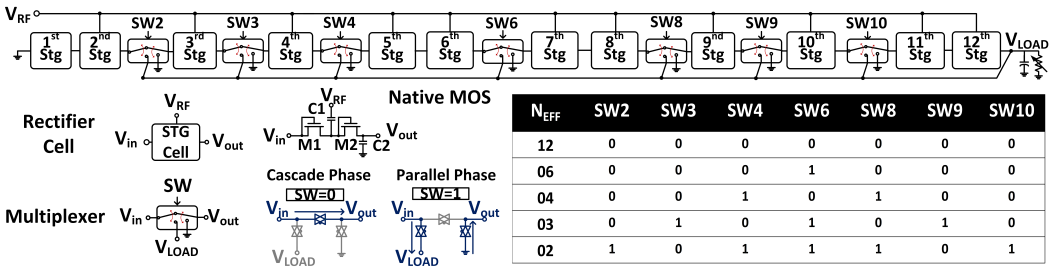

N_{EFF}	SW2	SW3	SW4	SW6	SW8	SW9	SW10
12	0	0	0	0	0	0	0
06	0	0	0	1	0	0	0
04	0	0	1	0	1	0	0
03	0	1	0	1	0	1	0
02	1	0	1	1	1	0	1

(a)

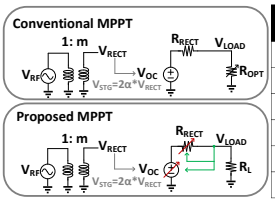

N_{EFF}	R_{RECT}	V_{OC}
N_0=12	$N_{EFF}/(N_0/N_{EFF})*R_{STG}$	$N_{EFF}*V_{STG}$
12	$12*R_{STG}$	$12*V_{STG}$
06	$3*R_{STG}$	$6*V_{STG}$
04	$(4/3)*R_{STG}$	$4*V_{STG}$
03	$(3/4)*R_{STG}$	$3*V_{STG}$
02	$(1/6)*R_{STG}$	$2*V_{STG}$

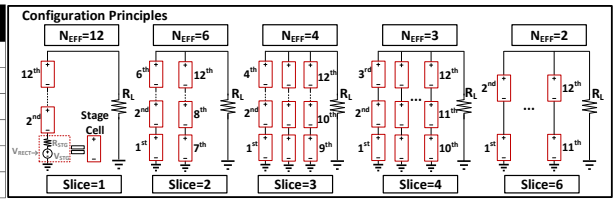

(b)

Figure 3.2: 12-stage reconfigurable rectifier (a) schematic and (b) rectifier MPPT principle model.

is generated at the input of the next stage cell to start a new rectifier slice. Configurations 12-6-4-3-2 are provided with listed control signals in Fig. 3.2a. For example, when the control signals are all zeros, all the multiplexer will connect the rectifier stage cell in cascade to generate a 12-stage configuration ($N_{\text{EFF}} = 12$). And for a 2-stage configuration with six 2-stage rectifiers connected in parallel, control signals SW2-4-6-8, and SW10 are at a high level to connect stage cell output to the final output node, while SW3 and SW9 remain zeros for cascade connection.

The rectifier is based on single-ended Dickson rectifier with Native NMOS for low voltage operation. All rectifier stage-cells are identical with a stage capacitor 200 fF to ensure a fast response. The switch number is optimized as shown by Fig. 3.2a. Compared to 12-2 configuration using five dual-path multiplexers, the proposed configuration is only using seven multiplexers to provide 12-6-4-3-2 five configurations, with the addition of three more configurations by just adding two more multiplexers.

3.2.2 MPPT Basic Concept and Analysis

Fig. 3.2b also shows the principle model for MPPT analysis. Here V_{RF} is the antenna voltage. V_{RECT} is the voltage at the RF node after ideal matching. The R_{RECT} is the effective rectifier output resistance, and R_{STG} is the inherit output resistance of each rectifier cell. Simply, R_{RECT} equals to $N_0 \times R_{\text{STG}}$ in a fixed N_0 stage rectifier. R_{OPT} is the optimal loading R_{L} for maximum power extraction. For analysis simplicity, it is assumed when R_{RECT} equals R_{L}, the power extraction is maximum [37]. The rectifier can be simplified as an ac-controlled dc-voltage source with a large internal resistance. The reconfigurable principles are also described in Fig. 3.2b. In a reconfigurable N_0 stage rectifier, N_{EFF} configuration means that N_{EFF} stage rectifier with the equivalent output resistance $N_{\text{EFF}} \times R_{\text{STG}}$ are configured and connected in parallel. The slice number is N_0/N_{EFF}. Therefore, effective R_{RECT} is calculated as ${N^2}_{\text{EFF}}/N_0 \times R_{\text{STG}}$ in (3.2). Conventionally, MPPT is achieved by adjusting R_{OPT} by DC-DC converter which generates additional loss and increases system complexity. Wide-range operation is also challenging because the R_{OPT} varies with input power and it requires a large tuning ability [38]. What's worse, the rectifier efficiency is not optimized for wide input-power conditions. In this work, our proposed MPPT is tuning R_{RECT} and the effective stage number N_{EFF} simultaneously to match the loading R_{L}, which can suppress the nonlinear variance of R_{RECT}, limit the output voltage range, and improve the rectifier efficiency with low cost solutions.

$$V_{\text{OC}} = N_{\text{EFF}} \times V_{\text{STG}} \tag{3.1}$$

$$\text{where } R_{\text{RECT}} = \frac{{N^2}_{\text{EFF}}}{N_0} \times R_{\text{STG}},\ V_{\text{STG}} = 2\alpha \times V_{\text{RECT}}. \tag{3.2}$$

V_{OC} is the rectifier open-circuit output voltage and V_{STG} is the open-circuit voltage of each rectifier cell. α is the RF-DC voltage conversion ratio in open circuit conditions. N_{EFF} is reconfigurable among 12, 6, 4, 3 and 2, and their corresponding R_{RECT} and V_{OC} are listed in Fig. 3.2b. Each rectifier cell is connected in series or in parallel; therefore, the effective output impedance is tuned from $12 \times R_{\text{STG}}$ to $1/6 \times R_{\text{STG}}$ discretely. Such methods are proved to be efficient in

thermoelectric generator, PV cell and rectenna array [39, 40, 37].

In a large stage number rectifier, the output voltage range is large because of its large internal resistance. Tuning stage number through a series/shunt combination can adjust internal resistance and output voltage. Meanwhile the stage capacitor is reused and transistor width is combined in parallel phase to limit the input impedance changes and suppress output ripples [41, 42]. Here we assume when $V_{\mathrm{LOAD}} = 0.5 \times V_{\mathrm{OC}}$, namely load-matching point, P_{OUT} is maximized as resistive source. While this is not always true for the rectifier non-linear operation, it can provide an effective approach for MPPT analysis. The analysis for the MPPT operation follows:

3.2.2.1 Load-Matching Point Analysis

$$V_{\mathrm{LOAD}} = \frac{N_{\mathrm{EFF}} \times V_{\mathrm{STG}} \times R_{\mathrm{L}}}{R_{\mathrm{L}} + (\frac{N^2{}_{\mathrm{EFF}}}{N_0}) \times R_{\mathrm{STG}}} \tag{3.3}$$

$$P_{\mathrm{OUT}} = \frac{V^2{}_{\mathrm{LOAD}}}{R_{\mathrm{L}}} = \frac{N^2{}_{\mathrm{EFF}} \times V^2{}_{\mathrm{STG}} \times R_{\mathrm{L}}}{(R_{\mathrm{L}} + (\frac{N^2{}_{\mathrm{EFF}}}{N_0}) \times R_{\mathrm{STG}})^2} \tag{3.4}$$

$$\text{For maximum } P_{\mathrm{OUT}}, N_{\mathrm{EFF}} = \sqrt{\frac{R_{\mathrm{L}} \times N_0}{R_{\mathrm{STG}}}} \tag{3.5}$$

To further examine rectifier power conversion efficiency η_{PCE}, the RF input power is needed:

$$P_{\mathrm{RFIN}} = \frac{V^2{}_{\mathrm{RECTrms}}}{Z_{\mathrm{IN}}} = \frac{N_0 \times V^2{}_{\mathrm{RECT}}}{2 \times Z_{\mathrm{IN_{STG}}}}. \tag{3.6}$$

Z_{IN} is the effective input impedance of the rectifier RF port and because in the RF node, all the rectifier stages are connected parallel to the RF node through the coupling capacitor. Therefore, Z_{IN} is equal to $Z_{\mathrm{IN_{STG}}}/N_0$ where $Z_{\mathrm{IN_{STG}}}$ is the input impedance of each stage cell. Notably, the change in N_{EFF} is proved in [38] to have a negligible effect on Z_{IN} because all the stage cells are always connected and rectifying. This statement is also verified through the S_{11} measurement indirectly in the latter part (Fig. 3.11b). And we can rewrite the equation of P_{OUT} from (3.2), (3.4) and (3.5):

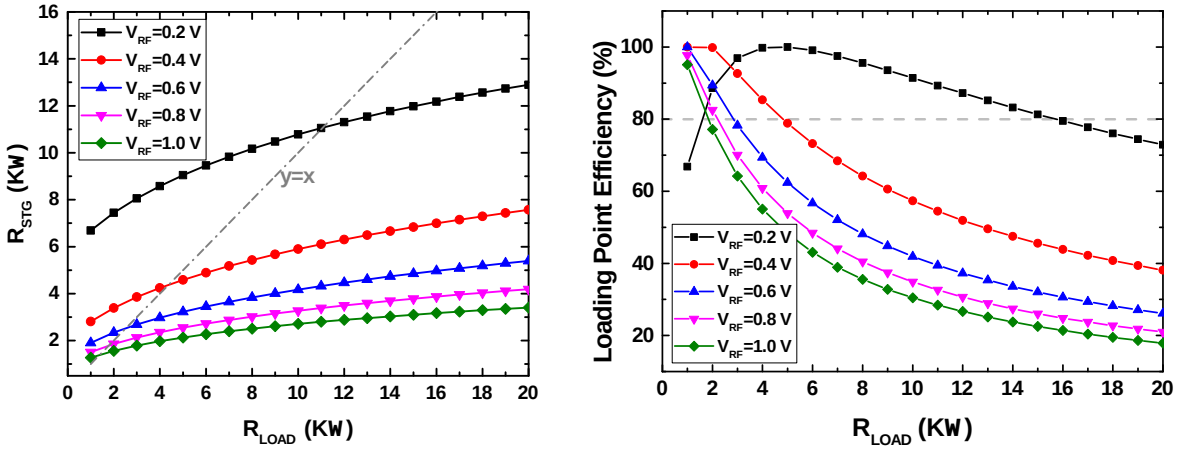

(a) (b)

Figure 3.3: (a) R_{STG} and (b) loading power extraction efficiency. ($N_{\text{EFF}} = 1$)

$$P_{\text{OUT}} = \frac{V^2{}_{\text{LOAD}}}{R_{\text{L}}} = \frac{\alpha^2 \times N_0}{R_{\text{STG}}} \times V^2{}_{\text{RECT}}. \tag{3.7}$$

$$\begin{aligned} \eta_{\text{PCE}} &= \frac{P_{\text{OUT}}}{P_{\text{RFIN}}} \\ &= (\frac{\alpha^2 \times N_0}{R_{\text{STG}}}) \times (\frac{2 \times Z_{\text{STG}}}{N_0}) \\ &= \frac{2 \times \alpha^2 \times Z_{\text{IN}_{\text{STG}}}}{R_{\text{STG}}} \end{aligned} \tag{3.8}$$

In simulation, the one-stage rectifier is used for simplicity; therefore, $Z_{\text{IN}} = Z_{\text{IN}_{\text{STG}}}$ and $R_{\text{RECT}} = R_{\text{STG}}$. $Z_{\text{IN}_{\text{STG}}}$ and R_{STG} are conceptual parameters; calculation is needed by:

$$\begin{aligned} Z_{\text{IN}} &= \frac{V^2{}_{\text{RECTrms}}}{P_{\text{RFIN}}}, \\ R_{\text{RECT}} &= R_{\text{LOAD}} \times (\frac{V_{\text{OC}} - V_{\text{LOAD}}}{V_{\text{LOAD}}}). \end{aligned} \tag{3.9}$$

From (3.8), even in the load-matching conditions, conversion efficiency still depends on α, R_{STG} and $Z_{\text{IN}_{\text{STG}}}$. As shown in Fig. 3.3a and 3.3b, the proposed load-matching point assumption can extract above 80% of the maximum output power in different input-power conditions. Here loading power extraction efficiency is defined as the percentage of the output power of different loading

resistance compared to the maximum value. In Fig. 3.3a, the simulated R_{STG} is changed from 11 KΩ to 1 KΩ when effective input power is ranged from 5 μW to 1.3 mW, which increases the challenges in the conventional MPPT operation. However, in our purposed MPPT operation, each rectifier configuration actually covers less input-power range compared to fixed stage designs. With the discrete adjustment in N_{EFF}, the changes of R_{STG} in each configuration can be minimized. For example, the simulated rectifier ($N_{\text{EFF}} = 1$) working range is only for the high power conditions. When V_{RF} is from 0.6 to 1.0 V, the variance of the R_{STG} is only from 3 KΩ to 1 KΩ with input power from 300 μW to 1.3 mW, which also achieves a higher extraction efficiency (95% at 1 KΩ) compared to the previous case.

3.2.2.2 General Loading Point Analysis

From the analysis of load-matching point above, we can find out if the analysis can be expanded to any point by changing the ratio between V_{LOAD} and V_{OC}. Therefore, a coefficient factor is needed to represent the loading effect on efficiency. We can derive the equation directly from (3.8) and (3.9) as follows:

$$\begin{aligned}\eta_{\text{PCE}} &= \frac{\frac{V^2_{\text{LOAD}}}{R_{\text{LOAD}}}}{0.5 \times \frac{V^2_{\text{RECT}}}{Z_{\text{IN}}}} = \frac{\frac{V^2_{\text{LOAD}}}{R_{\text{RECT}}}}{0.5 \times \frac{V^2_{\text{RECT}}}{Z_{\text{IN}}} \times \beta} \\ &= (\frac{2 \times \alpha^2_{\text{L}}}{\beta}) \times (\frac{Z_{\text{IN}}}{R_{\text{RECT}}}) \\ &= (\frac{2 \times \alpha^2_{\text{L}}}{\beta}) \times (\frac{Z_{\text{IN}_{\text{STG}}}}{N^2_{\text{EFF}} \times R_{\text{STG}}})\end{aligned} \tag{3.10}$$

$$\begin{aligned}\text{where } \beta &= \frac{V_{\text{LOAD}}}{V_{\text{OC}} - V_{\text{LOAD}}}, \text{loading coefficient factor;} \\ \alpha_{\text{L}} &= \frac{V_{\text{LOAD}}}{V_{\text{RECT}}}, \text{ effective voltage conversion ratio.}\end{aligned} \tag{3.11}$$

Equation (3.10) is a more general case for different loading conditions. When V_{LOAD} is half of the V_{OC} ($\beta = 1$ and $\alpha_{\text{L}} = \alpha * N_{\text{EFF}}$), it is equal to (3.8). In general case (fixed N_{EFF}), the loss contains two parts. The first part is the loading mismatch loss. The second part is the RF-DC conversion loss generated from diode imperfection and parasitic loss, which is like switching loss

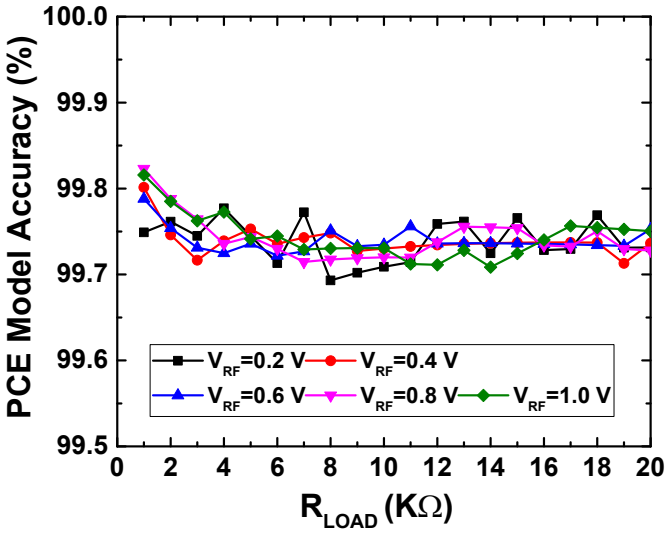

Figure 3.4: General loading efficiency model accuracy. ($N_{\text{EFF}} = 1$)

due to its high frequency operation (α_{L}) as well as the conduction loss ($Z_{\text{IN}}/R_{\text{RECT}}$). The second part is mainly determined by process parameters and proper device dimensions. And the first one can be optimized by our purposed MPPT method. Meanwhile, (3.10) indicates a smaller N_{EFF} with smaller R_{RECT} is desired for higher efficiency. Although this work does not focus on the control on the loading, a larger loading current is preferred for a smaller N_{EFF} to keep the optimal efficiency in higher input power, which means more loading blocks can be powered up internally.

Fig. 3.4 shows our proposed model (including the load-matching point efficiency) to be close to simulation results with trivial error, which means the equation is mathematical equals to η_{PCE}, but provides more design insights. Under similar loading conditions β, a higher efficiency is indicated by smaller V_{RECT} and better device parameter (Larger $Z_{\text{IN}_{\text{STG}}}/R_{\text{STG}}$ ratio). The Transistor W/L is not showing any effect in the analysis, but parasitics or leakage current will degrade the overall performance. The device parameters are supposed to be optimized to perform trade-off between $Z_{\text{IN}_{\text{STG}}}$ and R_{STG}. For example, larger W/L ratio will decrease R_{STG} by increasing the conduction current, but it will also decrease $Z_{\text{IN}_{\text{STG}}}$ by introducing more leakage and parasitics.

In our purposed model, only the rectifier efficiency η_{PCE} is considered and thus a pure sinusoidal source is used by assuming perfect matching network. However, this ideal matching network is

difficult to achieve. Therefore, the antenna impedance and the matching network with finite quality factors should be considered for further design verification. Even so, the model has shown its simplicity and effectiveness.

The preceding analysis mainly focuses on rectifier efficiency. However, the output voltage requirement is also critical; therefore, the rectifier is usually designed with a large stage number by sacrificing its efficiency. Thus, it is straightforward to make it reconfigurable to break the output voltage and efficiency trade-off, maintaining the rectifier at its highest efficiency state with different input-power conditions.

3.2.2.3 Hill-Climbing MPPT Searching

Simply, if a fixed loading resistance is connected to the rectifier, maximizing the output power means the output voltage is also maximized. From previous analysis, we can derive (3.2) and (3.3) as:

$$V_{\text{LOAD}} = \frac{N_{\text{EFF}} \times 2\alpha \times V_{\text{RECT}}}{1 + (\frac{N^2{}_{\text{EFF}}}{N_0}) \times (\frac{R_{\text{STG}}}{R_{\text{L}}})}. \tag{3.12}$$

To normalize the output voltage, we assume RF input power is constant during MPPT phase.

$$V^*{}_{\text{LOAD}} = \frac{N_{\text{EFF}}}{1 + (\frac{N^2{}_{\text{EFF}}}{N_0}) \times (\frac{R_{\text{STG}}}{R_{\text{L}}})} \tag{3.13}$$

For integer rounding, $R_{\text{STG}}/R_{\text{L}}$ is set from 10 to 0.1, the N_0 is 10 and N_{EFF} is from 1 to 10. In Fig. 3.5, the normalized V_{OUT} among different loading conditions is plotted. The output voltage of each individual configuration is ranked to find out the maximum output power directly. Each curve has only one optimal point, therefore its local optimal point is exactly the global optimal point. A digital controlled hill-climbing method is implemented to find out the optimal N_{EFF}. Every comparison is made between two successive states and the maximum state is determined by bubble sort algorithm with less FSM state numbers compared to [5, 43]. It also shows the small number ($N_{\text{EFF}} = 1, 2, 3, 4, 5$), which covers a larger optimal range than the large number

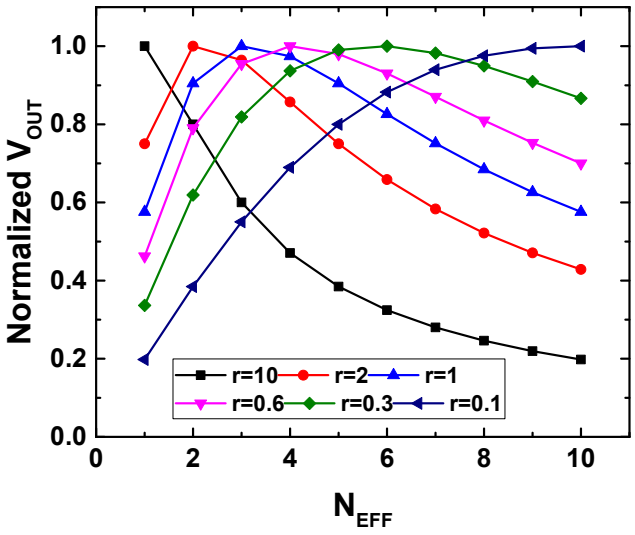

Figure 3.5: Optimal N_{EFF} distribution with different $r = R_{\text{STG}}/R_{\text{L}}$.

($N_{\text{EFF}} = 6, 7, 8, 9$), which is the reason we chose the 2,3,4,6 and 12 configuration in a 12-stage case. The analysis shows our proposed hill-climbing MPPT method can work well with constant input power. This is valid because our proposed MPPT ranking duration is minimized to five states, around 60 μs in ranking phase. And if the input power is changed during ranking, the controller can detect this error and reset to default 12-stage until the next correct ranking. Although during the MPPT mode, the ranking operation will introduce voltage ripples at the output node, its interference is minimized by short MPPT duration time and also the small duty ratio operations (60 μs in every 20 ms). For critical circuits loading, additional LDOs could be added to have better isolation. Although in this work, our purposed MPPT system is assisted by a MIMO-EH system and an external V_{dd} is used to further avoid this interference. Measurement results also verified its self-start-up and self-sustained functions because the MPPT operation is based on digital control. And the system is designed for wide V_{dd} ranges. If it is required, an additional regulated path can be added, which is explored in many recent works [31, 44, 45].

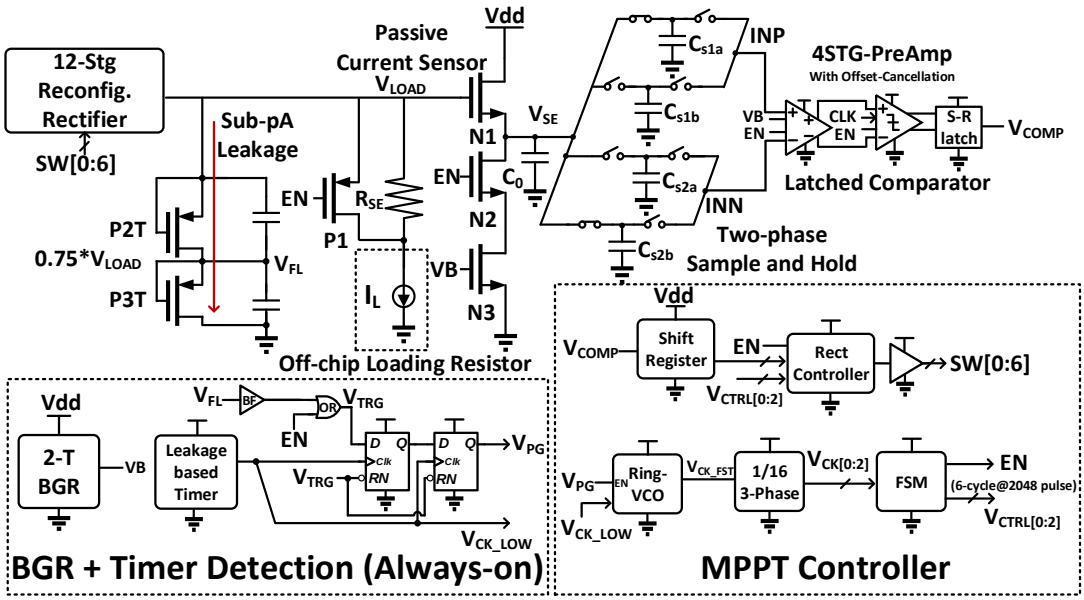

Figure 3.6: MPPT circuit block overview.

3.2.3 MPPT Circuit Block Overview

Our proposed MPPT system is based on hill-climbing method as analyzed. The loading is resistive with the on-chip capacitor 7.2 pF. The system can perform MPPT when the output voltage is larger than 0.4 V. The default stage number is set to be 12 and if there is no detected rectifier output, the whole system can sustain the detection function in the lowest $V_{\rm dd}$ as 0.5 V to achieve a low stand-by power of 20 nW. Our system has three modes: the stand-by mode with an activated always-on block, an MPPT ranking mode for searching and ranking, and an MPPT idle mode that can turn off the ranking system but keeps a fast VCO running for internal duty ratio control. The whole MPPT system shares a single one $V_{\rm dd}$ for external power source. Furthermore, the $V_{\rm dd}$ is set at 0.5, 0.75, 1.0, 1.5 and 1.8 V based on rectifier's output voltage to represent the adjustable power source from DC-DC converter. In our measurement, the $V_{\rm dd}$ is programmable through an external controller.

As shown in Fig. 3.6, the MPPT system mainly consists of two parts, 1) the always-on block, and 2) the MPPT controller. The always-on block contains a low power wake-up timer and a

voltage reference which detects the rectifiers output voltage and provides dc biasing voltage. A leakage current based voltage divider is implemented with thick-oxide PMOS P2T and P3T to generate a programmable fractional output voltage V_{FL}. Two DFFs are served as MPPT trigger block and when the voltage V_{FL} is higher than the inverter flip point ($V_{\text{dd}}/2$), the high logic signal V_{TRG} is generated through the digital buffer. In stand-by mode, once the rectifier output exceeds and maintains a certain threshold (0.4 V in measurement) until the second rising edge of the low-frequency signal VCK_LOW, the trigger signal V_{PG} will enable the MPPT controller with a fast clock generation to perform MPPT functions. To further minimize the interference introduced by the MPPT ranking mode, especially when the rectifier output voltage is closed to the flip point, a simple OR logic can be added to force the V_{TRG} to be 1 by the MPPT ranking mode flag signal EN. And when V_{FL} is below the flip point in the MPPT idle mode, which means the rectifier output voltage is dropped down because of the decreased input power. V_{TRG} is low to reset the V_{PG} to 0 immediately, and the whole system is returned to the stand-by mode until next trigger signal. Besides the control blocks, the core sensing and ranking function is achieved through the passive current sensor with an I-to-V level shifter, a sample-and-hold circuit, and a dynamic comparator with 4-stage preamplification. In MPPT ranking mode, the control signal SW[0:6] changes the rectifier configuration and V_{LOAD} value is disturbed as a direct index for maximum power point observation. The current sensor converts the output voltage of each configuration and it is sampled and stored for comparison. The comparator with shift register finds out the optimal state based on the sampled output voltage. And in the following idle mode, the controller will keep this optimal state until the next ranking operation. With a typical V_{dd} 1.0 V, the MPPT controller activated power consumption can go as high as 5 μW during the MPPT ranking mode. Therefore, an internal duty ratio controller will enable a 6-cycle MPPT ranking function after every 2048 clock cycles to average the power consumption down to 600 nW. To further minimize power consumption, the low power $V_{\text{CK\_LOW}}$ signal can be leveraged as an enable signal for external duty control.

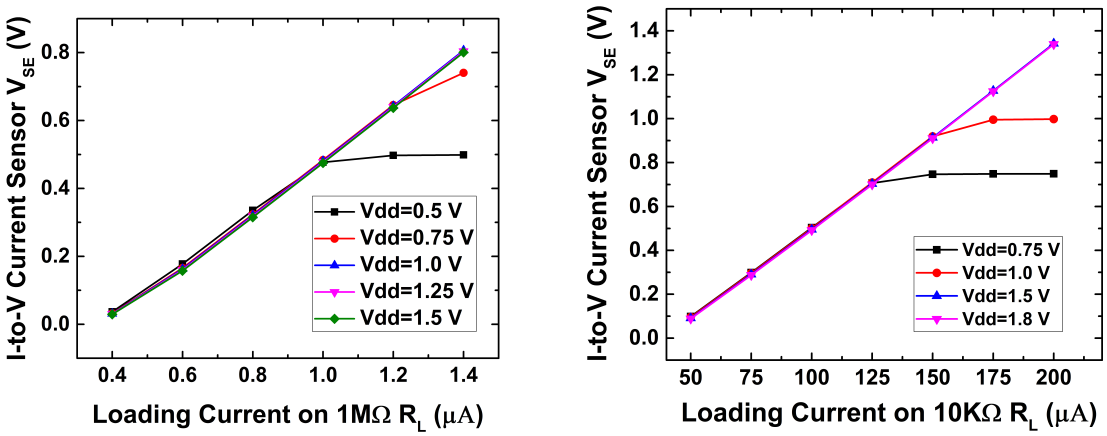

Figure 3.7: Current sensor steady output for low and high power conditions.

3.2.3.1 Passive Current Sensor Design

The current sensor simulation is shown in Fig. 3.7. A passive 250-Ω resistance is used by introducing less than 3% power overhead because the sensing current is typical at the μA level, and the loading resistance is larger than 10 KΩ. Additionally, a PMOS switch is turned on to bypass the sensor in the idle phase. The resistance value is chosen to ensure large enough I-to-V gain and finely adjust the output voltage. This resistance value is not very restricted for sensing because a nA-level biased source follower is also added to adjust the output voltage. In the normal operation range (V_{dd} from 0.75 to 1.8 V), the simulated average I-to-V gain is 0.77 V/μA with a coefficient of variation 8% under the 1-MΩ loading conditions. In the high power conditions, the simulated gain is 0.80 V/100μA with the loading of 10-KΩ. When the system is configured as the self-sustained mode, the V_{dd} is connected to V_{LOAD} directly and the N1 in Fig. 3.6 is in diode connection. The current sensor can still work in this configuration as a level shifter.

3.2.3.2 Two-phase Sample and Hold Circuit

The two-phase sample and hold circuit details are shown in Fig. 3.8. $V_{\text{CK}}[1]$ and $V_{\text{CK}}[2]$ are two nonoverlapped control signals. In each sample operation, two 200-fF capacitors are connected to V_{SE} to store the output voltage of the current sensor. And then one is used to compare with the previous sampled value from the previous stage and the other one is held and compared with

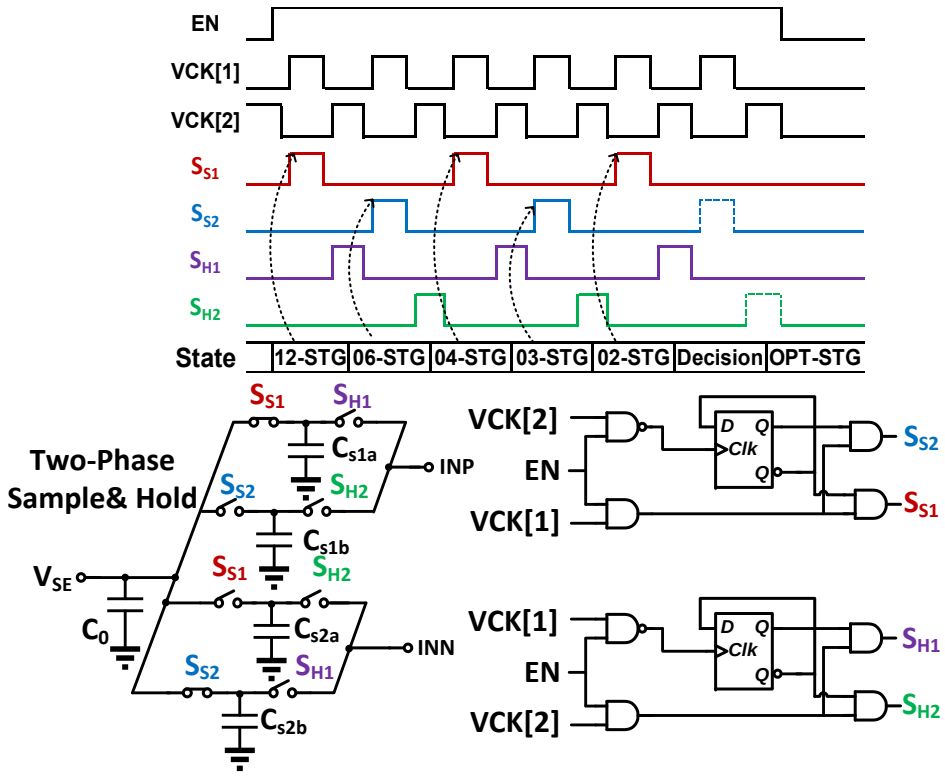

Figure 3.8: Two-phase sample and hold circuit with its control scheme.

the next sampled value in the next operation. Interleave two-phase operations are implemented because each middle state is required to compared twice with its adjacent states.

3.2.3.3 Low Offset Comparator Design

Fig. 3.9 shows the comparator architecture and control signals in the MPPT phase. $V_{\mathrm{CK}}[0{:}2]$ is generated from a 2-MHz VCO with $1/16$ frequency divider. $V_{\mathrm{CK}}[1]$ is a delayed version of $V_{\mathrm{CK}}[0]$. The FSM generates a rectifier-state sweeping and performs MPPT ranking by detecting the voltage difference between two successive states to find out the maximum state. If the current stage is larger than the previous stage, the temporary optimal stage is current stage until next optimal stage appears. For example, in Fig. 3.9, at the second S_{eval} pulse, current 6-stage is compared to previous 12-stage and the comparison results is low, indicating that the current stage output voltage is less than that in the previous stage. And with previous analysis, the optimal point is located at the previous stage 12. When the rectifier stage number is changed, a reset phase

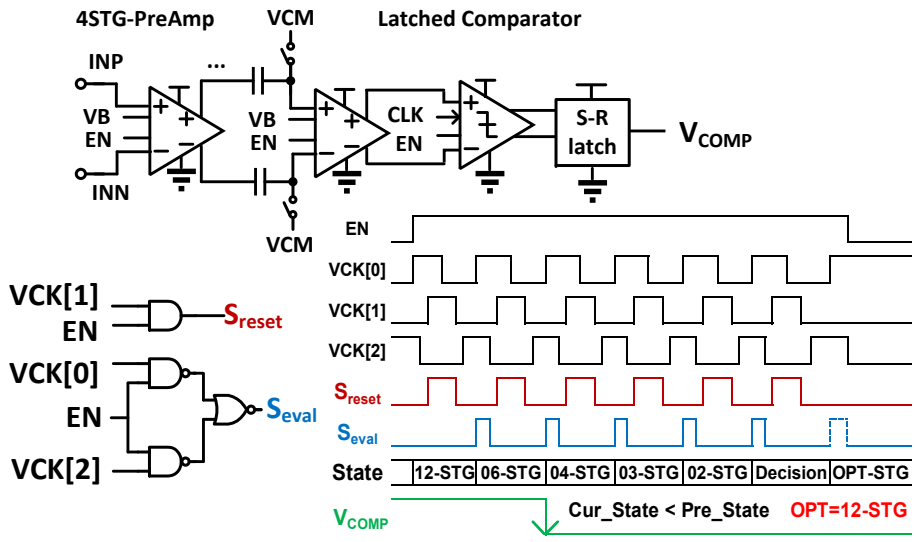

Figure 3.9: Comparator and MPPT control scheme.

between two successive comparisons is triggered for two main reasons: One is waiting for rectifier output node to be settled, and the other is resetting the comparator inner node to store the systematic offset value. Monte-Carlo simulation results show the offset voltage mean value as 68.7 μV with standard variation of 120 μV under 1000 samples. The overall system requirement is to detect 1 μA loading current difference and the minimum resolution is simulated as 8.0 mV including current sensor I-to-V gain at the minimum loading resistance 10 KΩ. Offset cancellation technique is used to decrease the offset by adding minor control overhead since multi-stage amplifiers are used and reset phase is required to wait until the rectifier output is settled. Pre-amps are used to ensure high gain and high-speed operation and decrease the bidirectional kick-back noise. And 4-stage amplifiers are used to provide a high enough gain in wide-range V_{dd} operations. The simulated minimum gain in the typical corner is 14 dB at the minimum V_{dd} 0.75 V in the MPPT ranking mode. The MPPT power overhead is minimized as 14% by duty ratio control and in the idle phase, all the MPPT ranking blocks are turned off by switches.

3.2.3.4 Always-on Block Design

The always-on block power consumption is critical to system efficiency. For wake-up timer design, the basic idea is from a pico-Walt timer based on [46] where gate leakage is used for low voltage operation. However, this gate leakage is not well controlled in wide V_{dd} operation. Therefore, two diode-connected transistor are used to control the charge/discharge current. The simulation results show the wake-up timer frequency is 16 Hz with 0.3 nW at V_{dd} 0.5 V and 170 Hz with 3.7 μW at V_{dd} 1.5 V. The 2-T architecture [47] is served for reference biasing. The simulation shows its output is 474 mV at V_{dd} 0.5 V with a 50 mV/V line regulation and a power consumption from 5.4 nW to 80 nW.

3.2.4 Antenna Design and Matching Design

To achieve high efficiency and good sensitivity, antenna gain and efficiency are also very important factors. Higher antenna gain can increase the received power from a given direction, and high efficiency increases the received power. Therefore a 915-MHz patch type antenna with L-probe feed is proposed to achieve high gain and high efficiency [3]. The antenna design is shown in plan and elevation views in Fig. 3.10. The substrate is 1.6 mm thick Rogers 3003 circuit board. The thick air substrate between the patch and ground and the L-probe feed are used to improve the bandwidth and radiation efficiency. The antenna radiation patterns, which were measured by the SATIMO StarLab system, are also shown in Fig. 3.10. The realized gain is 7.5 dBi at 915-MHz with 93% efficiency.

The 50-ohm matching method is used for discrete low-pass L-C (5 nH and 10 pF) matching network design. The rectifier and antenna performance can be well characterized individually, and the whole system is more flexible. If a high converted efficiency is desired, our purposed customized antenna is used; otherwise, other types of antenna can replace for area, low-cost or other considerations.

Fig. 3.11 shows the measured rectifier and antenna S_{11} parameter of less than -20 dB at 915-MHz, which shows very good impedance matching between the antenna and rectifier. The

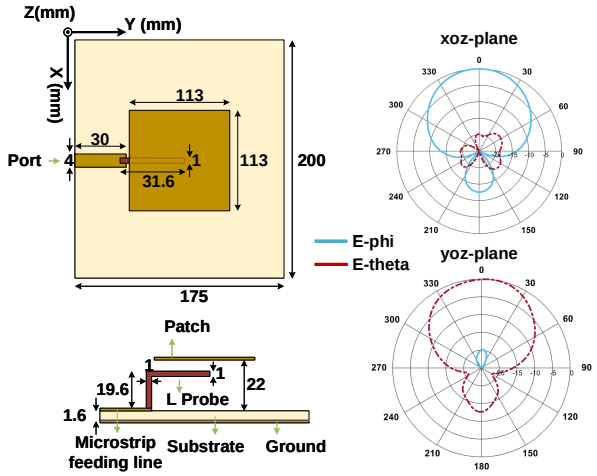

Figure 3.10: Dimensions of the patch antenna and its radiation pattern.

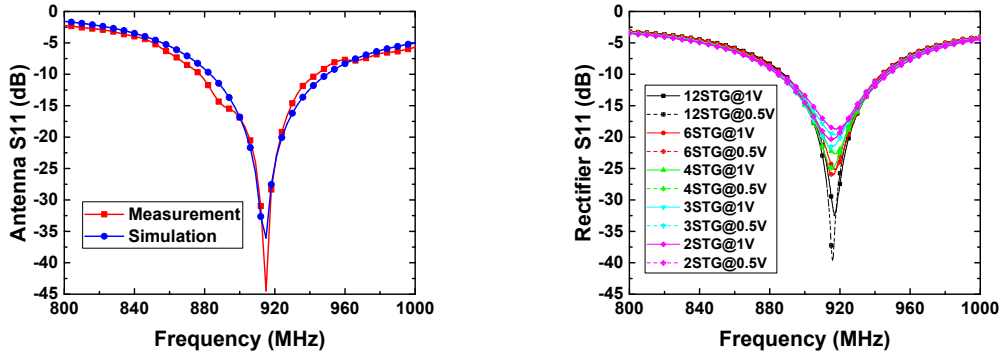

(a) (b)

Figure 3.11: S_{11} of (a) antenna and (b) reconfigurable rectifier with matching.

results in Fig. 3.11b also show how the optimal matching point is kept with target frequency under different configurations with a fixed matching network. In a conventional fixed stage rectifier design, it is reported that with higher input power, the S_{11} optimal point will be shifted from its original value because of the higher V_{OUT}; therefore, an input matching calibration is required [5]. With previous analysis, the S_{11} shift in higher power can be regarded as evidence that the internal output resistance R_{RECT} changes with the input power, and causes the impedance mismatch between R_{RECT} and R_{L}. Consequently, the absorbed power is less than the ideal case because

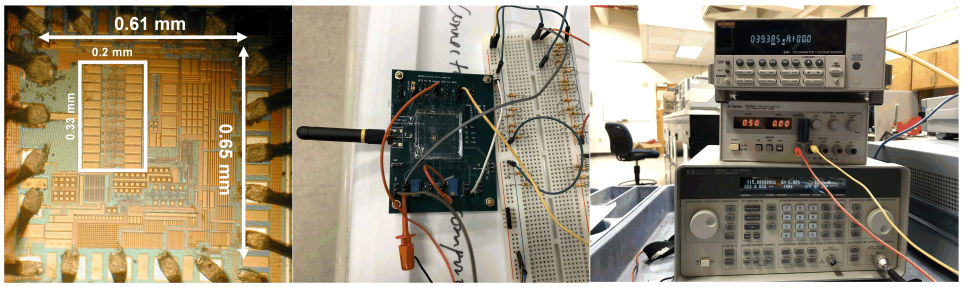

Figure 3.12: Die bonding-on-board micro-photo and test-bench.

the delivered output power is less, and all the remained power will be reflected and thus the S_{11} decreases[33]. Input matching calibration can help to adjust S_{11} back to the optimal point but it would require a high resolution sweeping and detection. As mentioned in the previous analysis, the reconfigurable structure has a negligible effect on the Z_{IN} since all the stage cells are connected for rectification. Moreover, changing R_{RECT} by N_{EFF} reconfiguration can not only limit the changes in the rectifier V_{OUT} for better S_{11} matching but also adjust N_{EFF} to get higher efficiency. Therefore, it is more efficient to sustain the rectifier optimal state in the wide input-power range even with a fixed matching network, which is supported by the S_{11} measurement directly.

3.3 Measurement Results

Fig. 3.12 shows the die micrograph fabricated in Global-Foundries CMOS 180-nm. The reconfigurable rectifier is 0.066 mm^2, and total area is 0.4 mm^2. The die is attached and bonded to the 4-layer FR-4 PCB. The PCB board is also shown connected to a commercial antenna for field testing. Major measurement equipment is including 8648C RF signal generator, 6487 pico-ammeter and the N5230A network analyzer. The pico-ammeter is used to measure nA-current and the minimum stand-by current is 39.4 nA with V_{dd} 0.5 V. The V_{dd} is externally connected to a dc power supply.

Fig. 3.13a shows the 12-stage configuration rectifier output changes with input power under different V_{dd} values. When the output voltage is smaller than V_{dd}, the gate voltage of the reconfiguration switches is high enough to suppress the parasitic R_{ON}. Therefore, the output voltage difference is $< 10\%$. When the output voltage is close and even higher than the V_{dd}, the PMOS

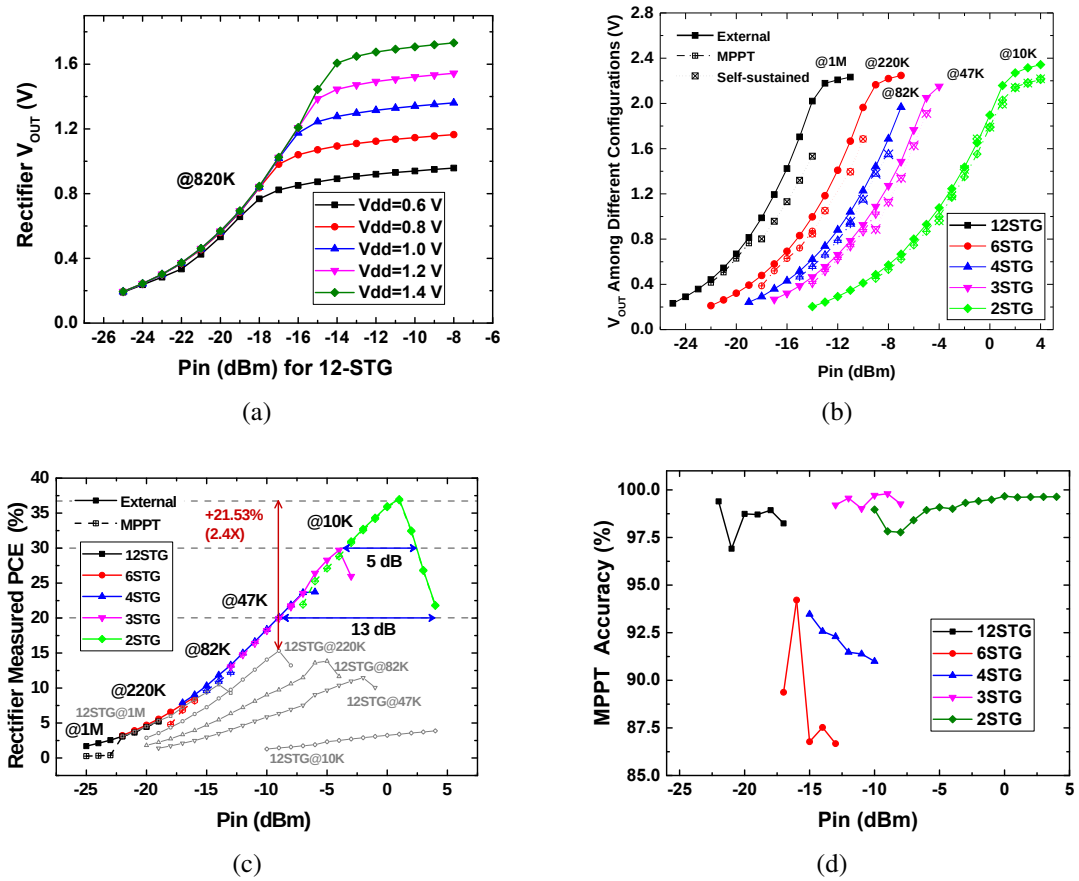

Figure 3.13: (a) Rectifier V_{OUT} with different V_{dd}, (b) V_{OUT} with all configurations, (c) rectifier (with matching network) PCE and (d) MPPT accuracy.

in bypass switches which connects the internal node to the final output cannot be turned off in this case because the internal node voltage is also close to the gate voltage. Therefore, forward biased diodes are generated and thus the output voltage growth is suppressed. This effect can be used as an inherited coarse regulation and voltage protection. And rectifier output voltage with different configurations is also plotted in Fig. 3.13b. In the MPPT mode, output voltage ranging from 0.4 to 0.8 V is measured except for the last configuration, which extends into the high power working range. Results show our proposed MPPT function can work from -22 to 4 dBm when V_{OUT} is larger than 0.4 V.

Fig. 3.13c shows the complete rectifier PCE under external control and internal MPPT con-

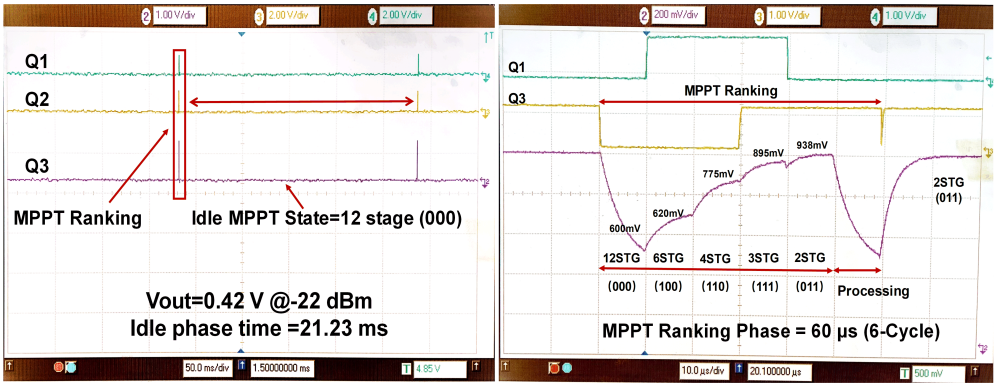

Figure 3.14: MPPT transient waveform in the MPPT idle mode and in the ranking mode. ($V_{\mathrm{dd}} = 1.0$ V)

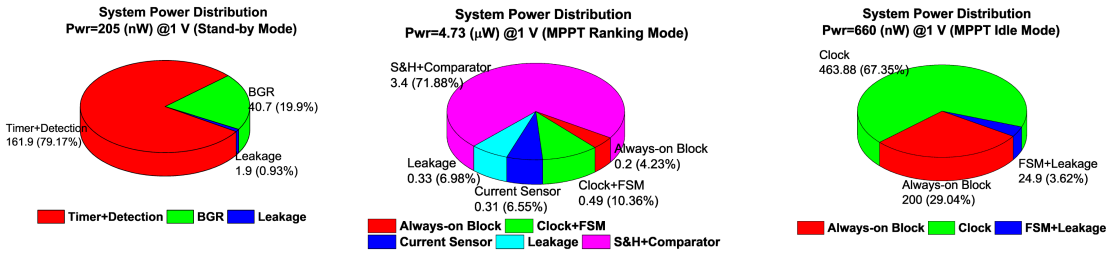

Figure 3.15: MPPT system power distribution in simulation. ($V_{\mathrm{dd}} = 1.0$ V)

trol. The PCE here is the power conversion efficiency of the rectifier with the matching network. To better show the improvement, the efficiency curves of the fixed 12-STG rectifier (under external control) with similar loading are also plotted. Meanwhile, it is equivalent to the conventional MPPT method by adjusting the optimal loading on a fixed stage rectifier optimized for the minimum sensitivity. Compared to the fixed stage rectifier, our purposed reconfigurable rectifier can break the trade-off between its peak efficiency and its sensitivity, and maintain its optimal state in wide input-power operations. The peak efficiency in the 12-STG configuration is only 15.3% and the overall efficiency is less than 20% even in the extremely high power conditions. However, in our purposed reconfigurable structure, the peak efficiency is 36.9% ($2.4\times$) with a 13 dB operation range for PCE $> 20\%$, which demonstrates the improvement on rectifier efficiency compared to

conventional MPPT operations.

The overall efficiency difference is shown in Fig. 3.13d. The MPPT accuracy is measured as larger than 87%. The MPPT accuracy is defined as the percentage of measured output power in the MPPT mode where programmable V_{dd} is used compared to the power measured in external tuning at fixed V_{dd} 1.8 V. The minimum MPPT accuracy appears in 6-STG and 4-STG mainly because their adjacent state performance is close; therefore, the performance is more sensitive to the smaller V_{dd}. The internal 7.2-pF capacitor can suppress the ripple within 10 mV with the help of the recombined stage-capacitor. Moreover, a 50% loading-resistance variance from the optimal loading in each configuration introduces a small absolute PCE difference less than 0.6%. With other different loading, the MPPT system can find the optimal state as long as V_{OUT} is larger than 0.4 V.

Fig. 3.14 shows two transient waveforms for MPPT functions. The left one shows the MPPT as triggered with minimum detectable voltage. The pulse from the digital signal represents the MPPT searching and the optimal state is kept until the next MPPT ranking mode. The internal duty ratio control is activated to reduce the power overhead. The waveform on the right shows a detailed plot of the MPPT ranking mode in high input-power conditions. The MPPT ranking takes 5 cycles to rank and determine the optimal stage in the 6^{th} cycle. The measured MPPT duration time is 60 μs for every 20 ms with 100-KHz V_{CK} signal at V_{dd} 1 V.

To better illustrate the power dissipation budget, post-layout simulation at 1 V V_{dd} is shown in Fig. 3.15. Compared to simulation results, the measured stand-by mode power is from 19.5 nW at 0.5 V to 5 μW at 1.8 V. Furthermore, the measured MPPT power consumption with internal duty ratio control is from 19.5 nW to 6.4 μW. In the minimum power case, stand-by power is same as MPPT power because in the minimum V_{dd} 0.5 V, one of the digital standard cells cannot disable the VCO therefore it stays in the MPPT idle mode. This will not affect system operation, but it will increase the minimum detectable power consumption from the 6 nW in simulation.

In Fig. 3.16, the maximum MPPT power efficiency under different configurations is plotted. The MPPT power efficiency is calculated by the effective harvested power over the measured har-

Table 3.1: Literature review and comparison of the end-to-end RF EH system.

	JSSC'14 [43]	JSSC'11 [48]	JSSC'17 [31]	JSSC'14 [5]	**This Work**
Freq.(MHz)	905	915	915	868	915
Tech. (nm)	65	90	180	90	180
Die Area / Rect. Area (mm^2)	2 / 0.080♮	1.35 / 0.190	5.3 / 0.275♮	0.8♮/ 0.029	0.4 / 0.066
Stage Number	12	17	1-2-4-8	5	2-3-4-6-12
$V_{\text{OUT}}(V)$	0.5 - 0.9	0 - 6.0	> 1.0	0.5 - 2.2	0.4 - 2.2 0.8 - 2.2 (Self-sustained)
System Requirement	Gate Biasing Switches+ LDO	Deep N-Well Vth-Compensated	Pre-defined Threshold + Ext. 100-μF	Real Time Processor+ Tunable MN.	External V_{dd} 0.5 - 1.8 + Loading Control
Antenna and Eff.	Loop Antenna	No	No	Loop (84.7%)	Patch (93%)
Distance 1V@1-Mohm	0.9 m @20 dBm Tx	NA	NA	27 m (chamber) @32.5 dBm Tx	1.78 m @10 dBm Tx
Sensitivity 1V@1-Mohm	4.0% @−16 dBm	5.6% @−17.5 dBm	3.0% @−14.8 dBm	17.8%* @−22 dBm	6.0%* @−17.8 dBm
MPPT Range	−20 to −14 dBm	NA	−15 to 0 dBm	−27 to −10 dBm	**−22 to 4 dBm** −18 to 4 dBm (Self-sustained)
MPPT Power Efficiency	Not reported		82% - 90% 90%@−5 dBm	Not reported	**72% - 99.8%** >90%@−19 dBm 58% - 99.8% (Self-sustained)
MPPT Accuracy	Not reported		Not reported	Not reported	**> 87%**
MPPT Duration	3.2 ms		Always-on	0.5 s	60 μs
Peak PCE	5.2% @−14 dBm	16% @−15.8 dBm	25% @0 dBm	40%* @−17 dBm	34.4%* @1.3 dBm
Peak PCE Enhancement	+2.5% (1.6×)◇	NA	+11% (1.8×)†	+6.4% (1.28×)◇	**+21.5% (2.4×)**†
High PCE Range	0 dB	0 dB	10 dB (> 20%)	10 dB (> 20%)	**13 dB (> 20%)**
Pwr Density Capacity‡ MIN.-MAX.($\mu W/mm^2$)	13 - 26 (2×)	5 - 22 (4×)	4 - 909 (227×)	34 - 275 (8×)	**15 - 7031 (469×)**
Minimum Power	500 nW@0.5 V	NA (Passive)	66 nW@1 V	Not reported	20 nW@0.5 V

♮ Estimated from layout figure and reported data
* End-to-end power conversion efficiency including antenna efficiency
◇ Calculated based on the maximum PCE difference w/ and w/o efficiency enhancement techniques
† Calculated based on the overall peak PCE compared to the peak PCE in the configuration for the lowest power range
‡ Calculated based on the rectifier static output power at sensitivity (MIN.) and peak efficiency point (MAX.), only the rectifier area is considered

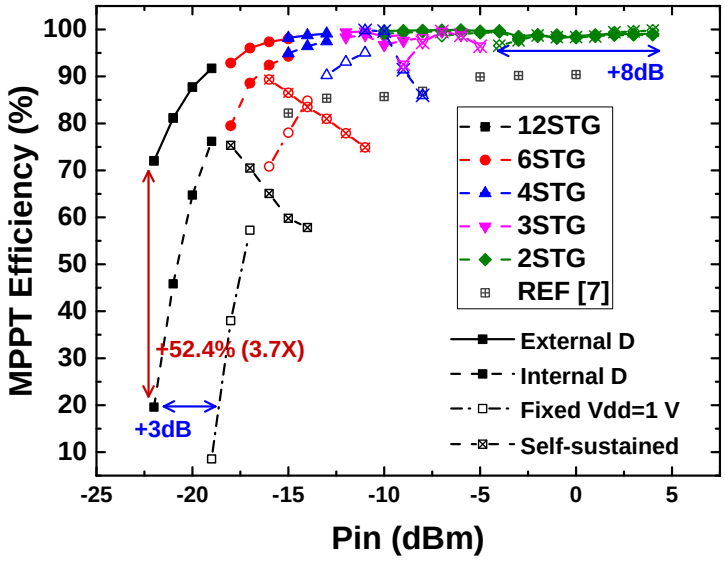

Figure 3.16: Measured MPPT power efficiency and comparison.

vested power at the loading. The effective harvested power is the difference between the harvested power and the consumed power because the consumed power performs as an additional power loss compared to passive design. To further improve MPPT power efficiency in the low power range, an additional external duty ratio control mode is used for comparison. A 1/32 counter triggered by external $V_{\text{CK\_LOW}}$ was used, and the 0.2% power overhead is almost undetectable in simulation. The comparison shows that an additional 3% duty ratio control can improve MPPT power efficiency a maximum of $3.7\times$ by increasing the refreshing cycle, typically every 0.3 s from 20 ms originally. Notably, the scalable V_{dd} extends the overall MPPT range by 11 dB compared to fixed V_{dd} conditions, which decreases the power overhead in the lower input-power range and ensures room for output voltage in the higher input-power range. In the higher input-power range (> -10 dBm), the power efficiency improvement is less ($< 3\%$) because the harvested power is much greater than the consumed power. Compared to the MPPT power efficiency in [31], our system can achieve a higher efficiency from 72% to 99.8%, and also a larger operation range from -22 to 4 dBm.

Since this scaling V_{dd} might not exist in a power constraint system, the MPPT power efficiency

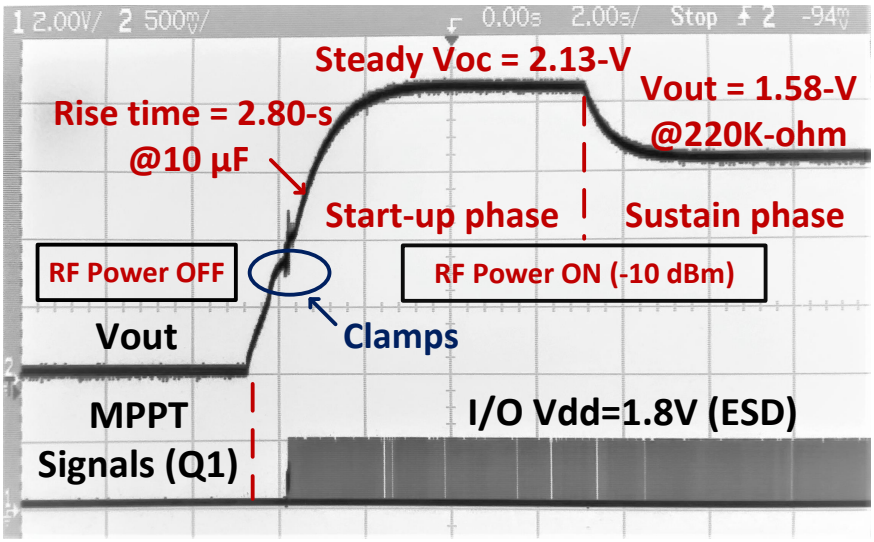

Figure 3.17: Self-start-up and self-sustained operation with capacitor 10 μF.

under $V_{\text{dd}} = 1.0$ V and self-sustained mode with internal duty control is also added for comparison in Fig. 3.16. For self-sustained mode, the minimum V_{OUT} is severer as 0.8 V because of the rectifier self-start-up issues. The logic buffer for configuration under undefined internal V_{dd} requires a higher supply to generate low-level logic signals and thus the leakage current to ground is generated through the NMOS switches. Therefore, its operating range is decreased as -18 dBm to 4 dBm with power efficiency from 58% to 99.8%. And the efficiency is dropped down from the optimal point because of its relatively high voltage operations ($V_{\text{OUT}} > 0.8$ V). That efficiency tackles under high voltage, especially in the low input-power range, also appears in other modes. And they are curtailed by the loading control (V_{OUT} from 0.4 to 0.8 V except for the last configuration). The self-sustained function is provided but could be improved to minimize the start-up voltage and power efficiency because the system operation is optimized for external mode with V_{dd} below 1 V. Even though, the RF-EH system can help the MIMO-EH system startup and then it can be configured back to the external V_{dd} mode with better performance.

Fig. 3.17 shows a typical system start-up case without external controls. The output is connected to a 10 μF capacitor for energy storage, and this output is also served as the V_{dd} of the whole internal MPPT system. An additional voltage source is used only to power up the I/O buffer

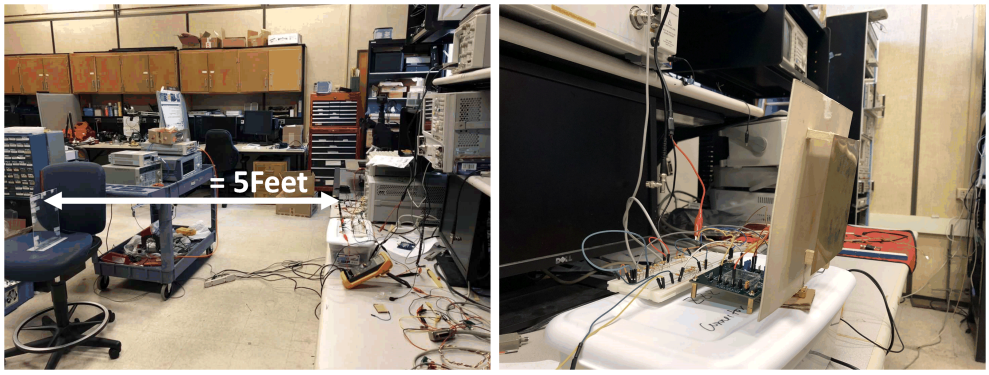

Figure 3.18: RF-EH system field testing bench.

for testing. It shows our proposed system can work with different usage scenarios, to charge up an external capacitor for energy storage when there is no available power for the whole system. The self-sustained V_{OUT} of fixed configuration 12-STG is 0.7 V at same power condition because of the similar mechanism in V_{dd} protection. The PMOS diode connection clamps the V_{OUT} in a metastable state. However, the MPPT ranking operation disturbs the switches and breaks the clamps to keep the output voltage increasing. It finally maintains at the highest V_{OUT} at 12-STG. And then a 220 KΩ loading is connected to the output, and the MPPT operation ensures the optimal stage 6-STG in the self-sustained mode. This big capacitor buffer can suppress the ripples below 10 mV during the ranking mode but it also raises up the offset requirement (1 mV difference in the adjacent state) and our MPPT system can still function properly under the help of offset cancellation techniques. Although the triggered MPPT operation guarantees the start-up function in the rising edge. Similar V_{OUT} is achieved with a shorter rise time 1.20 s in the fixed 12-STG with external V_{dd} as a passive reference, which shows a compromise between the start-up response ($0.43\times$) and the wide input-power operations.

Fig. 3.18 shows the system demonstration for indoor applications. At the Tx side, A dipole antenna with 0.5 dBi gain is used. For comparison, a commercial -1.3 dBi monopole antenna is used at Rx and it can provide 1 V for a 1-MΩ loading with 14 dBm Tx power from 1.52 meters away. Then the co-designed antenna is replaced to get same power with 7 dBm Tx power in the same position, which is 7 dB less than measured in the original case. For a moderate 10 dBm Tx

test case, 1.78-meter distance is measured with similar harvested power, showing that our system can harvest power from the potential energy source for indoor wireless sensor applications.

Table 3.1 compares our results with other works. Compared to fixed-stage designs [48], our design can limit the output voltage from 0.4 to 2.2 V. Our sensitivity and peak efficiency are better because of the native device which is commonly provided. Compared to the designs in [31, 43], our work achieves a better performance, including sensitivity, peak efficiency, high efficiency range, highest reported MPPT power efficiency and the largest MPPT range. Efficiency in [43] is relatively low because the gate biasing switches introduce large parasitic effects. Work in [31] uses an on-chip matching network, and its reconfigurable structure is not optimized for high power conditions. Compared to work in [5], our sensitivity and peak efficiency performance is comparable but less because the advanced process can ensure smaller parasitic loss and better channel current control in high frequency. However, it relies on a 7-bit capacitor array sweeping through an external controller, which will introduce a larger power overhead for control and detection. Compared to the fixed configuration, our purposed architecture can improve the peak efficiency by $2.4\times$, which shows the maximum enhancement compared to other works in the table. And the high PCE ($> 20\%$) range is also extended to 13 dB from 0 dB in origin. Thanks to duty ratio control and scaling V_{dd}, our work can achieve the lowest standby power as 20 nW at 0.5 V. The overall MPPT power efficiency is over 72% in the worst case and higher than 90% when the input power is larger than -19 dBm with MPPT accuracy over 87%. In terms of the rectifier output-power density capacity, our proposed design can achieve similar or better value at the minimum sensitivity point and can extend its maximum value in the high power ranges by adjustment in N_{EFF} and recombination of the stage capacitor, which also shows the maximum output-power density with the largest dynamic range in the comparison table. Overall, our proposed MPPT system can optimize the reconfigurable rectifier for wide range operations from -22 to -4 dBm and maintain high efficiency to extract the available RF power. A peak end-to-end efficiency is measured as 34.4% including antenna efficiency with a peak MPPT power efficiency of 99.8%.

3.4 Conclusion

In this work, a wide input-power range RF energy harvesting system with self-start-up and self-sustained functions is designed with an optimized reconfigurable 12-stage rectifier. The system can provide MPPT functions for the target range when output voltage is larger than 0.4 V. An analysis model is provided with a high accuracy and design intuition. To maximize overall system efficiency, a high efficiency patch antenna was co-designed. Measurement in field testing showed that our system can achieve minimum power sensitivity in 1.78 meters from a 10-dBm power source. Compared to other works, our end-to-end design achieves comparable and better sensitivity at -17.8 dBm and peak efficiency 34.4%. The high efficiency range (PCE > 20%) is 13 dB with an effective MPPT power efficiency above 72%, and a peak value of 99.8%.

4. AN ULTRA-LOW-POWER SC CONVERTER WITH OUTPUT BOOTSTRAPPING AND REVERSE LEAKAGE REDUCTION FUNCTION FOR RF EH [1]

4.1 Introduction

One challenge of RF energy harvesting is the limited RF-to-DC efficiency, especially for the low input RF power range. To improve the efficiency in the low input power range, low threshold devices or threshold compensated topologies are commonly adopted to reduce the forward voltage loss while sacrificing the diode reverse current clamping abilities [49, 50]. To further improve its efficiency, the input RF waveform optimized for wireless power transfer has been studied recently [51, 52]. It is found that the amplitude-modulated waveform can improve the rectifier efficiency when the waveform is near its peak value. However, when the waveform stays in the valley region, the undesired diode reverse leakage will discharge the energy-storage capacitor loading, which causes the output voltage drop and degrades the overall performance. A larger capacitor would be required to limit this undesired voltage drop. Whats worse, if the input RF power is weak or even zero periodically, the output voltage of the rectifier will decrease abruptly due to this leakage current.

To solve this issue, in the conventional RF-EH based battery charging systems as shown in Fig. 4.1a, a switch controlled by the power management unit (PMU) is inserted to reduce the reverse leakage current. However, the power consumption of PMU is high as micro-watts [53, 54] and it needs to monitor the direction of current flow continuously. In this paper, a novel switched-capacitor (SC) converter is proposed at the output of the rectifier as shown in Fig. 4.1b. This converter can boost up the output voltage of the RF-EH system for better energy storage. More importantly, it blocks the leakage current from the main battery to the rectifier. To keep the control power overhead to a minimum level, an asynchronous control scheme is proposed to replace power-

[1] Part of this chapter is reprinted with copyright permission, from Z. Zeng, S. Shen, B. Wang, J. J. Estrada-López, R. Murch and E. Sánchez-Sinencio, "An Ultra-low-power Power Management Circuit with Output Bootstrapping and Reverse Leakage Reduction Function for RF Energy Harvesting," 2020 IEEE/MTT-S International Microwave Symposium (IMS), Los Angeles, CA, USA, 2020, pp. 1059-1062.

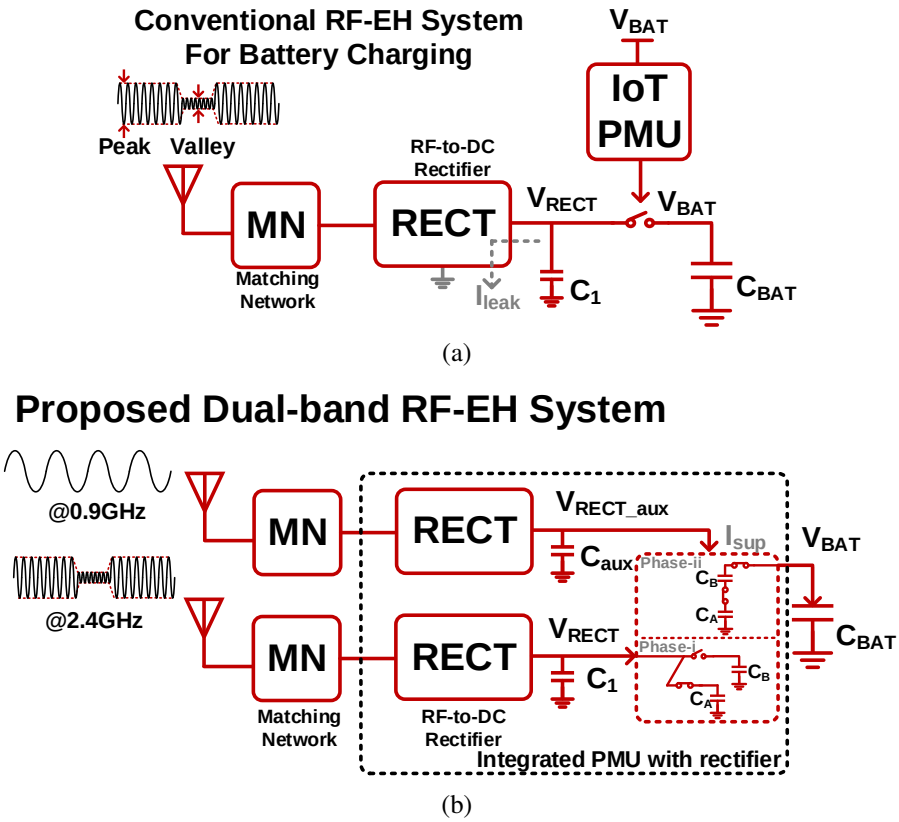

Figure 4.1: (a) Conventional RF-EH PMU and (b) our proposed RF-EH PMU.

hungry clocking elements. As a result, the voltage conversion efficiency is significantly improved in such low-frequency operations with minimized switching loss and minimized consumed power. When the RF power is weak or zero, the PMU automatically stays in the idle mode until the RF power is high enough.

Our proposed RF-EH system operates at GSM-900 (900 MHz) and WLAN (2.4 GHz) bands. As shown in Fig. 4.1b, a dual-port structure is adopted so that one antenna port harvests RF energy from WLAN and the other antenna port harvests RF energy from GSM-900. Particularly, the RF waveform from WLAN is highly related to user behaviors with high PAPR, which will cause current leakage and degraded performance. Therefore, we propose a novel PMU architecture with output voltage bootstrapping and reverse leakage current reduction function to efficiently harvest the WLAN RF energy.

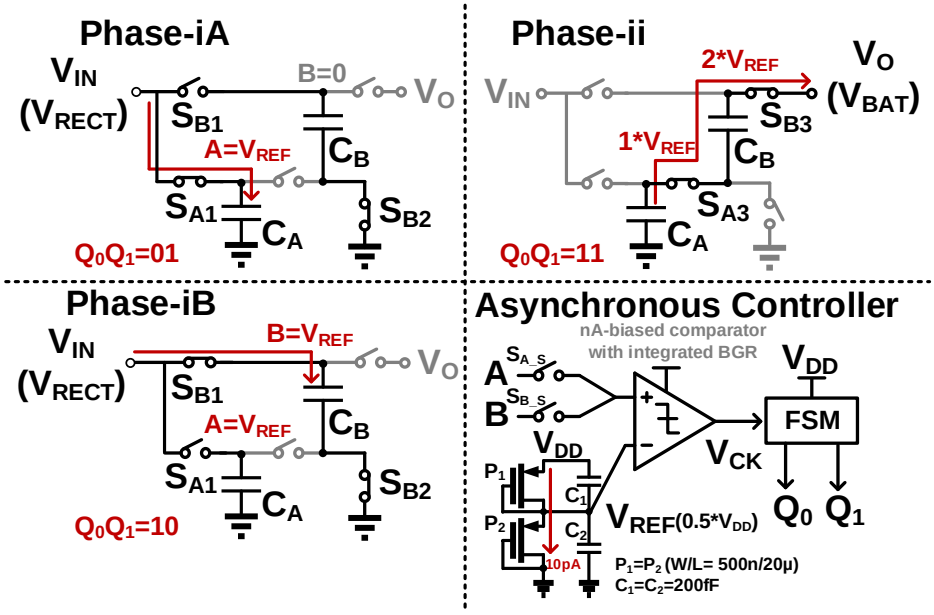

Figure 4.2: Asynchronous-controlled 1:2 parallel-series SC converter principles.

This paper is organized as follows: Section 3.2 discusses the design details of the proposed power management system. Section 3.3 shows the measurement results and literature comparison. Section 3.4 concludes this work.

4.2 Design of the Proposed RF-EH System

The RF-EH system includes rectifiers with an off-chip matching network and an SC converter PMU. The rectifier topology is a two-stage Dickson rectifier employing native transistors [38]. The typical threshold voltage is simulated as 125 mV. As shown in Fig. 4.1b, the PMU supply V_{DD} is powered up by another rectifier optimized for the GSM-900 band. The PMU input V_{IN} is connected to the output of the 2.4 GHz rectifier. The PMU output V_O is connected to a capacitor loading that serves as a battery to store the harvested energy. The PMU can also be self-powered up in a single-port system with single-band operations. In this case, the PMU is configured as a 1:1 SC converter by simply connecting the V_{DD} to the V_O directly in the self-sustain mode. Nevertheless, the dual-band operations can make full advantage of the ambient RF power from different bands, and the dual-port structure can achieve optimization for each band separately. The

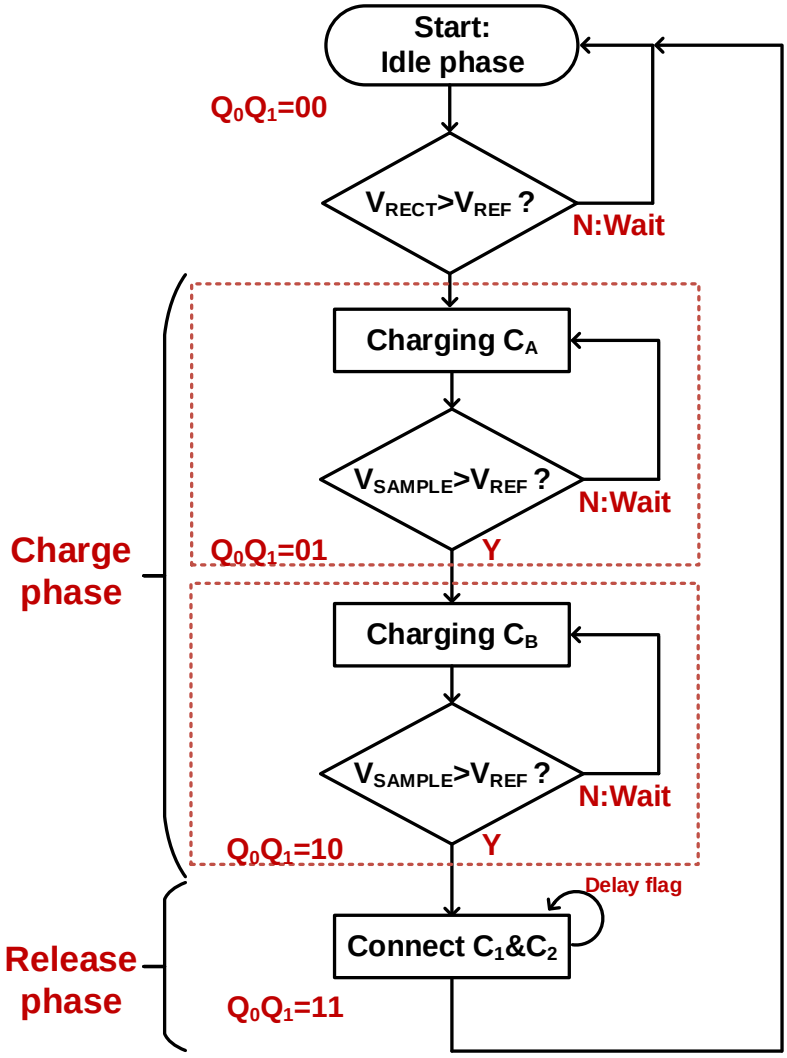

Figure 4.3: Event-triggered PMU FSM diagram.

PMU is powered up by the harvested GSM-900 power through the other port. And because this PMU only consumes power in nano-watts, this harvested power from the GSM-900 band can be used to power up the IoT sensor loading simultaneously.

4.2.1 Asynchronous 1:2 Parallel-Series SC Converter

Fig. 4.2 shows the working principles of the 1:2 parallel-series SC converter PMU. In conventional designs, the switches are driven by the clock signals which requires dynamic power in the level of μW. To accommodate the RF-EH scenarios, a novel asynchronous SC converter is

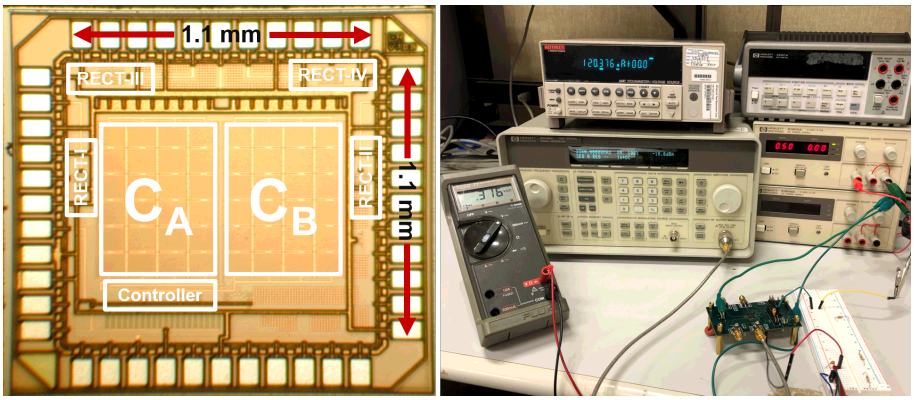

Figure 4.4: Die micrograph and measurement test-bench photograph.

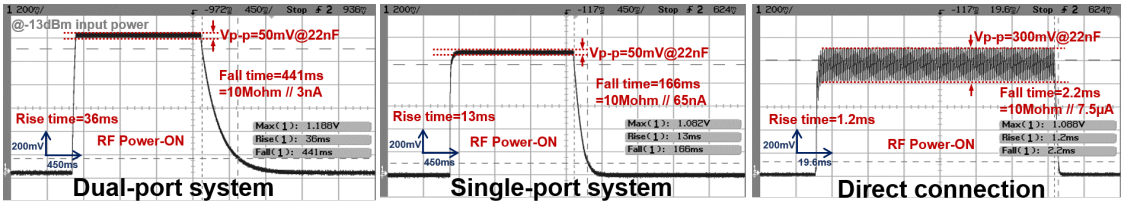

Figure 4.5: Cold start-up results under AM modulated power. (with a 10-MΩ probe)

proposed. An nA-biased (through an ultra-low-power band-gap reference (BGR) [55]) comparator continuously monitors the voltage of the capacitor bank. Its output V_{CK} invokes the internal finite-state-machine (FSM). Firstly, in phase-iA, the switch S_{A1} connects the bank capacitor C_A to the rectifier and the voltage of C_A is monitored by the comparator through the switch S_{A_S}. The rectifier will charge up the internal 0.5 nF capacitor C_A to the internal reference voltage V_{REF} ($0.5\times V_{DD}$). And then in phase-iB, another capacitor C_B is charged up successively. When both capacitors are fully charged up to V_{REF}, the system moves to the release phase. C_A and C_B are connected in series to boost up the output voltage. In the steady stage, the final output voltage is ideally $2\times V_{REF}$. The switches S_{A1}, S_{B1} and S_{B3} between the rectifier and the battery will not be turned on simultaneously. Therefore, the leakage current from the battery to the rectifier is significantly reduced. The V_{REF} can be replaced with other voltage references, and the internal voltage divider is adopted here to make sure the final output voltage can not exceed V_{DD} for voltage protection.

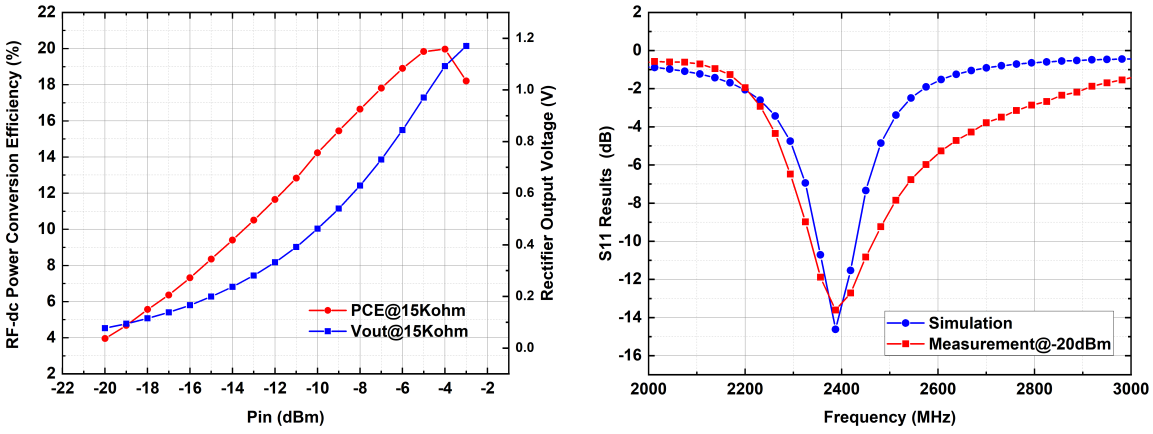

(a) (b)

Figure 4.6: (a) RF-DC PCE and (b) S_{11} measurement with simulation results.

4.2.2 Event-triggered PMU Finite-State-Machine (FSM)

The FSM of the PMU system is illustrated in Fig. 4.3. Notice the modular design of the SC topology, which means that if a higher conversion ratio is required, the system could be expanded to 1:n configuration for higher output voltage. In the release phase, the energy stored in the capacitor is delivered to the output. After the charge is released, the system is back to the idle phase for the next trigger signal. The PMU self-oscillating frequency is dependent on the low modulation frequency (1 kHz in this work) of the input RF waveform because the output of the RF-DC rectifier is changed abruptly along with the dynamic input power. In this approach, if the ambient RF power is too weak or suddenly disappears, the system can maintain in the idle phase and the connection between rectifier and the loading is cut-off to avoid reserve leakage current. The system can process the charge delivery once the capacitor voltage exceeds V_{REF} again.

4.3 Measurement Results

The PMU with rectifier is fabricated in CMOS 130-nm process and the matching network is designed with discrete components. Fig. 4.4 shows the chip micrograph (1.1mm×1.1mm) with the test bench. To imitate the modulated waveform, a 2.4 GHz amplitude modulation (AM)

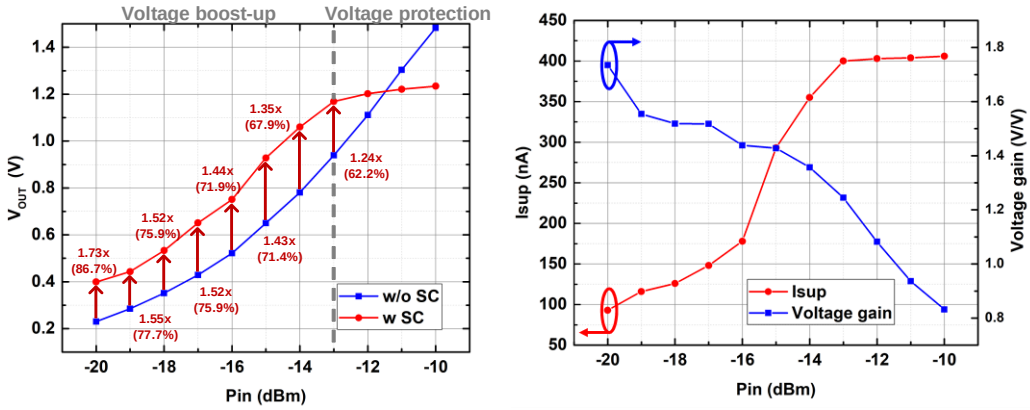

Figure 4.7: (a) RF-EH and (b) SC converter performance. (with a 10-MΩ probe)

waveform at 1 kHz is injected from the RF signal generator for simplicity. In the dual-port PMU with WLAN rectifier measurement, an external DC power supply is used as the PMU supply voltage to characterize the system performance under different V_{DD} before the final integration.

Fig. 4.5 shows the transient output waveform of three different cases under the same input power, including the dual-port system (V_{DD} fed separately), single-port system (V_{DD} fed by the output V_{BAT}), and the direct connection (rectifier connected to V_{BAT} directly without the SC converter). The ripple reduction of our purposed system is 6× compared to the direct connection under the same 22 nF loading capacitor. When the RF power is off, the falling time compared to the generic topology, is 200× and 75× respectively. To characterize the reverse leakage current reduction performance, a constant current source is used to represent the average leakage current. The equivalent average leakage current is 3 nA and 65 nA respectively compared to 7.5 μA in the direct connection, which is reduced by 2500× and 115×. The error introduced by the 10 MΩ probe is also included in the calculation. The rise time is measured as 36 ms (30×) and 13 ms (11×) compared to its leakage reduction performance.

Fig. 4.6a shows the RF-DC rectifier power conversion efficiency (PCE) performance under 2.4 GHz. The rectifier working range is from −20 dBm to −2 dBm with a sensitivity point at −20 dBm for 4% PCE and peak PCE of 20% at −4 dBm. When the input power is larger than

Table 4.1: Literature comparison of the RF-EH system with SC converter.

Work	TMTT-19 [53]	JSSC-19 [49]	IMS-17 [54]	**This work**
Process	Discrete	65 nm	180 nm	**130 nm**
Frequency	2.45 GHz	2.45 GHz	400 MHz	**2.4 GHz**
Rectifier sensitivity	2%@ −20 dBm	2%@ −17 dBm	10%@ −13 dBm	**4%@ −20 dBm**
Rectifier peak PCE	38%@ 13 dBm	48.3%@ −3 dBm	59% @ −8 dBm	**20%@ −4 dBm**
PMU type	Switched-L	Switched-L	SC	**Asyn. SC**
Achieved voltage gain	1.3	NA	<1 (step-down)	**1.73**
PMU working range	NA	>−19 dBm	−12 to −1 dBm	**>−20 dBm**
PMU consumed power	>47 μW*	>1 μW	35 μW*	**28 - 405 nW**
PMU integration	No	No	Yes	**Yes**
Start-up voltage	NA	0.38 V	1.2 V	**0.2 V**
PMU V_{DD}	>3.0 V	NA	>1.2 V	**0.3-1.0 V**
RF-EH V_{OUT}	0-14 V (w/o PMU)	>2.2 V (w PMU)	1.2 V (regulated)	**0.4-1.2 V (w SC)**

−4 dBm, the PCE drops down because the 1.2 V Electrostatic discharge (ESD) voltage clamps the output voltage at 1.2 V for protection. Our design is better in a low power range than other designs even using a more advanced process. The measured S_{11} result in Fig. 4.6b matches with the simulation as well. The S_{11} simulation model includes the rectifier linear model, transmission line and package model.

Fig. 4.7a shows the WLAN RF-EH system output voltage under the capacitor loading with and without the SC converter. The maximum voltage boost gain is measured as 1.73× even in very low input voltage around 0.2 V at the minimum input power −20 dBm (86.7% compared to the ideal conversion gain). When input power is higher than −13 dBm, the system is in voltage protection mode because of the ESD protection. And the SC converter protects the battery from overcharge in this mode. In Fig. 4.7b, the system total power consumption is measured from 28 nW to 405 nW with V_{DD} from 0.3 to 1.0 V, which includes all the circuit blocks.

Compared to other designs listed in Table 4.1, our RF-EH system can provide better performance especially in the low input power range with a fully integrated and low-cost solution. Our proposed SC converter achieves the minimum power consumption down to 28 nW. Its capability of blocking the reverse leakage current and meanwhile, boosting up the output voltage is experimentally verified. Compared to the other PMU that requires larger power consumption, the proposed design can extend its working range to the minimum input power as −20 dBm with an rectifier output of 0.2 V.

4.4 Conclusion

In this work, a dual-band RF-EH system is presented. Particularly, to harvest the RF energy from 2.4 GHz WLAN band more efficiently, a novel asynchronous SC converter is proposed to perform output voltage bootstrapping and reverse leakage current reduction. The whole system can be self-started up when the input power is larger than −20 dBm with the minimum power consumption 28 nW. Our future work is to achieve co-design the PMU with the multi-port antenna.

5. A CMOS ENERGY HARVESTING INTERFACE CIRCUIT WITH CYCLE-TO-CYCLE FREQUENCY-TO-AMPLITUDE CONVERSION MPPT FOR CENTIMETER-SCALE WIND TURBINE

5.1 Introduction

Fig. 5.1 shows the proposed wind energy harvesting system. The permanent magnet generator driven by the blade converts the mechanical power into electrical power. For the AC-DC power conversion, the conventional full-bridge rectifier will introduce a large forward-voltage loss. Therefore, an active-diode embedded negative voltage converter (AD-NVC) with a self-biased comparator is proposed in this work to improve the power conversion efficiency, especially in low-voltage domains. A novel frequency-to-amplitude conversion (FAC) MPPT is proposed to monitor the frequency of the input signal that determines the MPPT voltage. After the rectifier, a DC-DC boost converter performs the MPPT operation to maximize the power extraction and boost up the output voltage for energy storage. The loading can be a specific circuit load for IoT edge-sensing applications or a capacitor buffer for temporal energy storage. Additionally, a low-dropout regulator (LDO) is implemented to provide a stable supply and a reference voltage for the FAC MPPT. This paper is structured as follows. Section II will discuss the details of circuit implementation and analysis. Section III provides measurement results and compares them with previous designs. Finally, Section IV will offer a summary of this work.

5.2 System Implementation and Analysis

To build a power-efficient system for wind EH, the system optimization for the target input voltage and input power is significant. Also, the EH system is designed for autonomous and asynchronous operations to accommodate unpredictable wind behaviors. In this section, the circuit blocks in the proposed EH system are introduced individually.

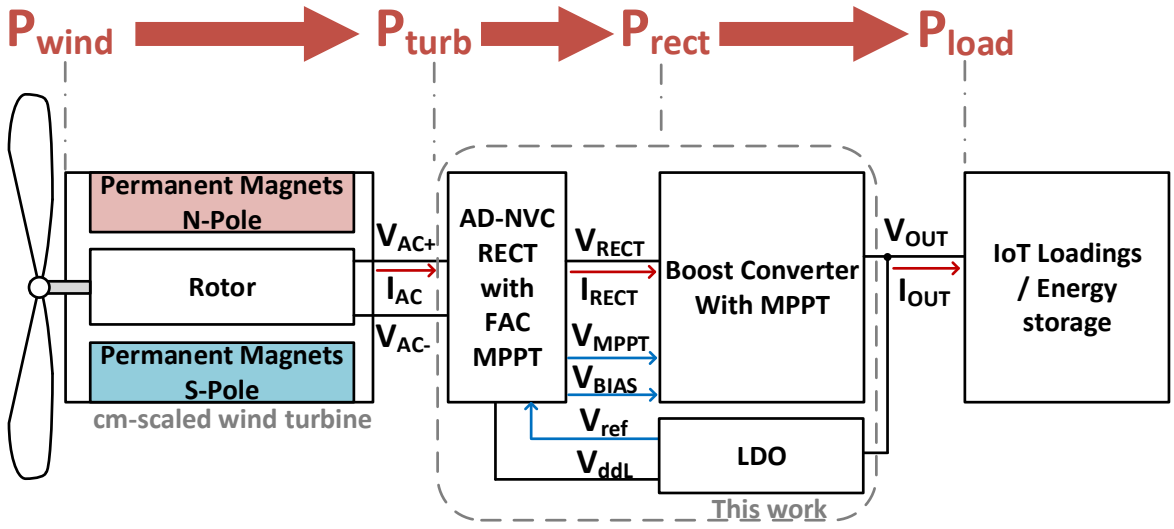

Figure 5.1: Proposed wind energy harvester system for IoT sensors.

5.2.1 AC-DC NVC Rectifier and Active Diode Design

To achieve autonomous operations and self-start-up, conventional active rectifiers are not suitable because they need additional control circuits and well-start-up power supplies. Fig. 5.2a shows the AD embedded NVC (AD-NVC) rectifier architecture details. The active diode is added to control the PMOS pair to reduce the reversed leakage current in the conventional NVC [56, 57, 58]. Compared to the two-step conversion with an additional AD [56, 57], our proposed architecture saves one main conduction switch by just adding a comparator. The area is reduced significantly because the area of the switch is dominant. To ensure the system's self-start-up and autonomous operation, a self-biased current-mode comparator with a positive latched feedback loop [59] is adopted. Additionally, a short-through current suppression buffer (by M_{P5}, M_{P6}, and M_{N5}) is added to provide the rail-to-rail control voltage V_{AD}. The typical idle current is 30 pA when the input signal is absent. And the average current in active mode is 800 nA, without any additional control circuits or additional start-up mechanism [60], which can handle the sparse wind power while providing high power conversion efficiency. Additionally, bulk regulation is added by a cross-coupled PMOS selector. Offset is also skewed by resizing M_{N3} and M_{P1} to prevent

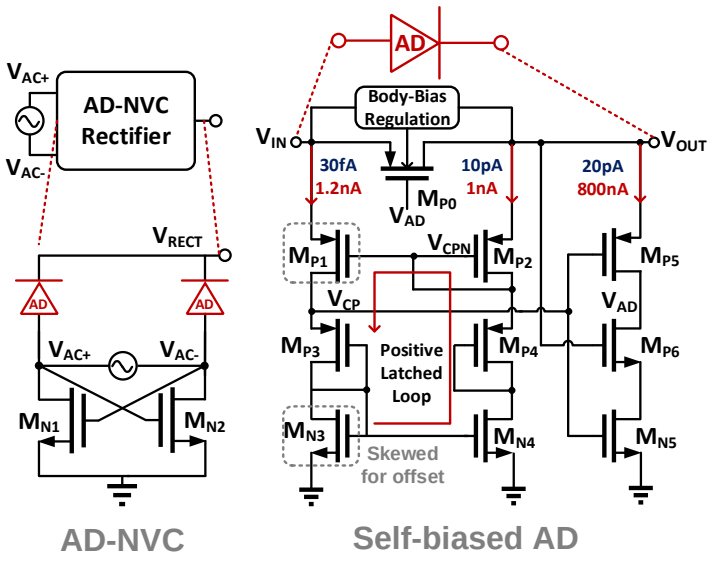

(a)

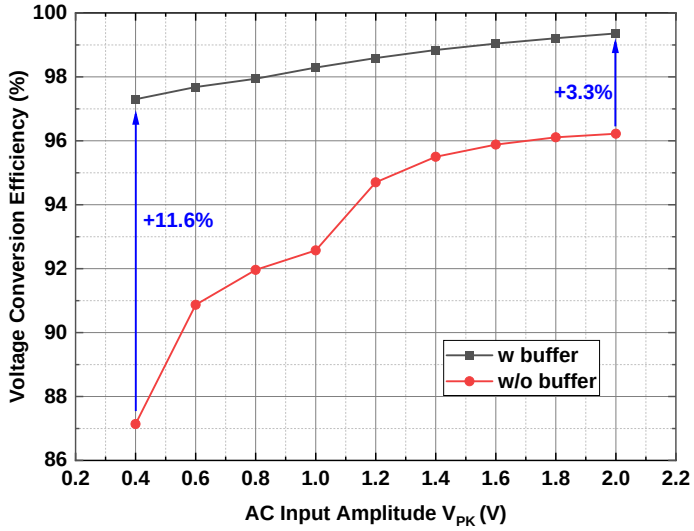

(b)

Figure 5.2: (a) AD-NVC Rectifier and (b) VCE simulation in open-circuit cases.

multiple-conduction oscillations. To examine its rectification abilities in low-voltage conditions, the rectifier voltage conversion efficiency (VCE) under open-circuit conditions is simulated in Fig. 5.2b. The comparison results are also added to highlight the buffer's contribution. The peak VCE is simulated as 99.5% and the VCE is over 97% for an input amplitude from 0.4 to 2.0 V.

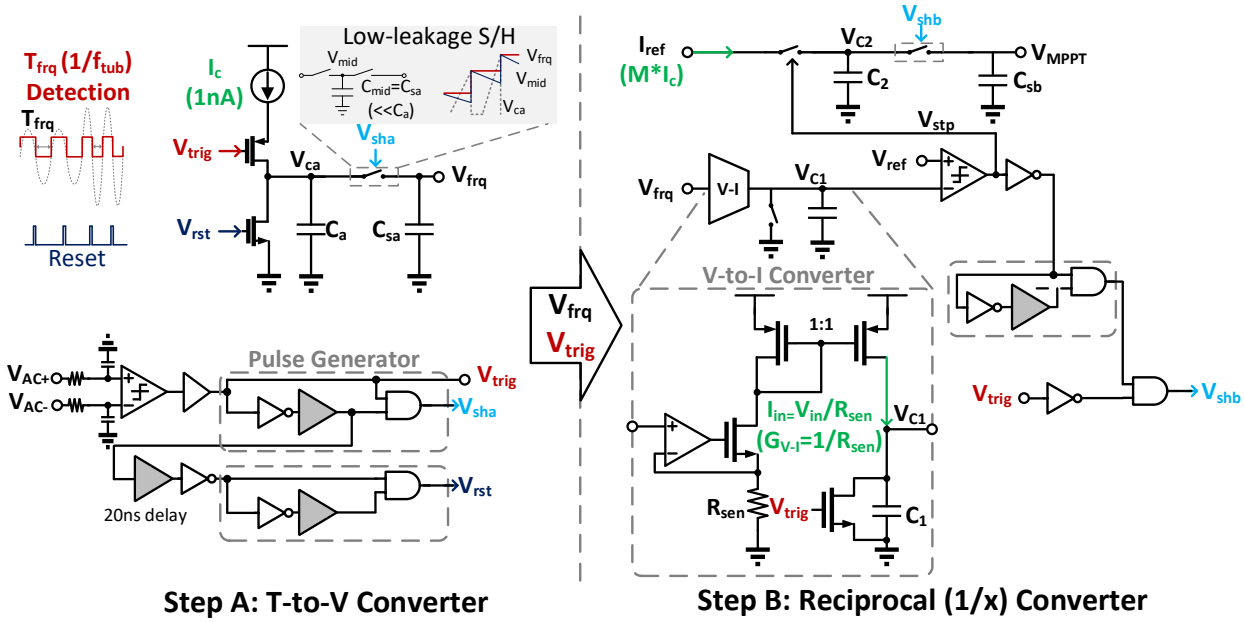

Figure 5.3: Frequency-to-amplitude conversion MPPT schematic.

5.2.2 FAC MPPT Detection and Generation

To generate a reference voltage for the fast MPPT, a novel two-step conversion is proposed in this work. As shown in Fig. 5.3, the differential sine-wave signal V_{AC} is first converted into a square wave V_{trig} based on the polarity flip. In the first step, a time-to-voltage converter monitors V_{trig} and generates an intermediate voltage V_{frq} which is linearly proportional to T_{frq}. In the second step, a reciprocal (1/x) converter is activated to generate the final output voltage V_{MPPT}. The time-to-voltage converter is based on a three-phase (charge-sample-reset) charge-pump introduced in [61]. In the first phase when V_{trig} is logic low, a 1-nA current source charges up C_{a} for the duration of T_{frq}. In the second phase when V_{trig} becomes logic high, V_{c} is sampled on C_{sa} via a low leakage switch controlled by V_{sha}. Finally, in the third phase with a 20 ns delay, C_{a} is reset by V_{rst} and prepares for the next trigger of V_{trig}. To accommodate the low-frequency operation down to 10 Hz, a low leakage sample and hold circuit is also needed. An intermediate sample and hold capacitor C_{mid} is added to alleviate the leakage current from the final output to the ground during the reset phase. By sizing C_{mid} equal to the sample and hold capacitor C_{sa} (2 pF), the voltage ripple

introduced by the leakage current is less than 15 mV in post-layout simulation. Since T_{frq} is half of the rotation cycle ($1/f_{\text{tub}}$), the DC value of V_{frq} can be expressed as:

$$V_{\text{frq}} = \frac{I_{\text{c}} \times T_{\text{frq}}}{C_{\text{a}}} = \frac{I_{\text{c}}}{2 \times f_{\text{tub}} \times C_{\text{a}}} \tag{5.1}$$

Another block is required to generate the MPPT reference by using a reciprocal (1/x) converter. The reciprocal converter is based on capacitor charge conservation principles and this method requires two reference voltages with two voltage-to-current converters [62, 63]. In this work, only one voltage to current converter is required by replacing the other converter with a ratio current source. In Fig. 5.3, the multiplied reference current I_{ref} and the V-I converted current I_{in} charge the capacitor C_1 and C_2 respectively until the voltage on C_1 reaches the reference voltage V_{ref}. The voltage on C_2 is then sampled and stored at C_{sb} (2 pF). In the first step, V_{frq} is refreshed and hold when V_{trig} is in low-to-high transition. And in the second step, the V_{MPPT} is generated and hold from the V_{trig} when V_{trig} is logic low. Our proposed MPPT method can track the turbine frequency after one cycle in the steady-state. V_{MPPT} is refreshed by V_{trig} and its value is updated from V_{frq} which was converted in the previous cycle. Meanwhile, the total power consumption for the MPPT reference voltage generation still remains as low as 400 nW because of its low frequency and nano-ampere operations. The overall frequency-to-voltage conversion can be simply derived as:

$$Ton = \frac{V_{\text{ref}} \times C_1}{G_{\text{V-I}} \times V_{\text{in}}} \tag{5.2}$$

$$V_{\text{MPPT}} = \frac{M \times I_{\text{c}} \times Ton}{C_2} \tag{5.3}$$

$$\text{Finally, } V_{\text{MPPT}} = \frac{2 \times M \times V_{\text{ref}} \times C_1 \times C_{\text{a}}}{G_{\text{V-I}} \times C_2} \times f_{\text{tub}} \tag{5.4}$$

In (5.4), M is the current mirror multiplication ratio. V_{ref} is provided from the internal refer-

ence voltage. $G_{\text{V-I}}$ is the voltage to current gain in the V-to-I converter which depends on the value of on-chip R_{sen}. By sizing M, $G_{\text{V-I}}$, C_{a}, C_1, and C_2, the target linear slope is achieved. In this work, $M = 10$, $G_{\text{V-I}} = 50$ ns, $C_{\text{a}} = 40$ pF, $C_1 = 150$ pF, and $C_2 = 34$ pF, which makes target α numerically equal to V_{ref} for design convenience. V_{MPPT} is proportional to the ratio of $C_{\text{a,1, 2}}$, and also M, which provides more immunity to process variations. (5.4) indicates the simplicity of our proposed method, and this method is also effective in other frequency-to-voltage conversion applications by selecting the proper parameters. In this work, only V_{ref} is reserved to be programmable considering the process variations and adjustments for the different α.

The proposed FAC MPPT eliminates the major drawbacks of the conventional V_{OC} detection MPPT in wind EH applications. For example, by measuring V_{OC} indirectly, the EH system does not need to be disconnected from the wind turbine, which ensures that energy extraction is uninterrupted and extends the working range by eliminating high voltage stress under open-circuit conditions. In addition, the loading effect on the WTG induced voltage is decoupled, enabling an accurate and real-time MPPT suitable for wind EH to be achieved while inheriting the low-cost, fast-response merits of the V_{OC} detection.

5.2.3 Nano-Ampere Peaking Current Source

Although I_{c} does not play a role in (5.4), it is still very important to compromise between the power consumption, capacitor size, and the internal voltage range. Therefore, a constant reference current helps to improve system robustness against PVT variance. A peaking current topology operating in weak inversion regions is employed for its supply independence and capability of operating under low current levels [64]. To achieve a first-order temperature compensation without extra penalty, an N-Well under a diffusion resistor with a positive TC of 65 Ω/°C and a silicided N+ poly resistor with a negative TC of -42 Ω/°C are used to achieve mutual compensation after proper sizing. The designed nominal reference current is 6 nA at room temperature. This nano-ampere current reference has a simulated low TC of 208 ppm/°C, and a small supply sensitivity of 0.55 nA/V.

Overall, the static voltage of V_{MPPT} is plotted in Fig. 5.4a. To cover different target α values,

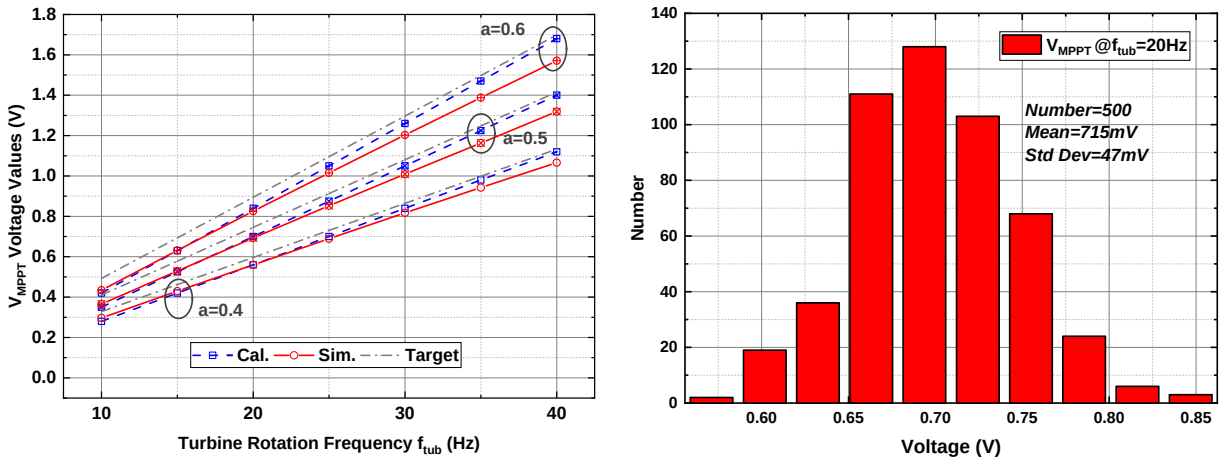

(a) (b)

Figure 5.4: Static V_{MPPT} in simulations (a) $V_{\text{ref}} = 0.4$, 0.5, and 0.6 V respectively, (b) Monte-Carlo simulation results when $f_{\text{tub}} = 20$ Hz. ($\alpha = 0.5$)

the wide-tuning range is achieved by simply adjusting V_{ref}. For example, when $V_{\text{ref}} = 0.5$ V, the achieved α ranges from 0.45 to 0.47 with an average error of 7.6%. The maximum V_{MPPT} deviation is 10% and the overall efficiency difference is less than 3%. When necessary, the deviation can be further minimized by fine tuning V_{ref}. Fig. 5.4b shows the Monte-Carlo simulation results with an intermediate $f_{\text{tub}} = 20$ Hz. The target V_{MPPT} is 0.7 V and the generated mean value is 715 mV with a standard deviation of 47 mV. By replacing the other V-to-I converter in the reciprocal block with the multiplied ratio current branch, the deviation in V_{MPPT} is reduced by 30% and the silicon area is compressed by 20%.

5.2.4 Boost Converter for MPPT Power Extraction

Fig. 5.5 shows the boost converter architecture with the other supportive unit blocks. The boost converter ensures that the loading voltage of the rectifier is near its optimal value for maximum power extractions and boosts up the final output voltage. The boost converter is triggered by a MPPT comparator with hysteresis-control, and the whole system operation is asynchronous without any additional clocking or control elements. The quiescent current of the boost converter is measured as 20 nA in the idle state when the input power is absent (the MPPT comparator is dis-

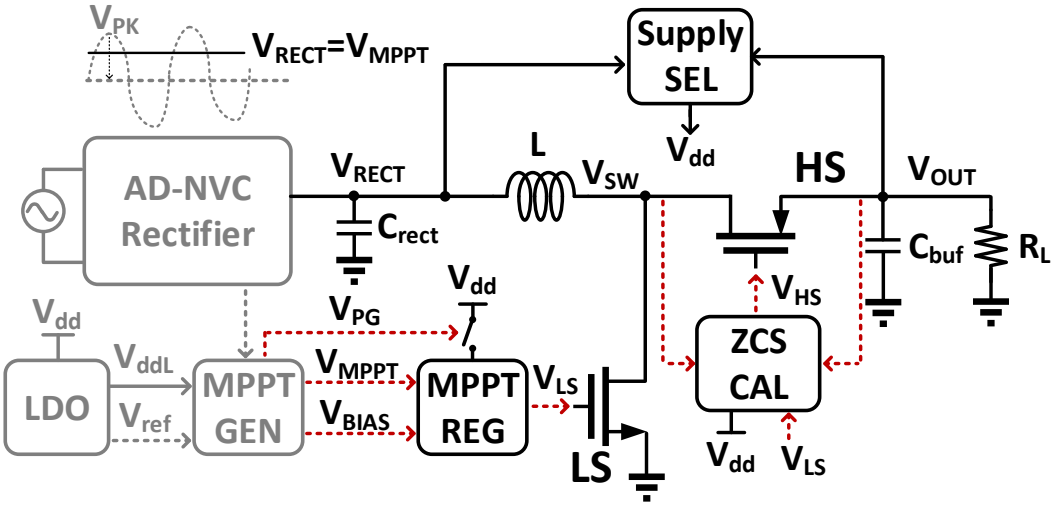

Figure 5.5: Boost converter for power conversion and MPPT.

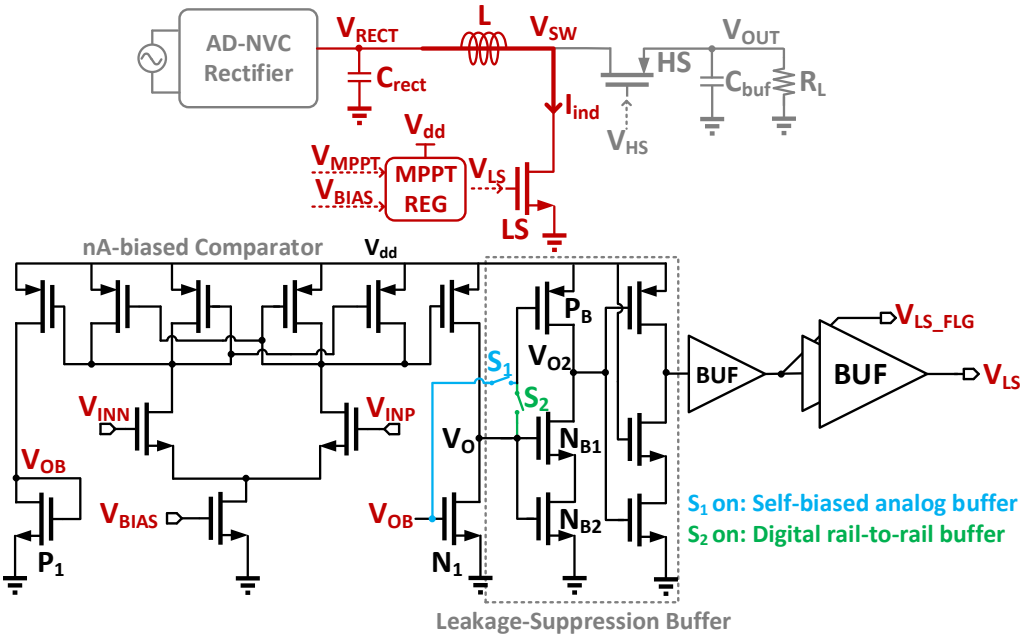

Figure 5.6: Boost converter MPPT comparator schematic.

abled when V_{PG}=0), and the operation power consumption is from 10 to 30 μW, which is adaptive to the input power levels.

To regulate the rectifiers output voltage around the desired maximum power point, a hysteresis

control is implemented for its simplicity and inherent stability by a nA-biased comparator. The hysteresis window is around 2 μs with a switching frequency around 50 KHz according to the simulation. Fig. 5.6 shows the schematic of the MPPT comparator. Once V_{RECT} reaches to V_{MPPT}, the LS switch will be turned on to charge the inductor and V_{RECT} is decreased. And when V_{RECT} hits the low side of the hysteresis window, the LS switch will be turned off. The leakage suppression buffer performs as an analog buffer biased by V_{OB} because the changes of V_{OB} is very small (50 mV in typical) compared to the changes of V_{O} (rail-to-rail). The analog buffer provides a faster response (+13%) by consuming more power (+90%) compared to the digital buffer, which is only triggered by V_{O} as a digital inverter. The control signal V_{LS} of the low-side (LS) NMOS switch also serves as the trigger signal for the following zero-current-switching (ZCS) operations. Therefore, the boost converter operates under asynchronous control, requiring no additional clocking circuit, which simplifies the design and minimizes the consumed power in the idle phase.

To deliver all the available charge stored in the inductor, the high-side (HS) switch is controlled by the ZCS technique [65]. The conventional ZCS uses a high-speed comparator operating only in the HS phase to alleviate the power-speed trade-off. A predefined offset in this comparator is also required to compensate for the path delay. However, the offset is also sensitive to PVT variations [66, 67, 68]. To address this issue, a digital calibration technique is implemented by additional arbitration after the ZCS cycle is finished. The complete ZCS controller is shown in Fig. 5.7. The ZCS comparator is enabled by V_{LS} with a delay of 2 ns. The ZCS comparator detects the voltage difference between V_{SW} and V_{OUT} and turns off the HS switch when V_{SW} reaches V_{OUT}, which means the charge transfer is finished. Then the ZCS comparator itself is deactivated to save power until the next trigger signal. More details of the ZCS-control can be found in [65].

To ensure optimal ZCS, the offset of the ZCS comparator needs to be controlled to provide a timely response. A digital flip-flop (DFF) serves as the arbiter circuit to detect the voltage level of V_{SW} after ZCS with a predefined delay signal $V_{\text{HS\_DLY}}$. If the HS switch is turned off too early when the charging current is still positive, V_{SW} will be charged up higher than V_{OUT} after ZCS. And if the HS switch is turned off too late when the charging current is already negative, then V_{SW}

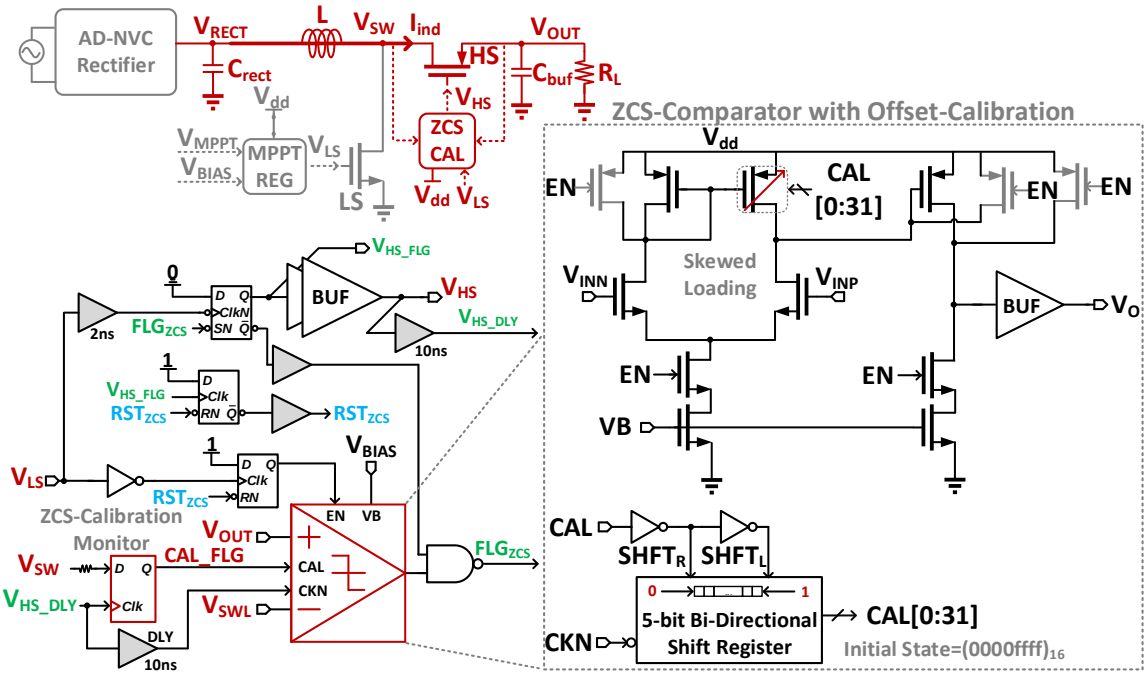

Figure 5.7: ZCS controller with comparator offset self-calibration.

will be discharged lower than GND [66]. Therefore, a simple DFF is sufficient to arbitrate the performance of ZCS with an ESD-protection resistor. A 5-bit offset calibration is employed in the ZCS comparator to provide a unified offset tuning by controlling the active loading devices [69]. The tuning-range is from -40 to 68 mV with an average step resolution of 3.5 mV (Fig. 5.8). The offset in the middle state (Digital Code 15) is skewed to compensate the path delay.

In addition to the circuits for energy delivery, an external capacitorless LDO is designed to provide a 1.5 V voltage supply and a programmable reference voltage from 0.2 to 0.6 V by the resistor dividers. The quiescent current of LDO is 40 nA. A maximum supply voltage selector assists the system start-up. Two cross-coupled NMOS transistors are used to feed the V_{dd} with the maximum voltage between V_{SW} and V_{OUT} automatically. The supply selector automatically charges up the internal V_{dd} through the rectifier output voltage until the normal operation mode is activated. Furthermore, before the V_{dd} is fully charged up, the boost converter is disabled until the power-good signal V_{PG} is generated.

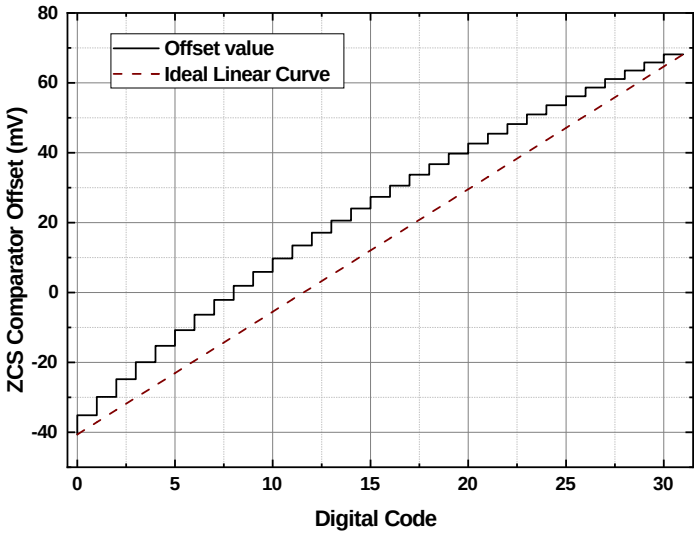

Figure 5.8: ZCS comparator skewed-offset simulation.

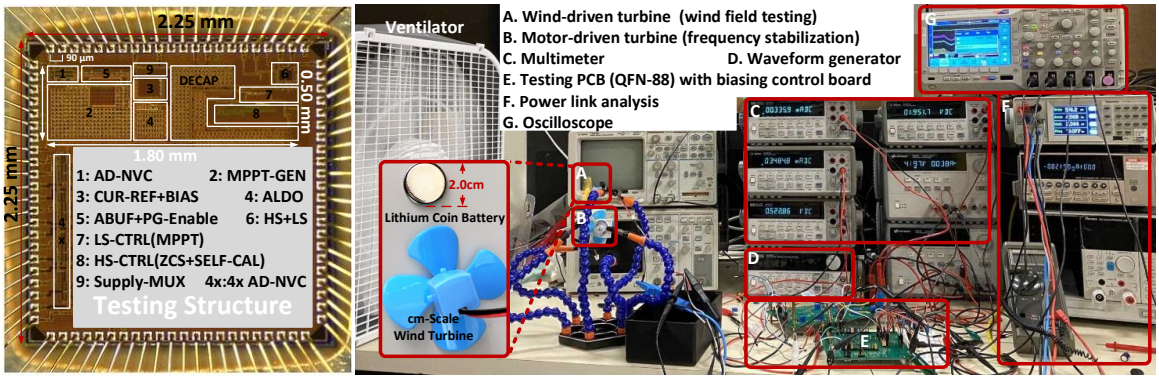

Figure 5.9: Chip micro-photograph and test-bench.

5.3 Measurement

The EH system is fabricated in a CMOS 180-nm technology. The active area is 0.9 mm^2, and a $4\times$-area AD-NVC rectifier is also fabricated as a counterpart for performance comparisons. The off-the-shelf components include μF-level loading capacitors and a 47-μH inductor. The chip micro-photograph is shown in Fig. 5.9, together with the testing setup. A ventilator with a handheld wind-speed measurement instrument is used to characterize the EH system performance in wind

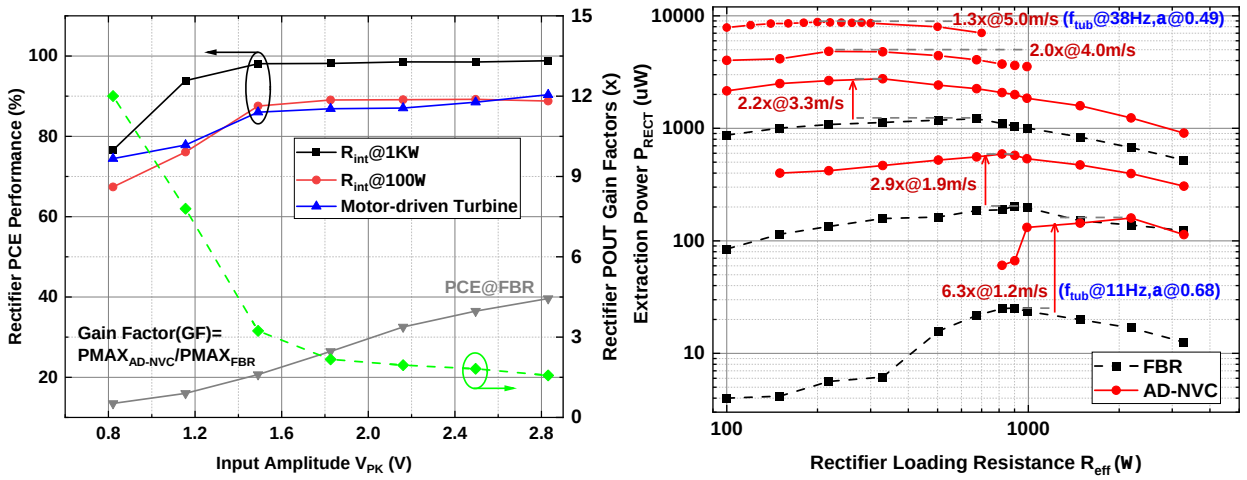

(a) (b)

Figure 5.10: Rectifier (a) PCE tested in motor-driven testing, (b) harvested output power in wind-field testing.

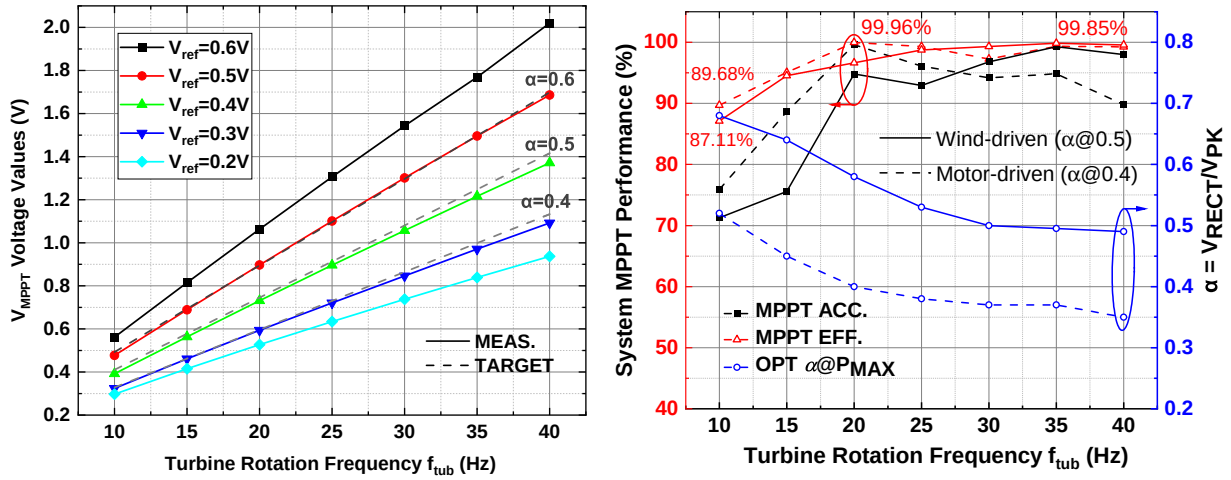

(a) (b)

Figure 5.11: (a) V_{MPPT} static output voltage, (b) MPPT performance.

field-testing. Meanwhile, a DC-motor directly drives the turbine for testing under stabilized rotation frequencies, thereby providing the driving power needed to overcome the demanding torque under different loading conditions.

Before testing the overall system performance, the individual performance of each block is

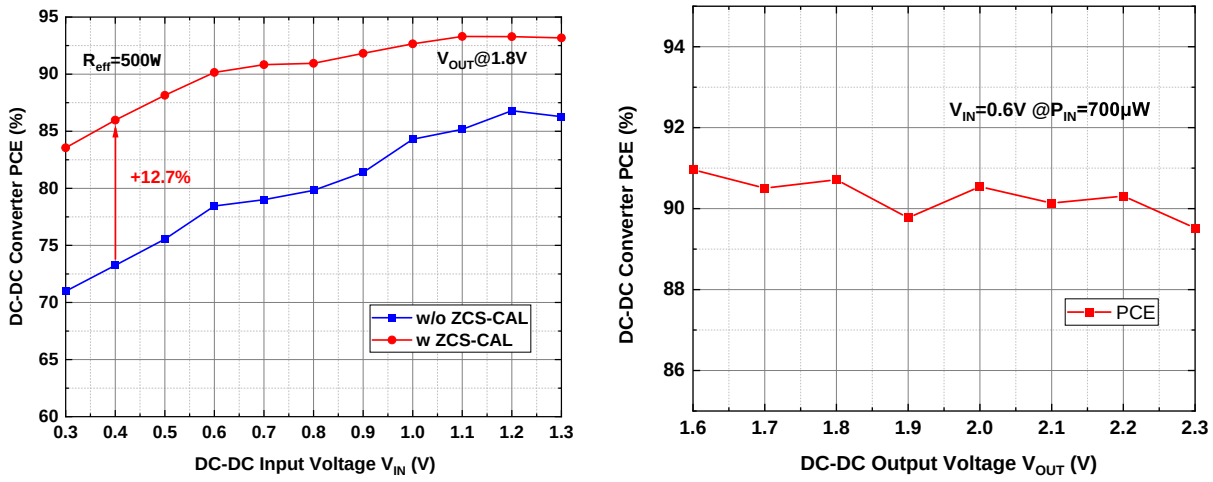

(a) (b)

Figure 5.12: DC-DC converter PCE versus (a) input voltage, (b) output voltage.

first examined. The power conversion efficiency of the AD-NVC rectifier is plotted in Fig. 5.10a. When R_{int}=1 KΩ, the power conversion efficiency (PCE) of the AD-NVC is above 94% when V_{PK} is larger than 1.2 V, indicating its high efficiency for low-voltage and μWatt-level EM applications. The PCE performance drops to 89% when R_{int}=100 Ω because of the larger conduction loss. To quantify the power extraction abilities, the achievable energy extraction gain compared to a conventional Schottky-diode-based full-bridge rectifier (FBR) is also shown in Fig. 5.10a. Under the same stabilized frequency condition, the output power of the AD-NVC rectifier is $12\times$ compared to the FBR in the low-frequency range, indicating its supreme performance especially in low-voltage domains. In Fig. 5.10b, the performance comparison is also employed with similar wind speed conditions. The AD-NVC achieves a $6.3\times$ extracted output power gain in low-wind conditions at 1.2 m/s, while still maintaining at $2.0\times$ in 4.0 m/s. Notably, the optimal loading R_{eff} is larger in the wind-field testing compared to the motor-driven testing, which is because of the loading effect in WTG discussed in Section II.

The V_{MPPT} under V_{ref} from 0.2 V to 0.6 V is plotted in Fig. 5.11a. The results show a wide tuning ability and a feasible tuning solution in the proposed FAC MPPT, which makes the V_{MPPT} applicable for other frequency-to-voltage conversion applications, such as low-cost wind-speed

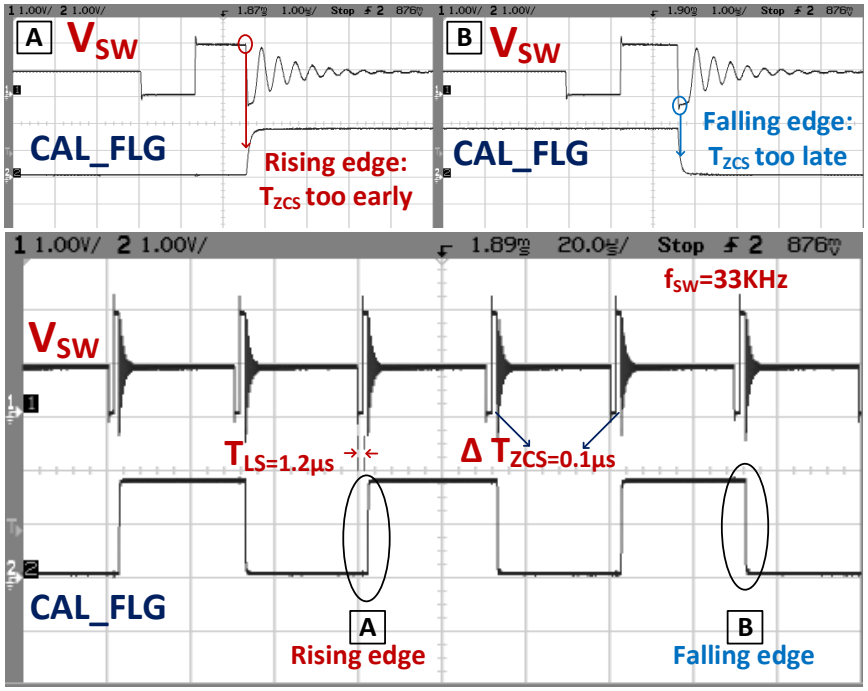

(a)

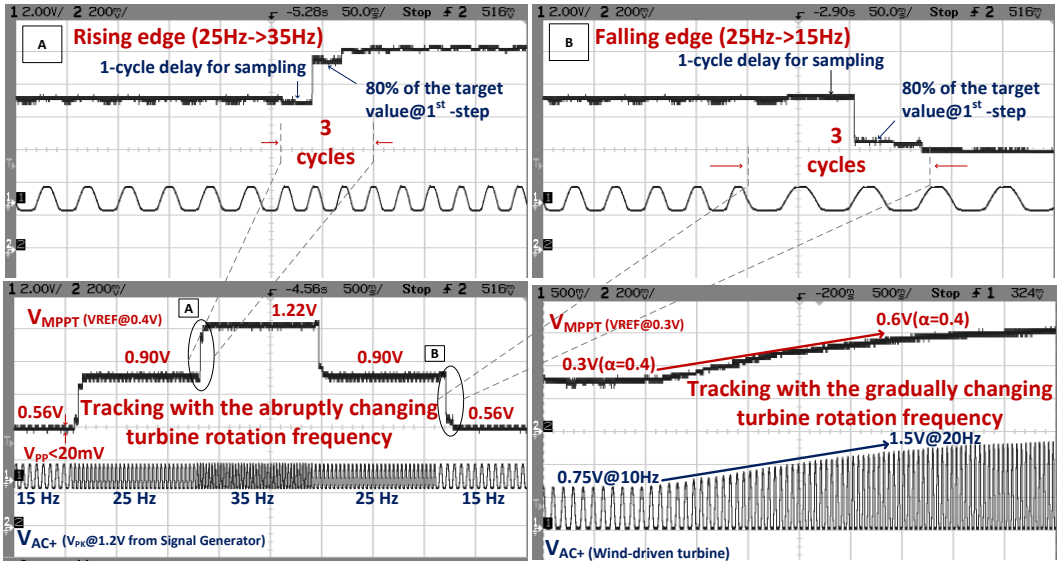

(b)

Figure 5.13: Transient waveform of (a) ZCS self-calibration, (b) MPPT response.

detection. With the V_{ref} value trimmed down by 100 mV, the accuracy above 95% is achieved compared to target α. Therefore, as characterized in Fig. 5.11b, an α of 0.4 ensures the optimal MPPT performance in the motor-driven testing. And an α of 0.5 maximizes the MPPT performance in the

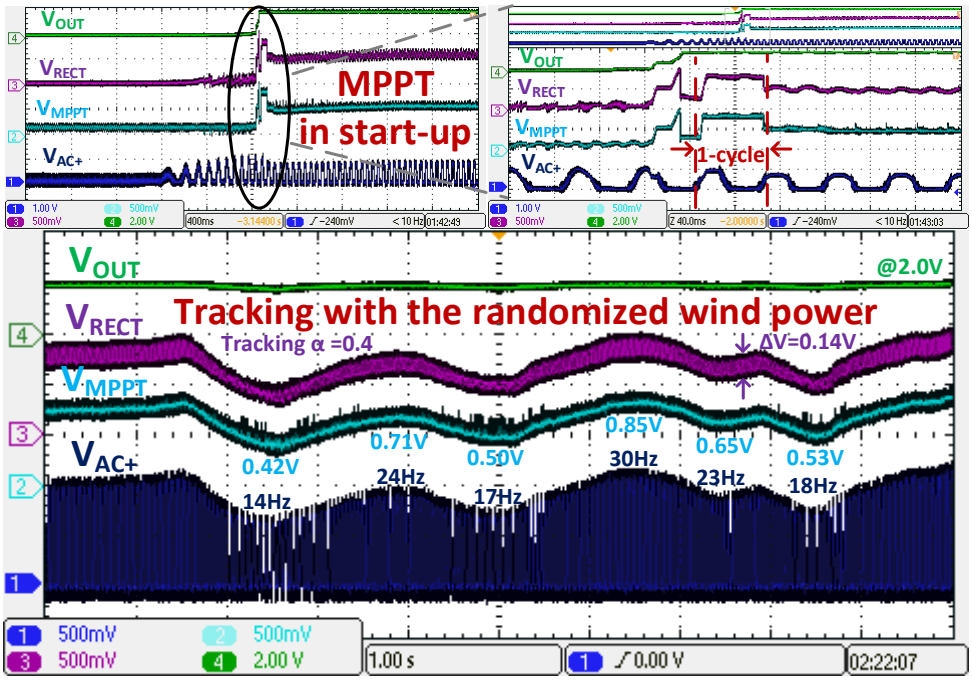

Figure 5.14: System with MPPT in a wind field-testing demonstration

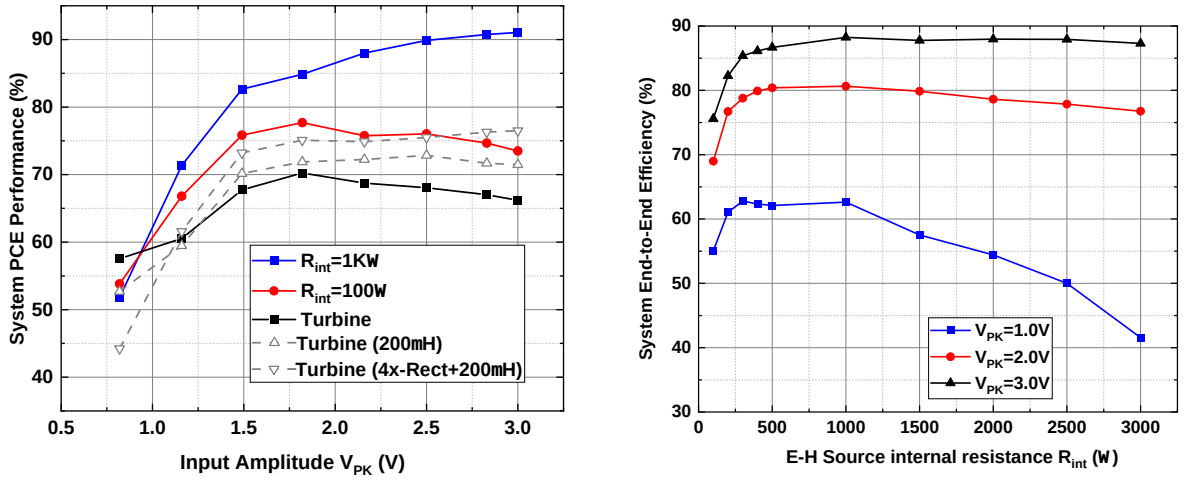

(a) (b)

Figure 5.15: System performance of (a) PCE, (b) end-to-end EFF.

wind-driven testing, which achieves a peak MPPT efficiency of 99.85% with an MPPT accuracy of 99.27%. The variance of an optimal α also depicts the necessity of tuning α values for different EH scenarios. The optimal α is close to 0.4 in the motor-driven testing because the turbine is rep-

resented as an ideal voltage source without any loading effects. However, in wind-driven testing, the torque equilibrium performs as an additional loss and leads to a higher optimal α. Notably, the motor-driven conditions can represent EH applications for ocean waves or marine current energy where the generated driven-torque is dominant [70].

The PCE of the DC-DC converter is shown in Fig. 5.12. a 200-mΩ low-DCR 47-μH shielded inductor is selected for low cost and high efficiency. Thanks to the contribution of the self-calibration technique in the ZCS, the PCE is maintained above 90% in a wide input voltage ranging from 0.6V, and the output voltage covers from 1.6 V to 2.2 V, which achieves a 12.7% peak performance improvement compared to the performance when self-calibration is disabled. The transient response of the ZCS self-calibration in the steady-state is plotted in Fig. 5.13a. The optimal ZCS point is locked by two back-and-forth digital states, with a 0.1 μs resolution in the adjacent state. Although the ringing appears after ZCS, the HS reverse recovery time is larger than 200 ns after the self-calibration is finished, so it does not affect the operations of self-calibration.

Fig. 5.13b demonstrates the V_{MPPT} response with different types of frequency changes. First, the MPPT response under abrupt frequency changes is tested. The input sinusoidal signal is generated from a signal generator with a step frequency of 10 Hz. The zoom-in plot shows that the proposed MPPT method can track the abrupt frequency change within 3 turbine cycles, with an 80% accuracy in the first turbine cycle. when tested with the gradually changing wind-driven turbine, the cycle-to-cycle amplitude V_{PK} difference is less than 2%; meanwhile, the V_{MPPT} can still track this small change smoothly. The high-resolution capability is maintained while the fast response is also achieved by the variable and adaptive step response. The V_{MPPT} is triggered by the turbine operation itself. Therefore, no additional clocking element or control circuits are required. The whole interface IC, including the AD-NVC rectifier, the MPPT functions, and the DC-DC converter, operates autonomously in favor of modular designs.

The system tested in an actual wind field is shown in Fig. 5.14. The loading is a 10-μF capacitor with a 5-KΩ resistance. After the system is stabilized at 2.0 V from start-up, the correct V_{MPPT} is generated after one turbine cycle, demonstrating the ability of the MPPT to operate in shock

or burst modes. For fast varying wind power, V_{MPPT}, V_{RECT}, and $V_{\text{AC+}}$ are tracking the turbine frequency from cycle to cycle. As previously mentioned, different loading conditions affect the operations of the EM turbine and introduce errors in conventional open-circuit detection methods. However, the proposed FAC MPPT monitors the turbine frequency f_{tub} in real time. The envelope depicts the dynamic and accurate response of the proposed MPPT operations in different wind EH scenarios, such as the continuous and shock excitation.

In Fig. 5.15a, the overall system PCE is measured in motor-driven testing, which is defined by the percentage of the output power compared to the average AC input power. The AC input power is measured by an AC/DC power analyzer. With a well-defined R_{int} source, the peak PCE is 91% when R_{int}=1 KΩ, while the peak PCE is 77.7% with a smaller R_{int}=100 Ω. The PCE is dropped down mainly because of the conduction loss with the increasing conduction current reaching up to 10 mA. When tested with the turbine, the peak PCE is 70% when V_{PK}=1.8 V, which is also degraded compared to the well-defined R_{int} source. However, in wind field-testing, the PCE performance in the practical implementation is between R_{int}=1000 Ω and R_{int}=100 Ω in two cases. An alternative rectifier with a quadruple area coverage can improve the overall system performance by 5% if PCE improvement is demanded. Meanwhile, a larger inductor of 200-μH can also help in the large V_{PK} conditions by reducing the peak inductor current. The peak PCE is improved by 10% with a performance degradation of 13.3% in low power domains, showing the design trade-off for the low cost (area and form factors) and optimal PCE for different operation ranges. In Fig. 5.15b, the end-to-end efficiency (EFF) is characterized by changing R_{int}. The end-to-end EFF is determined by the PCE performance and the power extraction ability (MPPT efficiency). A peak end-to-end EFF is measured as 88.2% when V_{PK}=3.0 V, and it is kept as 62.8% with low V_{PK}=1.0 V, indicating the high efficiency is still reserved in low-voltage and μW EH applications. The EFF is dropped down at low input power domains mainly because the minimum DC-DC converter operation power is set to 8 μW.

Table 5.1 draws a comparison with other EM or AC-type EH systems with comparable output power or input voltage. The presented system achieves fast and wide range MPPT for cycle-to-

Table 5.1: Wind-EH system performance compared to state-of-arts.

References	[19] JSSC	[24] JSSC	[11] TPE	[23] JSSC	**This work**
Process	350nm BCD	350nm	Discrete	180nm	**180nm**
Active Area	4.7mm^2	1.3mm^2	NA	0.47mm^2	**0.9mm^2**
E-H Type	EM/PEH	EM	EM turbine	PEH	**EM turbine**
E-H F_{SRC}	100-400 Hz	64, 109 Hz	10-100 Hz	53, 85 Hz	**10-40 Hz**
Architecture	Act. Rect. +Buck-Boost	NVC+AD +Boost	Act. Rect. +Boost	SaS Rectifier	**AD-NVC +Boost**
Inductor Value	10 mH	1 mH	10 mH	1 mH	**47 μH**
Output Power	0.03-10 mW	0.004-1 mW	1-70 mW	0.4-16 μW	**0.1-10 mW**
Output Voltage	1-8 V	4.2 V	3.0 V	0.5-2.0 V	**1.6-2.0 V**
MPPT Method	V_{OC} Detection	Conduction Angle	R_{LOAD} Emulation	I-to-V F_{SW}. Tuning	**Freq-to-V_{PK} Conversion**
MPPT-GEN PWR (EFF*)	10 μW (66.7%)	40 nW (99.0%)	267 μW (73.3%)	230 nW (42.5%)	**380 nW (99.6%)**
MPPT Step Response	9.09 ms/V	Fixed Step 50 mV/Cycle	NA.	Fixed Step (F_{SW}=2.5K Hz)	**25-250 mV/Cycle**
MPPT Cycles (over 1/F_{SRC})	1 (For V_{OC})	△V/0.05 (20@△V=1 V)	Always -on	F_{SW} / F_{SRC} (>30)	**<3 (>80%@1st step)**
F_{SRC} Tracking	NO	NO	NO	NO	**YES**
Voltage Stress	High	LOW	NA.	High	**LOW**
MPPT ACC. MPPT EFF.	η_V=99.0% η_P=99.0%	NA. η_P=90%	NA. NA.	η_V=80% η_P=91%	**η_V=99.27% η_P=99.85%**
Peak System EFF (End-to-End)	80% (only buck-boost)	95%@ V_{PK}=3.6V	60%@ V_{PK}=10.0V	42%@ V_{PK}=2.0V	**88.2%@ V_{PK}=3.0V**
EFF @V_{PK}=1.0V	NA.	50%	NA.	NA.	**62.8%**
Rectification FoM* (Periodic)	NA.	NA.	1.2x@ 8.5m/s V_{PK}=8.5V 3.0x@ 2.3m/s V_{PK}=1.5V	5.4x (strong) V_{PK}=2.0V 5.6x (weak) V_{PK}=1.3V	**1.3x@ 5.0m/s V_{PK}=2.7V 6.3x@ 1.2m/s V_{PK}=0.9V**

*MPP-GEN EFF=(1-$P_{MPPT\text{-}GEN}/P_{OUT(MIM)}$) *100%, the MPP information processing efficiency

**FoM=$P_{OUT(MAX)}$@AD-NVC/$P_{OUT(MAX)}$@FBR, the energy extraction gain

cycle tracking with an ultra-low-power consumption of 380 nW, and a MPPT processing efficiency larger than 99.6%. A $20\times$ smaller inductor (47-μH) is selected for reduced form factor and low-cost design. The whole system including the rectifier design is optimized for autonomous and sub-1V operations, achieving a 630% energy extraction gain at low wind-speed conditions of 1.2 m/s (V_{PK}= 0.9 V). Compared to [26], the proposed system achieves a comparable peak end-to-end EFF with less active silicon area and a smaller inductor, while a $10\times$ power delivery ability

is achieved. Moreover, the proposed FAC MPPT achieved cycle-to-cycle MPPT with a fast and adaptive response, while maintaining the least power overhead compared to the harvested power [20, 11, 25]. The highest MPPT efficiency was also achieved with wide-tuning abilities for the wide-range operations from 10 to 40 Hz ($4\times$). The allowed operation wind speed is covered from 1.0 to 5.0 m/s. The minimum MPPT operation range is extended by $2.3\times$ compared to [11], which is limited by the minimum cut-in wind speed of the wind turbine itself.

5.4 Conclusion

This work presents a power-efficient EH system for the EM wind turbine EH. The system is optimized for a wide input power range with self-start-up and autonomous operations. The proposed FAC MPPT maximizes the power extraction ability under different wind conditions. The fast cycle-to-cycle MPPT transient response and short settling time (one cycle) can ensure that the EH system is suitable for continuous energy extraction, as well as the shock or burst excitation. The total quiescent current of the EH system is 150 nA when the wind power is absent. To the best of the authors knowledge, this is the first IC prototype for a cm-scale wind turbine EH which achieves a real-time MPPT with the highest reported MPPT efficiency. The proposed FAC MPPT design is low cost with wide-tuning abilities, which is suitable for other linear frequency-to-voltage conversion applications, such as low-cost wind speed detection.

6. CONCLUSION

In this dissertation, the energy harvesting techniques suitable for IoT applications are reviewed. Particularly, the ambient RF energy and wind energy profiles are examined for EH purposes with different EH scenarios. The major challenges and the limitations in conventional MPPT methods are analyzed and different EH PMU systems are designed in this dissertation accordingly.

Chapter 2 presented a reconfigurable and self-start-up RF EH rectifier for wide input-power range operations. The FOCVA MPPT is proposed to relieve the burden of non-linear MPPT requirement of cascading DC-DC converter for wide range operations. To further improve the overall end-to-end efficiency, chapter 3 introduced a fully-integrated RF EH system. An accurate conceptual model is provided for rectifier efficiency and MPPT analysis. Based on the model, a hill-climbing MPPT method is developed for resistive SoC loading. The proposed MPPT function can detect and determine the optimal rectifier stage for different loading and different input power, with a peak MPPT power efficiency of 99.8%. The end-to-end RF EH abilities are demonstrated in field-testing with a high-gain antenna, which can harvest 1 μW at the output with a 10-dBm transmitter at a distance of 1.78m.

Chapter 4 proposed a fully-integrated SC converter for RF EH applications. The SC converter reduces the system reverse leakage current and provides an output voltage bootstrapping function. With asynchronous control, an ultra-low-power consumption down to 28 nW is achieved with a high voltage boost gain of 1.73 (VCE=86.7%) at 0.4 V.

Chapter 5 demonstrated a power-efficient EH system to extract the energy from a cm-scale EM wind turbine. Compared to a full-bridge rectifier, a 630% energy extraction gain is measured at a low wind speed of 1.2 m/s. To tackle the challenge in MPPT for frequently-changing wind power, a FAC MPPT method is proposed for cycle-to-cycle MPPT with ultra low power consumption. The EH system with MPPT targets for wind speeds from 1.0 to 5.0 m/s, with a peak MPPT accuracy of 99.27%, and a MPPT efficiency of 99.85%. The interface circuits are designed with self-biasing and self-start-up functions, and the total quiescent current of the EH system is 150 nA.

REFERENCES

[1] J. A. Paradiso and T. Starner, "Energy scavenging for mobile and wireless electronics," *IEEE Pervasive Computing*, vol. 4, no. 1, pp. 18–27, 2005.

[2] K. Mimis, D. R. Gibbins, S. Dumanli, and G. T. Watkins, "The ant and the elephant: ambient RF harvesting from the uplink," *IET Microwaves, Antennas & Propagation*, vol. 11, no. 3, pp. 386–393, 2017.

[3] S. Shen, C. Chiu, and R. D. Murch, "A dual-port triple-band L-probe microstrip patch rectenna for ambient RF energy harvesting," *IEEE Antennas and Wireless Propagation Letters*, vol. 16, pp. 3071–3074, 2017.

[4] A. K. Moghaddam, J. H. Chuah, H. Ramiah, J. Ahmadian, P. Mak, and R. P. Martins, "A 73.9%-efficiency CMOS rectifier using a lower DC feeding (LDCF) self-body-biasing technique for far-field RF energy-harvesting systems," *IEEE Transactions on Circuits and Systems I: Regular Papers*, vol. 64, no. 4, pp. 992–1002, 2017.

[5] M. Stoopman, S. Keyrouz, H. J. Visser, K. Philips, and W. A. Serdijn, "Co-design of a CMOS rectifier and small loop antenna for highly sensitive RF energy harvesters," *IEEE Journal of Solid-State Circuits*, vol. 49, no. 3, pp. 622–634, 2014.

[6] M. A. Abouzied and E. Sánchez-Sinencio, "Low-input power-level CMOS RF energy-harvesting front end," *IEEE Transactions on Microwave Theory and Techniques*, vol. 63, no. 11, pp. 3794–3805, 2015.

[7] J. Yi, W. Ki, and C. Tsui, "Analysis and design strategy of UHF micro-power CMOS rectifiers for micro-sensor and RFID applications," *IEEE Transactions on Circuits and Systems I: Regular Papers*, vol. 54, no. 1, pp. 153–166, 2007.

[8] K. R. Sadagopan, J. Kang, Y. Ramadass, and A. Natarajan, "A 960pW co-integrated-antenna wireless energy harvester for WiFi backchannel wireless powering," *2018 IEEE International*

Solid - State Circuits Conference - (ISSCC), pp. 136–138, 2018.

[9] M. Habibzadeh, M. Hassanalieragh, A. Ishikawa, T. Soyata, and G. Sharma, "Hybrid solar-wind energy harvesting for embedded applications: Supercapacitor-based system architectures and design tradeoffs," *IEEE Circuits and Systems Magazine*, vol. 17, no. 4, pp. 29–63, 2017.

[10] Y. K. Tan and S. K. Panda, "Self-autonomous wireless sensor nodes with wind energy harvesting for remote sensing of wind-driven wildfire spread," *IEEE Transactions on Instrumentation and Measurement*, vol. 60, no. 4, pp. 1367–1377, 2011.

[11] Y. K. Tan and S. K. Panda, "Optimized wind energy harvesting system using resistance emulator and active rectifier for wireless sensor nodes," *IEEE Transactions on Power Electronics*, vol. 26, no. 1, pp. 38–50, 2011.

[12] D. Porcarelli, D. Spenza, D. Brunelli, A. Cammarano, C. Petrioli, and L. Benini, "Adaptive rectifier driven by power intake predictors for wind energy harvesting sensor networks," *IEEE Journal of Emerging and Selected Topics in Power Electronics*, vol. 3, no. 2, pp. 471–482, 2015.

[13] E. Sardini and M. Serpelloni, "Self-powered wireless sensor for air temperature and velocity measurements with energy harvesting capability," *IEEE Transactions on Instrumentation and Measurement*, vol. 60, no. 5, pp. 1838–1844, 2011.

[14] P. D. Mitcheson, E. M. Yeatman, G. K. Rao, A. S. Holmes, and T. C. Green, "Energy harvesting from human and machine motion for wireless electronic devices," *Proceedings of the IEEE*, vol. 96, no. 9, pp. 1457–1486, 2008.

[15] S. Nabavi and L. Zhang, "Portable wind energy harvesters for low-power applications: A survey," *Sensors*, vol. 16, no. 7, p. 1101, 2016.

[16] "National Centers for Environmental Information." `https://www.ncei.noaa.gov/`.

[17] M. M. Ababneh, S. Perez, and S. Thomas, "Optimized mini notched turbine energy harvesting using resistor emulation approach and particle swarm optimization," in *SoutheastCon 2017*, pp. 1–6, 2017.

[18] N. Rezaei-Hosseinabadi, A. Tabesh, and R. Dehghani, "A topology and design optimization method for wideband piezoelectric wind energy harvesters," *IEEE Transactions on Industrial Electronics*, vol. 63, no. 4, pp. 2165–2173, 2016.

[19] Y. Hu, I. Chen, and T. Tsai, "A piezoelectric vibration energy harvesting system with improved power extraction capability," in *2016 IEEE Asian Solid-State Circuits Conference (A-SSCC)*, pp. 305–308, 2016.

[20] M. Shim, J. Kim, J. Jeong, S. Park, and C. Kim, "Self-powered 30 μW to 10 mW piezoelectric energy harvesting system with 9.09 ms/v maximum power point tracking time," *IEEE Journal of Solid-State Circuits*, vol. 50, no. 10, pp. 2367–2379, 2015.

[21] Z. M. Dalala, Z. U. Zahid, W. Yu, Y. Cho, and J. Lai, "Design and analysis of an MPPT technique for small-scale wind energy conversion systems," *IEEE Transactions on Energy Conversion*, vol. 28, no. 3, pp. 756–767, 2013.

[22] C. Lu, C. Tsui, and W. Ki, "Vibration energy scavenging system with maximum power tracking for micropower applications," *IEEE Transactions on Very Large Scale Integration (VLSI) Systems*, vol. 19, no. 11, pp. 2109–2119, 2011.

[23] J. Hsieh and T. Tsai, "An AC-DC wind energy harvesting circuit with extended input-voltage range and 95% tracking efficiency," *2018 IEEE International Symposium on Circuits and Systems (ISCAS)*, pp. 1–4, 2018.

[24] A. Quelen, G. Pillonnet, P. Gasnier, F. Rummens, and S. Boisseau, "Electromagnetic mechanical energy-harvester IC with no off-chip component and one switching period MPPT achieving up to 95.9% end-to-end efficiency and 460% energy-extraction gain," in *2020 IEEE International Solid-State Circuits Conference (ISSCC)*, pp. 490–492, 2020.

[25] Y. Peng, K. D. Choo, S. Oh, I. Lee, T. Jang, Y. Kim, J. Lim, D. Blaauw, and D. Sylvester, "An efficient piezoelectric energy harvesting interface circuit using a sense-and-set rectifier," *IEEE Journal of Solid-State Circuits*, vol. 54, no. 12, pp. 3348–3361, 2019.

[26] J. Leicht and Y. Manoli, "A 2.6 μW 1.2 mW autonomous electromagnetic vibration energy harvester interface IC with conduction-angle-controlled MPPT and up to 95% efficiency," *IEEE Journal of Solid-State Circuits*, vol. 52, no. 9, pp. 2448–2462, 2017.

[27] T. Paing, J. Shin, R. Zane, and Z. Popovic, "Resistor emulation approach to low-power RF energy harvesting," *IEEE Transactions on Power Electronics*, vol. 23, no. 3, pp. 1494–1501, 2008.

[28] G. C. Martins and W. A. Serdijn, "An RF energy harvester with mppt operating across a wide range of available input power," *2018 IEEE International Symposium on Circuits and Systems (ISCAS)*, pp. 1–5, 2018.

[29] T. Huang, C. Hsieh, Y. Yang, Y. Lee, Y. Kang, K. Chen, C. Huang, Y. Lin, and M. Lee, "A battery-free 217 nW static control power buck converter for wireless RF energy harvesting with α-calibrated dynamic on/off time and adaptive phase lead control," *IEEE Journal of Solid-State Circuits*, vol. 47, no. 4, pp. 852–862, 2012.

[30] X. Hua and R. Harjani, "A 5W-5mW input power range, 03.5V output voltage range RF energy harvester with power-estimator-enhanced mppt controller," *2018 IEEE Custom Integrated Circuits Conference (CICC)*, pp. 1–4, 2018.

[31] M. A. Abouzied, K. Ravichandran, and E. Sánchez-Sinencio, "A fully integrated reconfigurable self-startup RF energy-harvesting system with storage capability," *IEEE Journal of Solid-State Circuits*, vol. 52, no. 3, pp. 704–719, 2017.

[32] Z. Zeng, X. Li, A. Bermak, C. Tsui, and W. Ki, "A WLAN 2.4-Ghz RF energy harvesting system with reconfigurable rectifier for wireless sensor network," *2016 IEEE International Symposium on Circuits and Systems (ISCAS)*, pp. 2362–2365, 2016.

[33] S. Shieh and M. Kamarei, "Transient input impedance modeling of rectifiers for RF energy harvesting applications," *IEEE Transactions on Circuits and Systems II: Express Briefs*, vol. 65, no. 3, pp. 311–315, 2018.

[34] L. Liu *et al.*, "An ultra-low-power integrated RF energy harvesting system in 65-nm CMOS process," *Circuits, Systems, and Signal Processing*, vol. 35, no. 2, pp. 421–441, Feb 2016.

[35] Y. Lu, H. Dai, M. Huang, M. Law, S. Sin, S. U, and R. P. Martins, "A wide input range dual-path CMOS rectifier for RF energy harvesting," *IEEE Transactions on Circuits and Systems II: Express Briefs*, vol. 64, no. 2, pp. 166–170, 2017.

[36] H. J. Visser *et al.*, "Ambient RF energy scavenging: GSM and WLAN power density measurements," *2008 38th European Microwave Conference, Amsterdam*, 2008.

[37] Yu-Jiun Ren and Kai Chang, "5.8-GHz circularly polarized dual-diode rectenna and rectenna array for microwave power transmission," *IEEE Transactions on Microwave Theory and Techniques*, vol. 54, no. 4, pp. 1495–1502, 2006.

[38] Z. Zeng, J. J. Estrada-López, M. A. Abouzied, and E. Sánchez-Sinencio, "A reconfigurable rectifier with optimal loading point determination for RF energy harvesting from -22 dBm to -2 dBm," *IEEE Transactions on Circuits and Systems II: Express Briefs*, vol. 67, no. 1, pp. 87–91, 2020.

[39] Q. Wan, Y. Teh, Y. Gao, and P. K. T. Mok, "Analysis and design of a thermoelectric energy harvesting system with reconfigurable array of thermoelectric generators for IoT applications," *IEEE Transactions on Circuits and Systems I: Regular Papers*, vol. 64, no. 9, pp. 2346–2358, 2017.

[40] I. Lee *et al.*, "A $> 78\%$-efficient light harvester over 100-to-100klux with reconfigurable PV-cell network and MPPT circuit," *2016 IEEE International Solid-State Circuits Conference (ISSCC), San Francisco, CA*, 2016.

[41] S. Yoon, S. Carreon-Bautista, and E. Sánchez-Sinencio, "An area efficient thermal energy harvester with reconfigurable capacitor charge pump for IoT applications," *IEEE Transactions on Circuits and Systems II: Express Briefs*, vol. 65, no. 12, pp. 1974–1978, 2018.

[42] K. Rawy, T. Yoo, and T. T. Kim, "An 88% efficiency 0.1-300-μw energy harvesting system with 3-d mppt using switch width modulation for iot smart nodes," *IEEE Journal of Solid-State Circuits*, vol. 53, no. 10, pp. 2751–2762, 2018.

[43] L. Xia, J. Cheng, N. E. Glover, and P. Chiang, "0.56 V, -20 dBm RF-powered, multi-node wireless body area network system-on-a-chip with harvesting-efficiency tracking loop," *IEEE Journal of Solid-State Circuits*, vol. 49, no. 6, pp. 1345–1355, 2014.

[44] S. S. Amin and P. P. Mercier, "MISIMO: A multi-input single-inductor multi-output energy harvesting platform in 28-nm FDSOI for powering net-zero-energy systems," *IEEE Journal of Solid-State Circuits*, vol. 53, no. 12, pp. 3407–3419, 2018.

[45] K. Kadirvel *et al.*, "A 330nA energy-harvesting charger with battery management for solar and thermoelectric energy harvesting," *2012 IEEE International Solid-State Circuits Conference, San Francisco, CA*, 2012.

[46] Y. Lin *et al.*, "A sub-pW timer using gate leakage for ultra low-power sub-Hz monitoring systems," *2007 IEEE Custom Integrated Circuits Conference, San Jose, CA*, 2007.

[47] M. Seok *et al.*, "A 0.5V 2.2pW 2-transistor voltage reference," *2009 IEEE Custom Integrated Circuits Conference, Rome*, 2009.

[48] G. Papotto, F. Carrara, and G. Palmisano, "A 90-nm CMOS threshold-compensated RF energy harvester," *IEEE Journal of Solid-State Circuits*, vol. 46, no. 9, pp. 1985–1997, 2011.

[49] P. Xu *et al.*, "Analysis, modeling, and design of a 2.45-GHz RF energy harvester for SWIPT IoT smart sensors," *IEEE Journal of Solid-State Circuits*, vol. 54, pp. 2717–2729, Oct 2019.

[50] Z. Zeng *et al.*, "Design of sub-gigahertz reconfigurable RF energy harvester from -22 to 4 dBm with 99.8% peak MPPT power efficiency," *IEEE Journal of Solid-State Circuits*, vol. 54, pp. 2601–2613, Sep. 2019.

[51] N. Ayir *et al.*, "Experimenting waveforms and efficiency in RF power transfer," *2019 IEEE MTT-S International Microwave Symposium (IMS)*, pp. 1140–1143, June 2019.

[52] B. Clerckx *et al.*, "Fundamentals of wireless information and power transfer: From RF energy harvester models to signal and system designs," *IEEE Journal on Selected Areas in Communications*, vol. 37, pp. 4–33, Jan 2019.

[53] S. Fan *et al.*, "A 2.45-GHz rectifier-booster regulator with impedance matching converters for wireless energy harvesting," *IEEE Transactions on Microwave Theory and Techniques*, vol. 67, pp. 3833–3843, Sep. 2019.

[54] S. Lin *et al.*, "A high-efficiency power management IC with power-aware multi-path rectifier for wide-range RF energy harvesting," *2017 IEEE MTT-S International Microwave Symposium (IMS)*, pp. 304–306, June 2017.

[55] M. Seok *et al.*, "A portable 2-transistor picowatt temperature-compensated voltage reference operating at 0.5 V," *IEEE Journal of Solid-State Circuits*, vol. 47, pp. 2534–2545, Oct 2012.

[56] Y. Rao and D. P. Arnold, "An input-powered vibrational energy harvesting interface circuit with zero standby power," *IEEE Transactions on Power Electronics*, vol. 26, no. 12, pp. 3524–3533, 2011.

[57] C. Peters, J. Handwerker, D. Maurath, and Y. Manoli, "A sub-500 mV highly efficient active rectifier for energy harvesting applications," *IEEE Transactions on Circuits and Systems I: Regular Papers*, vol. 58, no. 7, pp. 1542–1550, 2011.

[58] Y. Lam, W. Ki, and C. Tsui, "Integrated low-loss cmos active rectifier for wirelessly powered devices," *IEEE Transactions on Circuits and Systems II: Express Briefs*, vol. 53, no. 12, pp. 1378–1382, 2006.

[59] C. v. Liempd, S. Stanzione, Y. Allasasmeh, and C. v. Hoof, "A 1μW-to-1mW energy-aware interface IC for piezoelectric harvesting with 40na quiescent current and zero-bias active rectifiers," in *2013 IEEE International Solid-State Circuits Conference Digest of Technical Papers*, pp. 76–77, 2013.

[60] A. Costilla Reyes, A. Abuellil, J. J. Estrada-López, S. Carreon-Bautista, and E. Sánchez-Sinencio, "Reconfigurable system for electromagnetic energy harvesting with inherent activity sensing capabilities for wearable technology," *IEEE Transactions on Circuits and Systems II: Express Briefs*, vol. 66, no. 8, pp. 1302–1306, 2019.

[61] A. Djemouai, M. A. Sawan, and M. Slamani, "New frequency-locked loop based on CMOS frequency-to-voltage converter: design and implementation," *IEEE Transactions on Circuits and Systems II: Analog and Digital Signal Processing*, vol. 48, no. 5, pp. 441–449, 2001.

[62] B.-D. Yang and S. W. Heo, "Accurate tunable-gain 1/x circuit using capacitor charging scheme," *ETRI Journal*, vol. 37, no. 5, pp. 972–978, 2015.

[63] Y. Gao, L. Li, and P. K. T. Mok, "An AC input inductor-less led driver for efficient lighting and visible light communication," *IEEE Journal of Solid-State Circuits*, vol. 53, no. 8, pp. 2343–2355, 2018.

[64] M.-H. Cheng and Z.-W. Wu, "Low-power low-voltage reference using peaking current mirror circuit," *Electronics Letters*, vol. 41, no. 10, pp. 572–573, 2005.

[65] A. Shrivastava, Y. K. Ramadass, S. Khanna, S. Bartling, and B. H. Calhoun, "A 1.2μW simo energy harvesting and power management unit with constant peak inductor current control achieving 8392% efficiency across wide input and output voltages," in *2014 Symposium on VLSI Circuits Digest of Technical Papers*, pp. 1–2, 2014.

[66] S. Carreon-Bautista, A. Eladawy, A. Nader Mohieldin, and E. Sánchez-Sinencio, "Boost converter with dynamic input impedance matching for energy harvesting with multi-array thermoelectric generators," *IEEE Transactions on Industrial Electronics*, vol. 61, no. 10, pp. 5345–5353, 2014.

[67] S. Shin, Y. Huh, Y. Ju, S. Choi, C. Shin, Y. Woo, M. Choi, S. Park, Y. Sohn, M. Ko, Y. Jo, H. Han, H. Lee, S. Hong, W. Qu, and G. Cho, "A 95.2% efficiency dual-path DC-DC step-up converter with continuous output current delivery and low voltage ripple," in *2018 IEEE International Solid - State Circuits Conference - (ISSCC)*, pp. 430–432, 2018.

[68] C. Liu, H. Lee, P. Liao, Y. Chen, M. Chung, and P. Chen, "Dual-source energy-harvesting interface with cycle-by-cycle source tracking and adaptive peak-inductor-current control," *IEEE Journal of Solid-State Circuits*, vol. 53, no. 10, pp. 2741–2750, 2018.

[69] S. Kiran, S. Cai, Y. Luo, S. Hoyos, and S. Palermo, "A 52-Gb/s ADC-based PAM-4 receiver with comparator-assisted 2-bit/stage SAR ADC and partially unrolled DFE in 65-nm CMOS," *IEEE Journal of Solid-State Circuits*, vol. 54, no. 3, pp. 659–671, 2019.

[70] Y. Li, Q. Guo, M. Huang, X. Ma, Z. Chen, H. Liu, and L. Sun, "Study of an electromagnetic ocean wave energy harvester driven by an efficient swing body toward the self-powered ocean buoy application," *IEEE Access*, vol. 7, pp. 129758–129769, 2019.

APPENDIX A

POWER-COMBING EH SYSTEM WITH GLOBAL MPPT FOR HOMOGENEOUS WTG ARRAY

In this appendix chapter, a power-combining EH system is designed to handle the uncertainty of the coming wind power and to increase the overall harvested power capacity. Because of the dynamic changing wind power profiles, the generated power in each turbine can be similar or different depending on the wind flow direction, the angle of attack, the position of the turbine, and some other factors. Therefore, a power-combing system is desired to automatically select the maximum power source if there is one outstanding power source from others, meanwhile, to have the power combing ability when power sources are close to each other.

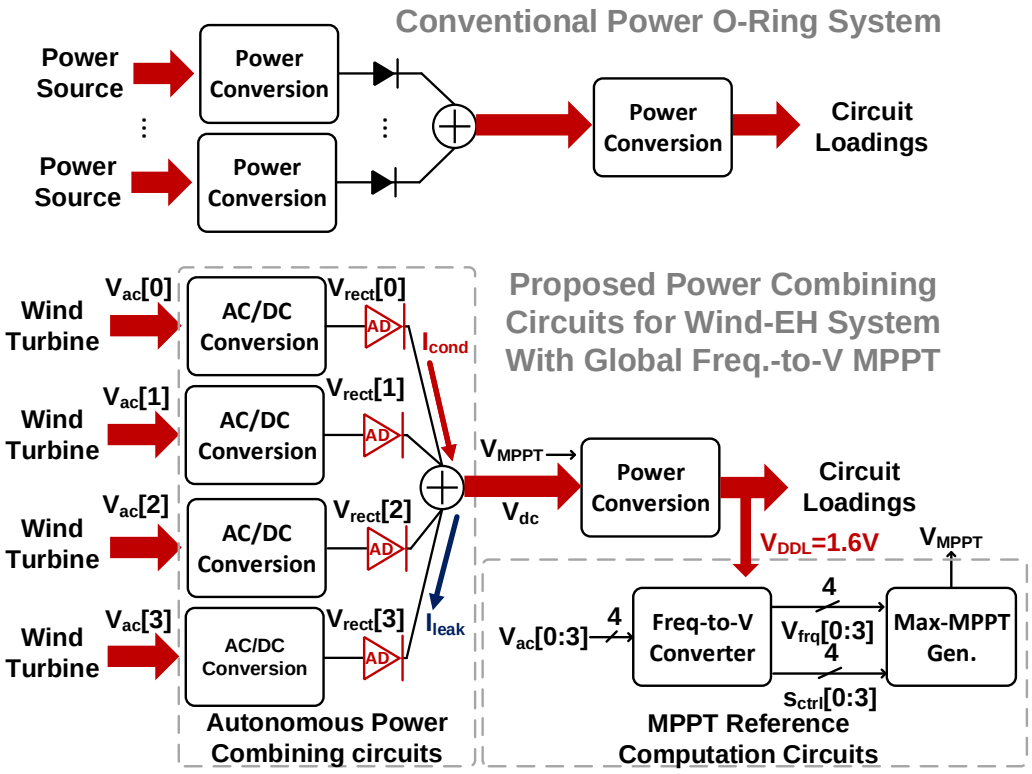

Figure A.1: 4-Channel wind-EH power-combing system.

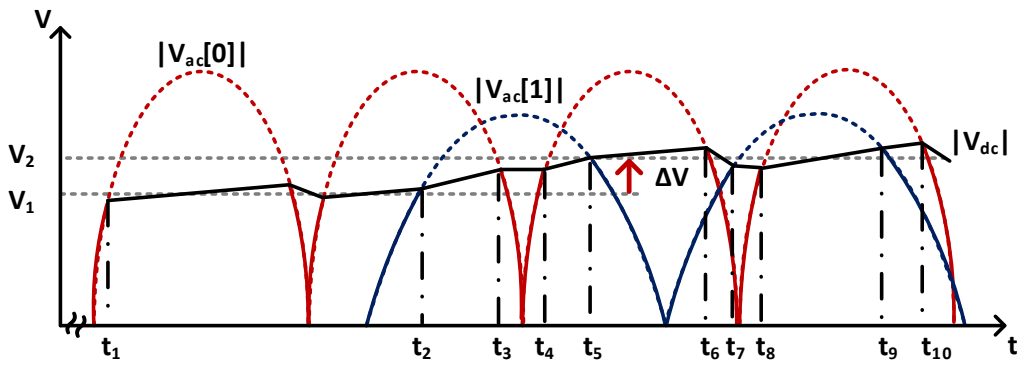

Figure A.2: Power combination in a dual-input power O-Ring system.

Fig. A.1 shows the basic concept of a power-combining system with a power O-Ring architecture. It is typically used in a battery charging system to switch between multiple potential sources. However, the forward voltage drop in the diode will degrade the overall efficiency in low voltage EH applications. Therefore, an active diode (AD) based power O-Ring architecture is proposed in this work. The proposed topology automatically delivers the energy from the turbine with the most generated power among the other idle turbines. The AD cuts off the reverse leakage automatically by sensing the rectifier output and the shared combiner output node $V_{\rm dc}$. Moreover, the AD also conducts the current whenever the generated voltage in each wind turbine is high enough. Therefore, our proposed topology also serves as an autonomous power-combining circuit for multiple-source energy harvesting applications compared to the other existing solutions.

In this work, the self-biased active diode is adopted to guarantee the forwarded power delivery and suppress the reverse leakage through the inactive EH source. Homogeneous WTGs are employed to build the array energy harvester, which guarantees similar electrical parameters in each turbine and the system can be regarded as a current combination in parallel. To accommodate the 4-channel wind turbine array, a global MPPT method is proposed to locate the optimal loading point of the maximum EH source. In this case, the cascading PMU only requires one input node to harvest all the combined energy based on the generated MPPT reference voltage.

The wind turbines are homogeneous in the EH array, so they share the identical electrical

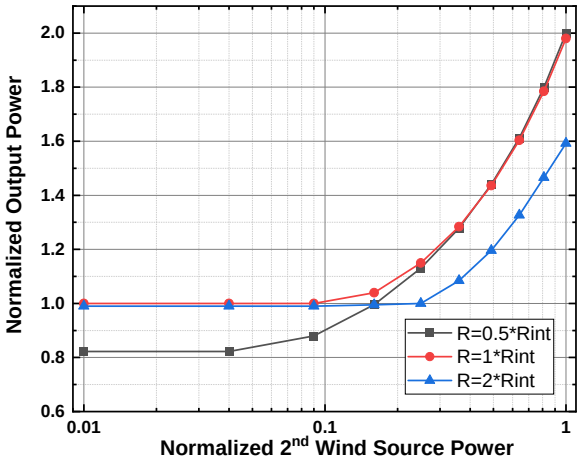

Figure A.3: Power combination simulation for two inputs.

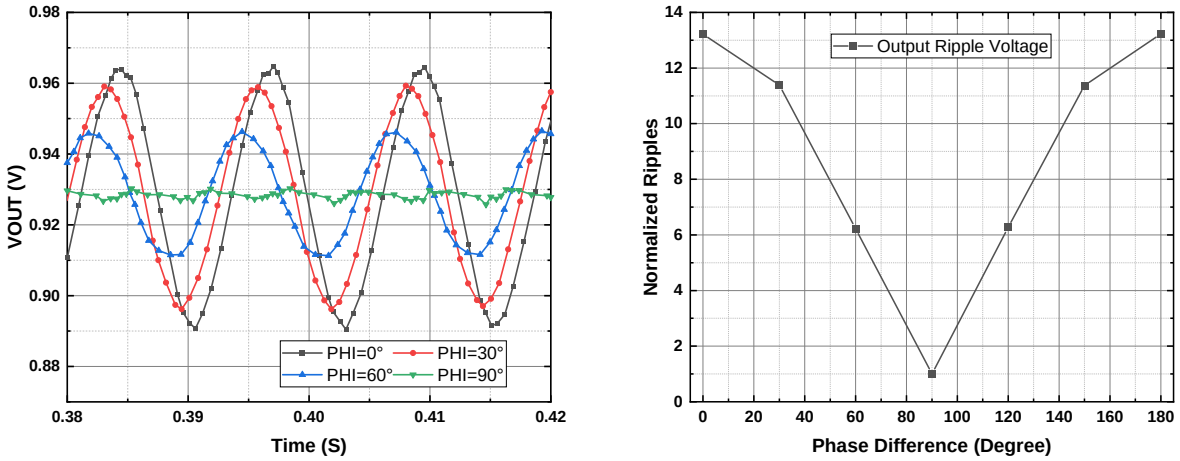

(a) (b)

Figure A.4: (a) Output voltage in dual-input system and (b) output ripples with different input phase.

models with the similar wind power conversion ability and same internal impedance. Fig. A.2 shows an example to illustrate the power combination abilities on a fixed loading resistance. From the time t1 to t2, the voltage Vdc is sustained by the single power source $V_{ac[0]}$. And in time t2 to t5, the secondary power source $V_{ac[1]}$ is available to power up the V_{dc} therefore the voltage will increase because of the additional conduction current.

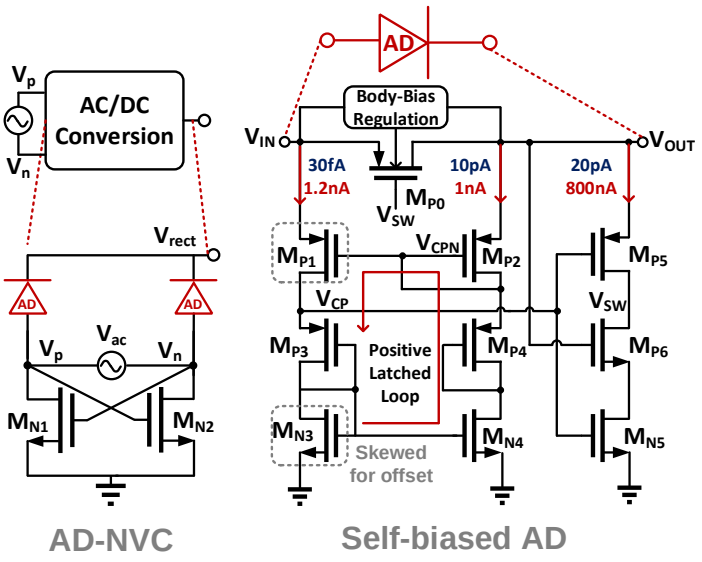

Name	Width (um)	Length (um)
M_{N1}	1800	0.18
M_{N2}	1800	0.18
M_{P0}	1800	0.18
M_{P1}	10	0.5
M_{P2}	12	0.5
M_{P3}	10	0.5
M_{P4}	10	0.5
M_{N3}	4	0.5
M_{N4}	2	0.5
M_{P5}	2	10
M_{P6}	2	10
M_{N5}	2	10

Figure A.5: AC-DC rectifier and self-biased active diode.

Fig. A.3 shows detailed simulation results of the power combination effect under different power conditions in dual-input systems. The output power increases with the secondary source power level and it reaches $2\times$ compared to single-source conditions when the two power sources are in similar conditions. And the optimal loading resistance will change to $0.5\times R_{\text{int}}$ from R_{int} because the parallel current combination is connecting the power source into parallel configuration. And in practical implementations, the variable loading is achieved by a cascading DC-DC converter with maximum power extraction functions. A two-source power combination is analyzed in this section, and it can be expanded to multi-source array scenarios.

Fig. A.4 shows the phase effect when the power of two WTG sources is identical. Although the ripple value depends on the phase difference from these two EH sources. The average output voltage and the output power is similar. An appropriate filtering capacitor is required for the worst case. And in practical implementations, the phase in each WTG is dithered by the variant wind speeds and directions. Therefore, the misaligned phase reduces the effective ripple voltage at the V_{dc} based on the simulation results. And if the phase difference is well controlled, the ripple can be further reduced as shown in Fig. A.4.

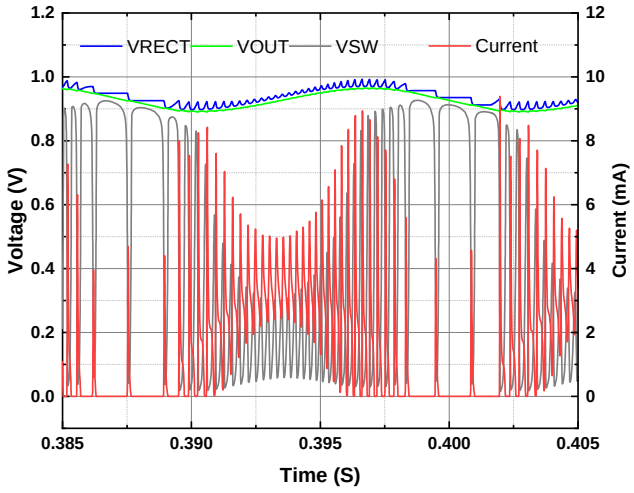

(a)

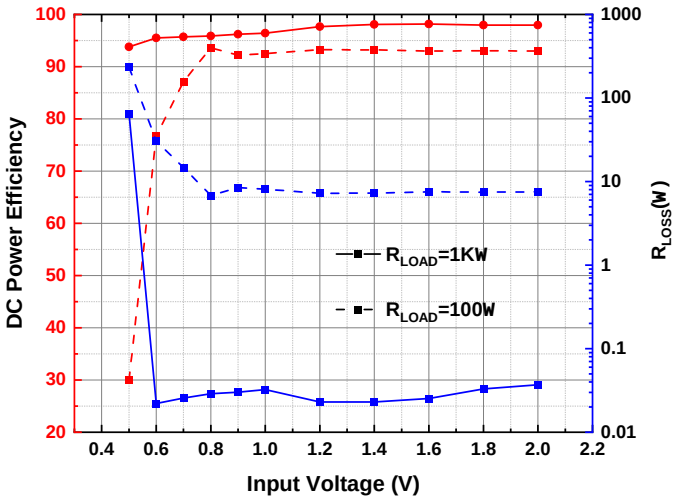

(b)

Figure A.6: Active diode (a) simulation waveform and (b) efficiency in measurement.

The self-biased AD in AD-NVC rectifier is employed in the AD-based Power O-Ring combiner. The schematic is shown in Fig. A.5. Because of its merit in autonomous and self-biased operations. The power combiner automatically conducts the available EH source and maximize the final output power. In Fig. A.6, the operation details in the self-biased AD for power combinations are plotted. The system is self-oscillating because of the hysteresis mechanism. The oscillating frequency is around 4 KHz, and adaptive to the voltage amplitude of the EH source. In measure-

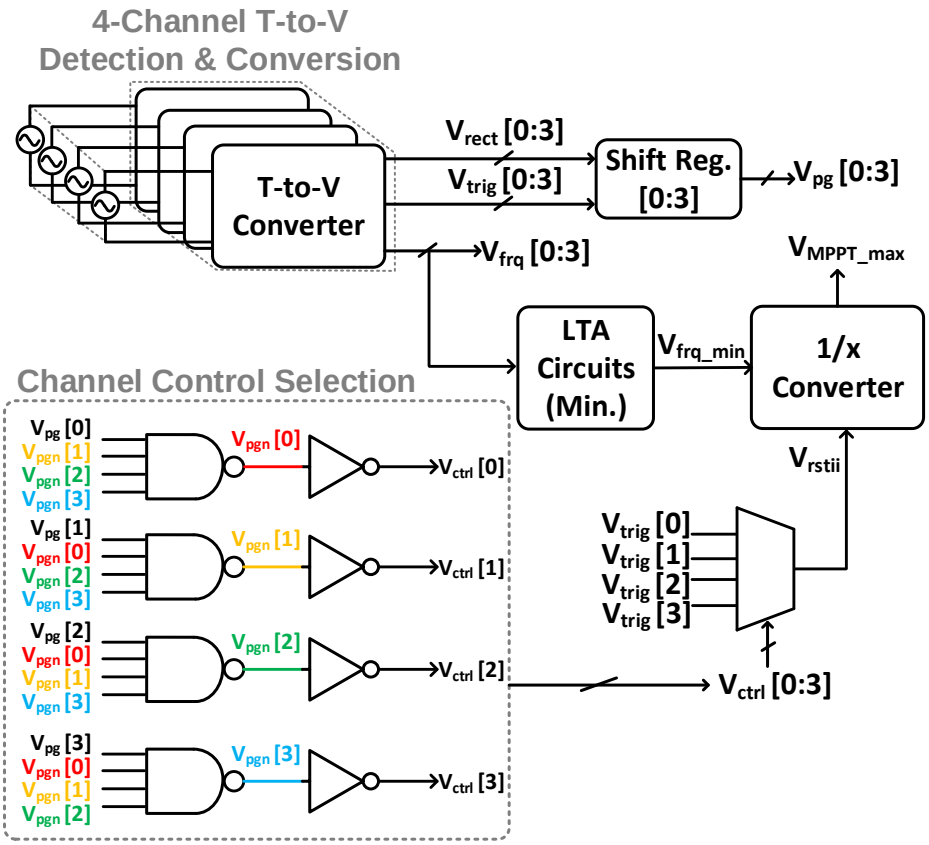

Figure A.7: Global MPPT voltage generation from 4-channel combiner.

ment, the PCE of the AD is around 93% ($R_{\text{int}} = 100\Omega$) to 98% ($R_{\text{int}} = 1000\Omega$), and the PCE is larger than 90% with a DC input of 0.7 V. The DC efficiency measurement is shown in Fig. A.6b, achieving a peak efficiency of 98.1% for 1-mW output power.

The global MPPT for WTG array is based on the FAC MPPT introduced in Chapter 5. To locate the WTG with the maximum power among others, the maximum V_{MPPT} is detected and ranked. A simple analog-to-digital converter (ADC) can be used but it introduces too much power and resources overhead. In this work, an analog computation method is used based on winner-takes-all (WTA) and loser-takes-all (LTA) techniques. As shown in Fig. A.7, LTA circuits are used to detect the minimum intermediate voltage V_{frq} which represents the WTG with the highest rotation frequency and also the largest power. To trigger the system operations, the trigger signals generated from each WTG are fed into a digital multiplexer circuit. Therefore, the control signal

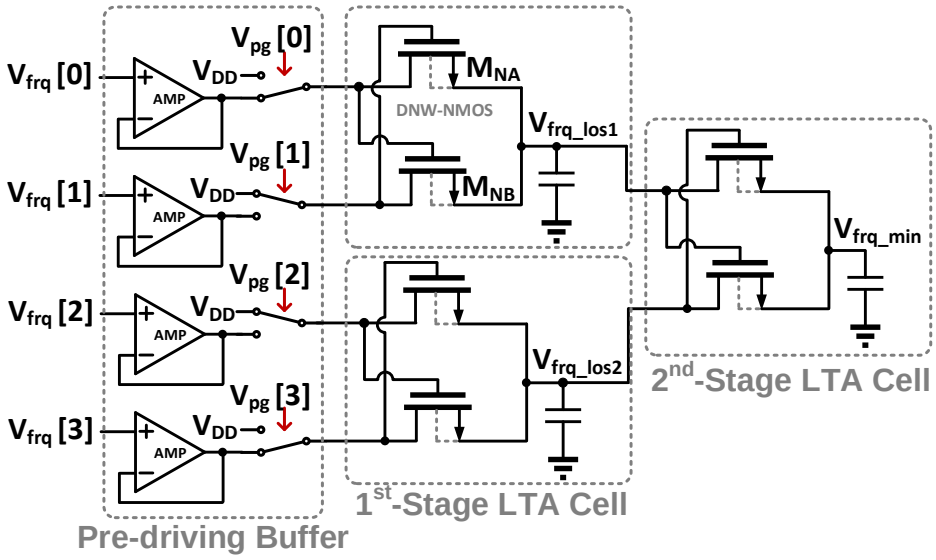

Figure A.8: LTA processing circuits with driving buffers.

is from one of the activated WTG, and no additional clock is required to save power. The whole system is autonomous to harvest, detect, and combine the power from the WTG array. Need to be mentioned, the global V_{MPPT} is converted directly by the minimum value of V_{frq} so only one reciprocal (1/x) block is required, which significantly reduces the circuit layout areas by 30% compared to the architecture that generates all the V_{MPPT} signals. This architecture is also suitable for a high-order array with more numbers of WTGs. And each MPPT engine parameter can be adjusted based on different WTG characteristics in potential heterogeneous EH applications.

Fig. A.8 shows the details of the LTA circuits. Between the LTA circuits and the input V_{freq}, a nA-biased unit-gain buffer is inserted to provide the driving ability and isolate the input and output. And when the WTG is not activated, the corresponding V_{freq} is not defined. Therefore, a digital multiplexer is added to ensure the correct final results. The V_{freq} is set to logic high by the internal power-good signal in each WTG channel. Fig. A.9, similar to the V_{MPPT} results presented in Chapter 5, the global V_{MPPT} in the 4-channel combiner circuits also achieves wide tuning abilities and high accuracy for FAC MPPT.

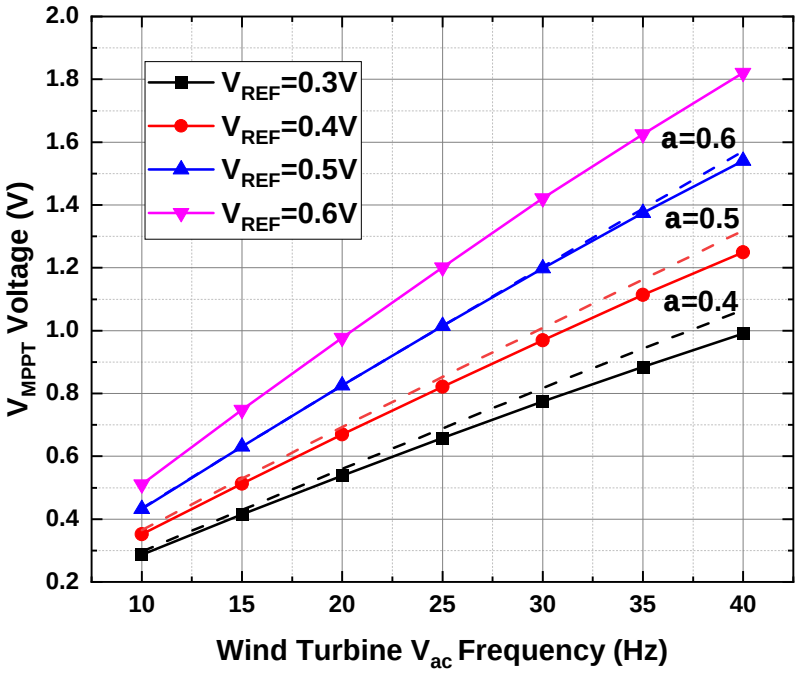

Figure A.9: Global V_{MPPT} measurement results.

APPENDIX B

A MATCHING NETWORK DESIGN EXAMPLE FOR 2.4-GHZ RECTIFIER WITH SIMULATIONS

This appendix chapter is based on the 2.4GHz RF-DC rectifier matching network designs. The entire matching network design procedure is assisted by an end-to-end simulation model, which matches with the measurement results and provide design guidance without iterations in the replacement of the components.

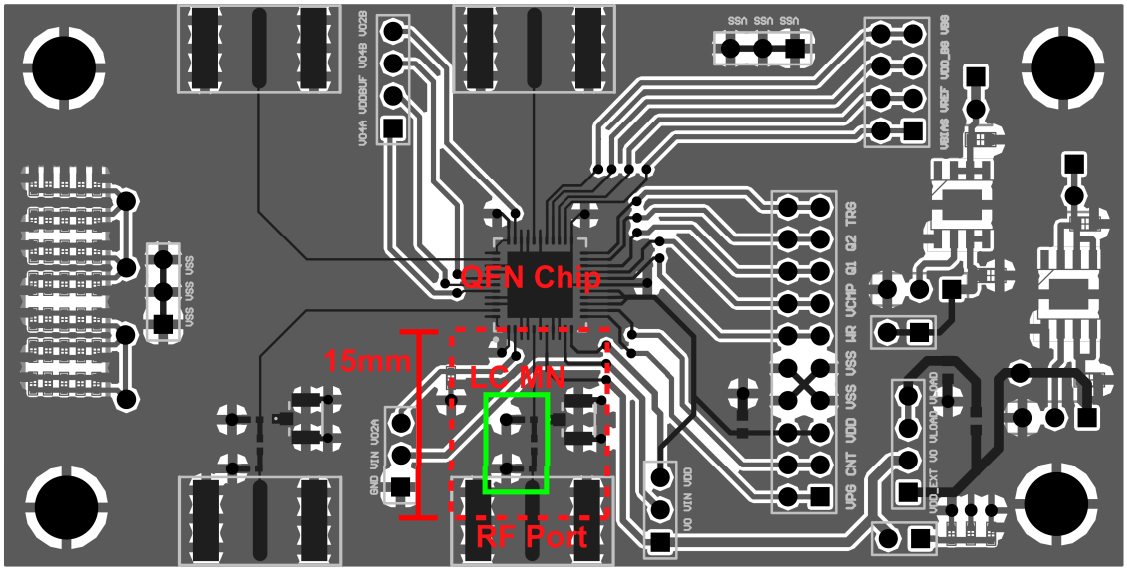

Figure B.1: PCB layout for 2.4-GHz RF-DC rectifier.

Fig. B.1 shows the PCB layout and component slots reserved for the matching network. Conventional matching network is based on conjugate matching for $50\ \Omega$. However, typical RF-DC rectifier chips are not designed for $50\ \Omega$ matching. Therefore, the s-parameters need to be measured before the matching network designs, which can be done by inserting a zero-ohm resistor. Meanwhile, the LC components in matching network LC usually need to be replaced after first-round

measurements. An accurate end-to-end model is helpful to maximize the system performance and reduce the design time significantly.

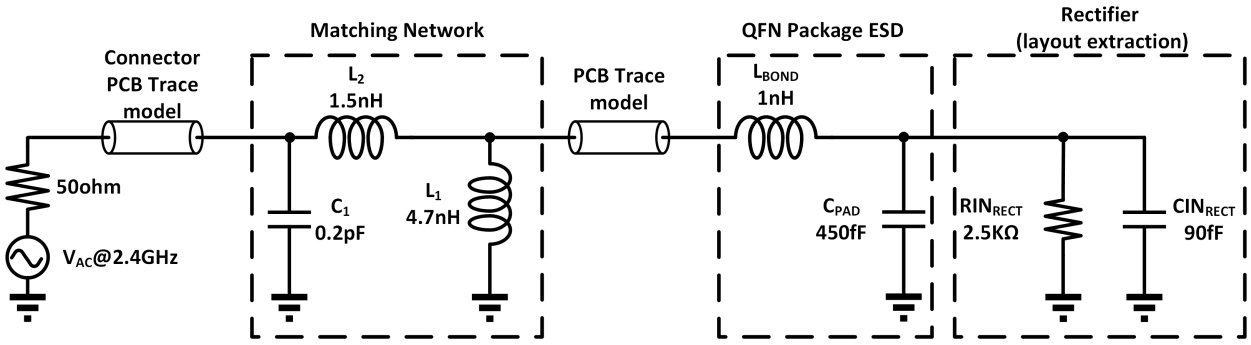

Figure B.2: End-to-end RF model for matching network design.

Fig. B.2 is the final matching network design with the parasitic models. The rectifier input impedance is extracted from post-layout simulations. The package parameter includes the bonding wire inductor and the bonding pad capacitor. A Pi-type matching network topology is selected for its flexibility. The PCB trace model is extracted from the PCB layout by the planar EM simulator.

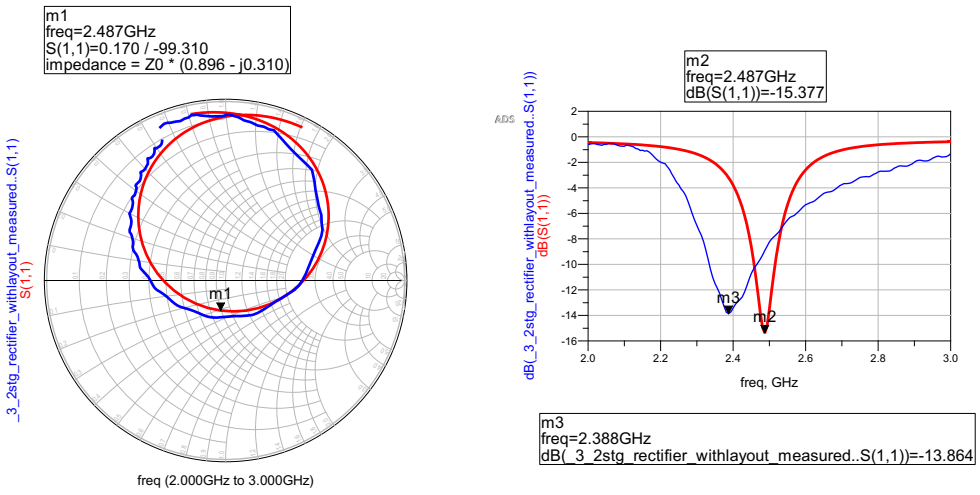

Figure B.3: S-parameter simulation compared with measurement. (with ideal LC)

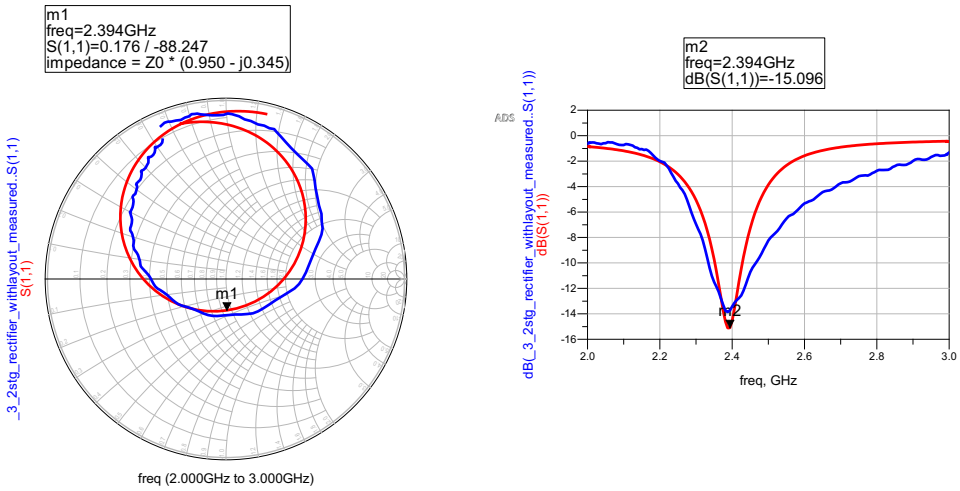

Figure B.4: S-parameter simulation compared with measurement. (with actual LC models)

The simulation results are plotted in Fig. B.3 and Fig. B.4 to compare with the measurements. The ideal LC components are used at first and then the s2p files from the manufacture foundries are imported as the actual parameter. It can be found that the proposed end-to-end model is very accurate compared to the measurement results. The analytical model not only provides insightful design guidance but also reduces the overall design iteration and complexity significantly.